ISTANBUL TECHNICAL UNIVERSITY ★ GRADUATE SCHOOL OF SCIENCE, ENGINEERING AND TECHNOLOGY

SOURCE MODELS OF SEPTEMBER 25, 2013 ACARI - PERU (M_W 7.1) AND SEPTEMBER 08, 2017 CHIAPAS - MEXICO (M_W 8.2) EARTHQUAKES AND TSUNAMI SIMULATIONS

M.Sc. THESIS

H.Tarık MERİÇ

Department of Geophysics Engineering

Geophysics Engineering M.Sc. Programme

APRIL 2019

ISTANBUL TECHNICAL UNIVERSITY ★ GRADUATE SCHOOL OF SCIENCE, ENGINEERİNG AND TECHNOLOGY

SOURCE MODELS OF SEPTEMBER 25, 2013 ACARI - PERU (M_W 7.1) AND SEPTEMBER 08, 2017 CHIAPAS - MEXICO (M_W 8.2) EARTHQUAKES AND TSUNAMI SIMULATIONS

M.Sc. THESIS

H.Tarık MERİÇ
505161411

Department of Geophysics Engineering

Geophysics Engineering M.Sc. Programme

Thesis Advisor: Assoc. Prof. Seda YOLSAL-ÇEVİKBİLEN

APRIL 2019

İSTANBUL TEKNİK ÜNİVERSİTESİ ★ FEN BİLİMLERİ ENSTİTÜSÜ

25 EYLÜL 2013 ACARI PERU (M_W 7.1) VE 08 EYLÜL 2017 CHIAPAS MEKSİKA (M_W 8.2) DEPREMLERİNİN KAYNAK MEKANİZMASI ÇÖZÜMÜ VE TSUNAMİ SİMÜLASYONLARI

YÜKSEK LİSANS TEZİ

H. Tarık MERİÇ
505161411

Jeofizik Mühendisliği Anabilim Dalı

Jeofizik Mühendisliği Yüksek Lisans Programı

Tez Danışmanı: Doç. Dr. Seda YOLSAL-ÇEVİKBİLEN

NİSAN 2019

Hakan Tarık MERİÇ, a M.Sc. student of ITU Graduate School of Science Engineering and Technology student ID 505161411, successfully defended the thesis entitled “SOURCE MODELS OF SEPTEMBER 25, 2013 ACARI - PERU (M_W 7.1) AND SEPTEMBER 08, 2017 CHIAPAS - MEXICO (M_W 8.2) EARTHQUAKES AND TSUNAMI SIMULATIONS”, which he prepared after fulfilling the requirements specified in the associated legislations, before the jury whose signatures are below.

Thesis Advisor : **Assoc. Prof. Dr. Seda YOLSAL-ÇEVİKBİLEN**
Istanbul Technical University

Jury Members : **Prof. Dr. Tuncay TAYMAZ**
Istanbul Technical University

Jury Members : **Assoc. Prof. Dr. Tahir Serkan IRMAK**
Kocaeli University

Jury Members : **Assoc. Prof. Dr. Seda YOLSAL-ÇEVİKBİLEN**
Istanbul Technical University

Date of Submission : 14 March 2019
Date of Defense : 05 April 2019

To my mother,

FOREWORD

First, I would like to thank my thesis advisor Assoc. Prof. Seda Yolsal- Çevikbilen for her guidance and support at each step of this study. She always persuaded me to learn and extend my knowledge in this field.

I would also like to thank Prof. Dr. Tuncay Taymaz for letting me draw on from his unique experience in this field and giving me the opportunity to study in an academic enviroment, in the seismology laboratory with fellow M.Sc and Ph.D. students.

I would like to thank Dr. Tuna Eken who helps me to solve problems I encountered and for all his suggestions improving my thesis.

I would like to thank Assoc. Prof. Tahir Serkan Irmak from Kocaeli University who is one of the jury member, for his valuable comments on this thesis.

The teleseismic body waves used in this thesis are from the International Federation of Digital Seismograph Networks (FDSN), the Global Digital Seismograph Network (GDSN) stations and archived at the IRIS-DMC, http://ds.iris.edu/wilber3/find_event. Dart and tide gauge data are taken from National Oceanic and Atmospheric Administration's National Data Buoy Center (NDBC-DART), https://www.ndbc.noaa.gov/dart.shtml and Sea Level Monitoring Facility of Intergovernmental Oceanographic Commision (IOC) http://www.ioc-sealevelmonitoring.org/index.php respectively. Software packages of Generic Mapping Tools (GMT8) (Wessel and Smith, 1998) were used to prepare some of the figures and SAC2000 (Goldstein et al., 2003) to process conventional earthquake data. Bathymetry data for tsunami simulations are taken from General Bathymetric Chart of the Oceans (GEBCO) https://www.gebco.net/. MT5 algorithm developed by McCaffrey et al. (1991) is further used to estimate source parameters of the earthquakes. I would like to thank Yuji Yagi for sharing his rupture history and slip distribution code as well as Xiaoming Wang for sending the latest version of COMCOT to me to perform numerical tsunami simulations. This M.Sc. thesis was further supported by Turkish Academy of Sciences (TÜBA) in the framework for Young Scientist Award Program (TÜBA-GEBİP) awarded to Assoc. Prof. Seda Yolsal Çevikbilen in 2018.

Finally, I would like to thank my beloved mother, Servet Tendu Meriç, for her love and support and my dear friends Elif Batıgün, Ceyhun Erman and Beran Gürleme for always being there for me. Thank you.

May 2019 Hakan Tarık MERİÇ

TABLE OF CONTENTS

Page

ABBREVIATIONS

BB	: Broad Band
BODC	: British Oceanographic Data Centre
CFL	: Courant–Friedrichs–Lewy condition
COMCOT	: Cornell Multi-grid Coupled Tsunami Model
DART	: Deep-Ocean Assessment and Reporting of Tsunami
ETOPO1	: 1 arc-minute global relief model of Earth's surface
GEBCO	: General Bathymetric Chart of the Oceans
GEBCO-30	: General Bathymetric Chart of the Oceans (30 arc-seconds)
Harvard-CMT	: The Harvard University - Centroid Moment Tensor
IOC	: Intergovernmental Oceanographic Commission
LP	: Long Period
NDBC	: National Data Buoy Center
NOAA	: National Oceanic and Atmospheric Administration
PSMSL	: Permanent Service for Mean Sea Level
SAC	: Seismic Analysis Code
SEED	: The Standard for the Exchange of Earthquake Data
SLSMF	: Sea Level Station Monitoring Facility
USGS	: United States Geological Survey

SYMBOLS

M	: Magnitude
MA, Dav	: Average Displacement
MD, D_{max}	: Maximum Displacement
M_o	: Seismic Moment
M_w	: Moment Magnitude
M_{wc}	: Centroid moment tensor
M_{ww}	: Moment W-phase
pP, pS , sS	: Reflection phases
RA	: Rupture Area
RW	: Rupture Width
SRL	: Sub-surface rupture length
δ	: Dip angle
λ	: Rake angle
φ	: Strike angle

LIST OF TABLES

Page

LIST OF FIGURES

Page

SOURCE MODELS OF SEPTEMBER 25, 2013 ACARI - PERU (M_w 7.1) AND SEPTEMBER 08, 2017 CHIAPAS - MEXICO (M_w 8.2) EARTHQUAKES AND TSUNAMI SIMULATIONS

SUMMARY

Subduction zones are places where intense earthquake activity is observed and often result in tsunami waves as a result of destructive earthquakes ($M_w > 7.0$). By using seismological observations such as kinematic and dynamic source mechanism parameters of large earthquakes occurred along these convergent boundaries and high resolution bathymetry data, mathematical tsunami simulations can be made. Thus, propagation of earthquake induced tsunamis waves, their effects on the coastal plains and wave characteristics can be determined. In this MSc. Thesis, source mechanism solutions with minimum misfit obtained from the inversion of teleseismic long-period (LP) P- and SH- waveforms are determined for the September 25, 2013 Acari-Peru (M_w 7.1) and September 08, 2017 Chiapas-Mexico (M_w 8.2) earthquakes. Then, finite-fault slip models of both earthquakes are achieved using teleseismic broad-band (BB) P-waveforms.

The southeast Pacific region is one of the most seismically active convergence regions in the world. Here, two different parts of this region have been studied for earthquake and tsunami hazard mitigation. Since this region hosts a large number of destructive earthquakes, it is important to understand tectonic behavior of this active zone. In the north, there is Middle America trench where Cocos plate subducting beneath Caribbean and North American plates, and in the south, subduction of Nazca plate under South American plate defines the tectonic processes.

The convergence between Nazca and South American plate, is the reason for the uplift of Andes Mountains and active volcanic belt present there. This is also the main reason for the occurrence of destructive earthquakes and earthquake induced tsunamis at western edge of the South American plate. One of the two earthquakes investigated in this study is 25 September 2013 Acari, Peru earthquake (M_w: 7.1) with an earthquake epicenter being Peru-Chile subduction zone. Source model and finite-fault slip distribution model is investigated using P- and SH- waveforms recorded at teleseismic distances. Source mechanism solution indicates that the 2013 Acari (Peru) earthquake (M_w 7.1) occurred at shallow focal depth (h: 48 km) with a thrust faulting mechanism.

The September 08, 2017 Chiapas, Mexico earthquake (M_w 8.2) occurred at west side of the Panama fracture zone where Cocos, North American and Caribbean plates meet at a triple junction called Middle America Trench. Cocos plate subducts under North American and Caribbean plates with a rate of 6.4 cm/yr. The source mechanism solution of this earthquake indicates a normal faulting mechanism. By using source mechanism solutions of these earthquakes, numerical tsunami simulations based on a uniform slip occurred on the fault plane have also been

achieved. Synthetics and observed tsunami waveforms are compared and it is seen that most of the amplitudes of tsunami waveforms are well matched.

25 EYLÜL 2013 ACARİ PERU (Mw 7.1) VE 08 EYLÜL 2017 CHİAPAS MEKSİKA (MW 8.2) DEPREMLERİNİN KAYNAK MEKANİZMASI ÇÖZÜMÜ VE TSUNAMİ SİMÜLASYONLARI

ÖZET

Deprem, dünya genelindeki levhaların hareketleri sonucunda biriken elastik gerilmenin ani bir şekilde boşalması sonucu açığa çıkan enerji ile meydana gelen elastik dalgaların yayılarak geçtikleri ortamları sarsmasından kaynaklanan ve yeryüzündeki yapılara zarar veren doğal bir olaydır. Yitim (dalma-batma) zonları, birbirine yakınlaşan iki levhadan birinin diğeri altına dalıp-batması sonucu yüksek deprem aktivitesinin meydana geldiği ve yıkıcı depremlere (M_w > 7.0) eşlik eden tsunami dalgalarının gözlendiği bölgelerdir. Bu bölgelerde oluşan büyük depremlerin sismolojik çalışmalar ile deprem kaynak modelleri ve kinematik ve dinamik kaynak parametreleri belirlenerek, bu parametreler ve yüksek çözünürlüklü batimetri verilerinin kullanılmasıyla matematiksel tsunami simülasyonları yapılabilmektedir.

Deprem odak mekanizması parametrelerinin giriş verisi olarak kullanıldığı tsunami simulasyonları, fay düzlemi üzerinde meydana gelen kırılmanın deniz tabanı üzerinde oluşturduğu düşey yerdeğiştirmenin hesaplanması ve bu yüzey deformasyonunun açığa çıkan tsunami başlangıç dalgası ile yaklaşık olarak aynı olduğu varsayımına dayanmaktadır. Böylece deprem kaynaklı tsunami dalgalarının okyanus veya deniz içerisinde yayılımı, kıyılara etkileri ve dalga özellikleri belirlenebilir. Tsunamiler de depremler gibi büyük can ve mal kayıplarına neden olan doğal afetler oldukları için araştırılmaları oldukça önemlidir. Genellikle deprem kaynaklı tsunamilerin oluşması için depremin okyanus tabanında, sığ odak derinliğinde, düşey yerdeğiştirmeye neden olan normal veya ters faylanma ile meydana gelmiş olması gerekmektedir.

Bu çalışmada 25 Eylül 2013 Acari-Peru (M_w 7.1) ve 08 Eylül 2017 Chiapas-Meksika (M_w 8.2) depremleri için telesismik P- ve SH- dalga şekillerinin ters çözümünden elde edilen en düşük hatalı odak mekanizması çözümü belirlenmiştir. Odak mekanizması telesismik dalga şekillerinin ters çözümüne dayalı olarak depremin ikili kuvvet çifti ve moment tensör çözümlerini sağlayan bir bilgisayar programı olan MT5 algoritması ile bulunmuştur. Sonrasında, geniş bantlı P-dalga formları ile *'hybrid back-projection'* yöntemi kullanılarak depremlerin sonlu fay kayma dağılımı modeli elde edilmiştir. Bu yöntem uzay ve zamanda sismik enerji salınımını tahmin eden bir yöntemdir ve Pp, sP fazlarını kaynağın yakınındaki süreksizliklerden yansıyan fazlarla birleştirmek için P- dalgalarını kullanır. Tüm sonuçlar kullanılarak, deprem sonrasında gözlenen tsunami dalgalarının maksimum dalga yüksekliklerini ve varış zamanlarını elde etmek için matematiksel tsunami simulasyonları yapılmıştır.

Pasifik okyanusunu çevreleyen dalma-batma zonlarında yoğun deprem ve volkanik aktivite gözlenmektedir. Deprem ve volkanik aktivitenin yoğun olduğu bu kuşağa *'Pasifik Ateş Çemberi'* (Ring of Fire) adı verilmiştir. Güneydoğu Pasifik bölgesi

depremsellik açısından, bu çemberin en aktif bölgelerinden biridir. Depremlerin ve tsunamilerin kıyı kesimler üstünde oluşturduğu riski azaltılması için bu bölgenin iki farklı kısmı incelenmiştir. Bu bölge büyük miktarda yıkıcı depreme ev sahipliği yaptığı için, bu aktif bölgenin tektonik davranışını anlamak önemlidir. Kuzeyde, Karayip ve Kuzey Amerika plakalarının altına Cocos plakasının yittiği Orta Amerika hendeği bulunmaktadır. Güneyde ise Güney Amerika plakası altına doğru Nazca plakasının yitimi tektonik süreçleri tanımlamaktadır.

Nazca Levhası hem yakınlaşan hem uzaklaşan levha sınırlarına sahip olan, birden fazla üçlü kesişim bölgesi barındıran, üç adet denizdağları zinciri bulunan, batıda Pasifik Levhası ve güneyinde Antarktika levhası tarafından sırasıyla Doğu Pasifik Yükselimi ve Şili Yükselimi ile sınırlanmış okyanusal bir kabuktur. Nazca ve sabit Güney Amerika plakası arasındaki çarpışma, ve Nazca plakasının Güney Amerika levhasının altına dalıp-batması, And Dağları'nın yükselişinin ve orada bulunan aktif volkanik kuşağın sebebidir. Bu durum, Güney Amerika'nın batı tarafında yıkıcı depremlerin ve deprem kaynaklı tsunamilerin meydana gelmesinin ana nedenidir. Bu çalışmada incelenen iki depremden biri de 25 Eylül 2013 tarihinde Peru-Şili dalma-batma zonunda meydana gelmiş olan 2013 Acari, Peru depremidir. Deprem kaynak modeli, telesismik mesafelerdeki sismik istasyonlarda kaydedilen P- ve SH- dalga şekillerinin ters çözümü ile belirlenmiştir. Bu çözüm 2013 Acari (Peru) depreminin sığ odak derinliğinde ve bindirme fay mekanizmasıyla oluştuğunu göstermektedir. Telesismik uzaklıklardan alınan P- ve SH- dalga şekillerinin ters çözümü ile elde edilen nokta-kaynak ikili kuvvet-çifti kaynak modeli ve *'hybrid back-projection'* yöntemi ile bulunan tek-düze olmayan fay modeli, matematiksel tsunami simulasyonlarının giriş parametreleri olarak kullanılmış ve elde edilen sonuçlar DART kayıtçıları ve gel-git ölçerler tarafından kayıt edilen veriler ile karşılaştırılmıştır.

8 Eylül 2017 Chiapas, Meksika depremi, Cocos, Kuzey Amerika ve Karayip levhalarının Orta Amerika dalma-batma zonu üçlü-kesişimde buluştuğu Panama kırığı bölgesinin batı tarafında Tehuantepec sırtı yakınında meydana gelmiştir. Bu deprem sonucu 98 ölü ve 300'den fazla kişinin yaralandığı bildirilmiştir. Cocos levhası, Kuzey Amerika ve Karayip levhalarının altına 6.4 cm / yıl'lık bir oranla dalıp batmaya uğramaktadır. Bu bölgede son 100 yılda büyük bir deprem meydana gelmediği için sismik boşluk olduğu düşünülmektedir. Elde edilmiş sonuçlar bu depremin odak mekanizması çözümünün normal faylanma olduğunu göstermektedir. Her ne kadar bu depremin merkezi yitim zonu yakınında olsada, Orta Amerika hendeğinde genellikle meydana gelen *'megathrust'* depremlerinden ziyade bu deprem, Cocos levhasında yüksek açılı, kuzeydoğu eğimli normal faylanma ile meydana gelmiş olması ilginçtir. Bu nedenle, bu tsunami için erken uyarı zordur, çünkü tsunami tahmin yöntemleri genellikle yitim bölgelerinde bindirme fay mekanizması ile meydana gelen depremler için geliştirilmişlerdir.

8 Eylül 2017 Chiapas, Meksika depremi için telesismik uzaklıklardan alınan P- ve SH- dalga şekillerinin ters çözümü ile elde edilen nokta-kaynak ikili kuvvet-çifti kaynak modeli ve *'hybrid back-projection'* yöntemi ile bulunan tek-düze olmayan fay modeli, matematiksel tsunami simulasyonlarının giriş parametreleri olarak kullanılmış ve elde edilen sonuçlar DART kayıtçıları ve gel-git ölçerler tarafından kayıt edilen veriler ile karşılaştırılmıştır.

Ayrıca bu tez kapsamında elde edilen odak mekanizması çözümleri episantr uzaklığı 30^o den yakın uzaklıkta kaydedilmiş P- dalga şekillerinin ilk hareket yönleri kullanılarak kontrol edilmiş ve birbirleriyle uyumlu sonuçlar elde edilmiştir.

Bu yüksek lisans tezi kapsamında elde edilen sonuçlar, yitim (dalma-batma) zonları boyunca deprem aktivitesi dağılımını, depremlerin fay düzlemleri üzerinde meydana getirdikleri yırtılma yayılımlarının ayrıntılarını, deprem kaynaklı tsunamilerin deprem kaynak özelliklerini ve tsunami dalgalarının kıyıları nasıl etkilediğini anlamamıza katkı sağlamaktadır. Bu çalışmadan elde edilen sonuçlar bölgenin afet riski derecesini ortaya koymak adına ve gelecekte meydana gelebilecek afetler için önlem alma çalışmalarına referans olabilecek niteliktedir.

1. INTRODUCTION

1.1 Purpose and Content

The area studied within the scope of this MSc thesis is the west side of South American Plate where Nazca, Cocos, South American and Caribbean plates meet. In general, earthquakes which cause devastating tsunami waves mostly occur along the subduction zones where intense earthquake activity is observed (Figure 1.1). These earthquakes ($M_w \geq 7.0$) help us to investigate the geometry of subduction zones, the stress and deformation area and to understand the active tectonics of different regions. The main purpose of this M.Sc. thesis is to study source mechanisms of destructive subduction zone earthquakes ($M_w \geq 7.0$) and to simulate earthquake-induced tsunamis in detail particularly at the west side of South American plate, which is highly active in terms of seismicity and tsunami occurrence, hence to reveal the active deformation area and seismotectonic behavior of the region in the light of seismological and tsunami observations. In addition, demonstration of the importance of seismological parameters and necessity of high resolution bathymetry data in tsunami wave simulations and potential tsunami risk analysis is another goal to achieve. For this purpose, two large earthquakes with $M_w \geq 7.0$ that occurred near the South American plate in the last 5 years have been studied. The obtained results are presented for each earthquake in the order of teleseismic source mechanism solutions, slip distribution models and tsunami simulations. The following criteria were taken into account when selecting earthquakes to be studied by using teleseismic body wave modeling, slip distribution and tsunami modeling methods; earthquakes that are not studied comprehensively as in both earthquake source modeling and tsunami modeling together and their epicenters being in the ocean.

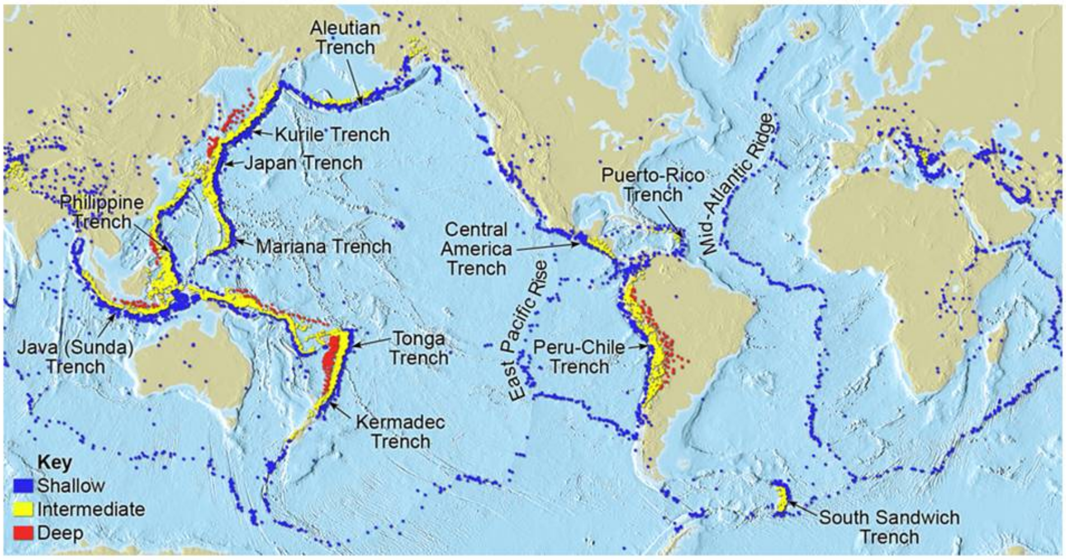

Figure 1.1 : Seismic activity distribution along the major subduction zones. The colors indicate focal depths of the earthquakes (taken from NOAA).

Within the scope of this thesis, the September 25, 2013 Acari - Peru (M_w: 7.1) and September 08, 2017 Chiapas - Mexico (M_w: 8.1) earthquakes were studied. Source mechanism parameters of those earthquakes were determined by using the MT5 (Moment Tensor 5) algorithm (McCaffrey et al., 1991; Zwick et al., 1994). Finite-fault slip distributions on fault planes were estimated by using the hybrid back-projection slip inversion code developed by Yagi et al. (2012a,b). In addition, tsunami simulations are conducted using the COMCOT tsunami code (Liu et al., 1998; Wang, 2009). Furthermore, software packages of Generic Mapping Tools (GMT; Wessel and Smith, 1998) were used to prepare the figures, and SAC (Seismic Analyses Code; Goldstein et al., 2003) was used to process conventional earthquake data. Besides, for all the figures and tsunami modeling, GEBCO-30 (General Bathymetric Chart of the Oceans) ocean bathymetry data with 30 arc-seconds resolution has been used. Teleseismic body waves used in this study are recorded by broad-band seismic stations of the International Federation of Digital Seismograph Networks (FDSN), the Global Digital Seismograph Network (GDSN), and archived at the IRIS-Wilber 3.

Another subject of this thesis is determination of various dynamic and kinematic earthquake parameters such as rupture time, the size of faulting area, stress drop, maximum and average displacement values from slip distribution models of these large subduction zone earthquakes (see Yagi et al., 2012a,b). The most important requirement for this is that the earthquake data has to be taken from a sufficient number of broad-band stations at teleseismic distances with good azimuthal distribution. By determining faulting geometry, slip distribution and tsunami wave propagation, the relationship between subduction processes, earthquake source and tsunami generation have been analyzed. With the numerical simulations made, it is aimed to reach results that show how the major destructive earthquakes, that may occur in the future, effect the whole Pacific coast.

1.2 Tectonic Features of the Study Area

Subduction zones are regions where two different convergent tectonic plates meet and one of them with lower density relative to other sinking beneath the other plate into the mantle (Figure 1.1). Substantial number of earthquakes occur on the interface between these two convergent plates. Depth of the earthquakes occuring on these zones vary depending on the length of the subduction. At deeper parts of the subduction zones, because of the increasing temperature and pressure by frictional forces, hot material starts to ascend. From this formation, volcanic arcs are generated at the back-arc basin of the subduction zone. On the subduction zones, usually a tectonic plate with oceanic crust and continental crust come across where one side of the subduction being on the ocean side. Shallow earthquakes observed on the flat slab of the subduction zones, often result in destructive tsunamis. For example, the March 11, 2011 Tohoku, Japan earthquake (M_{ww}=9.1), one of the largest intrumentally recorded earthquakes, occurred at a depth of 29 km and its epicentre being on the subduction zone between the North America and Pacific plates. This earthquake induced destructive tsunami waves throughout the Pacific ocean. Another example can be, the December 26, 2004 Sumatra earthquake (M_{ww}=9.1) that occurred between Burma microplate and Indian plate on a thrust fault at 30 km depth which resulted in a tsunami as well (see for details Taymaz et al., 2005 and USGS-NEIC earthquake catalogue). The South American Arc (Figures 1.2, 1.3 and 1.4) extends more than 7000 km from the Panama fracture zone to Chilean margin triple junction. It extends to the west of Caribbean Plate as interface between the Cocos and North American Plates and called Middle America Trench (Figure 1.5). Along this subduction zone, intense seismic activity with large magnitudes and dominantly vertical slip is observed, so earthquakes that occur in this region often caused tsunamis (Table 1.1). In general, the characteristics of subduction zones on the Earth such as crustal deformation, volcanic activity, the occurrence of large earthquakes and devastating tsunamis, are different. Earthquake source studies and numerical tsunami simulations are quite important for better understanding the general features of the subduction process, and also for modelling earthquake-induced tsunami initiation and wave propagation in open-ocean. By using tsunami simulation results, wave heights and arrival times of synthetic tsunami waves to several coasts are estimated.

In the south, oceanic crust of Nazca Plate subducts into the mantle under the South American Plate where the September 25, 2013 Acari - Peru (M_w 7.1) earthquake took place on the interface between them. Relative to the South American Plate, Nazca plate moves 80 mm/yr in the south and 65 mm/yr in the north to eastward direction in a reversed clockwise rotation (Hayes et al., 2015). As a result of this convergence intense seismicty (Figure 1.4), and uplift of Andes Mountains with volcanic activity are widely observed. Furthermore, there are deep-focus earthquakes, with focal depths greater than 600 km along the South American Arc, occurred due to the internal deformation of the subducting Nazca plate. Due to the asperities on fault planes, earthquakes reflect complex rupture characteristics (Bilek, 2010). There are also differences in slab geometry along the subduction zones from flat-slab to steep-slab. For example, on 24 November 2015, two deep-focus earthquakes (h: 606 km and h: 622 km) with magnitudes of 7.5 and 7.6 occurred within the subducted Nazca plate beneath eastern Peru (Ye et al., 2016). Along the South American Arc, the May 22, 1960 Valdivia - Chile earthquake (M_w 9.4 or 9.6), which is the largest instrumentally recorded earthquake in the world occurred, (Kanamori and Cipar, 1974; Cifuentes, 1989), for this reason it is especially important to study this subduction zone in order to understand the mechanism of earthquakes for hazard mitigation. Another example is the September 16, 2015 Chile earthquake (focal depth=26 km, dip angle (δ) = 25°) (see Yolsal-Çevikbilen et al., 2018) it is resulted in a destructive tsunami which is one of the simulated tsunamis for validating COMCOT code for tsunami simulations in this M.Sc. thesis. Furthermore, most of earthquakes occurred along the South American arc in past and instrumental period are clustered beneath the northern Chile and southwest of Bolivia, and decreases towards northern Peru and southern Ecuador at focal depths varying between 110 km and 130 km (Figures 1.2, 1.3 and 1.4; Hayes et al., 2015).

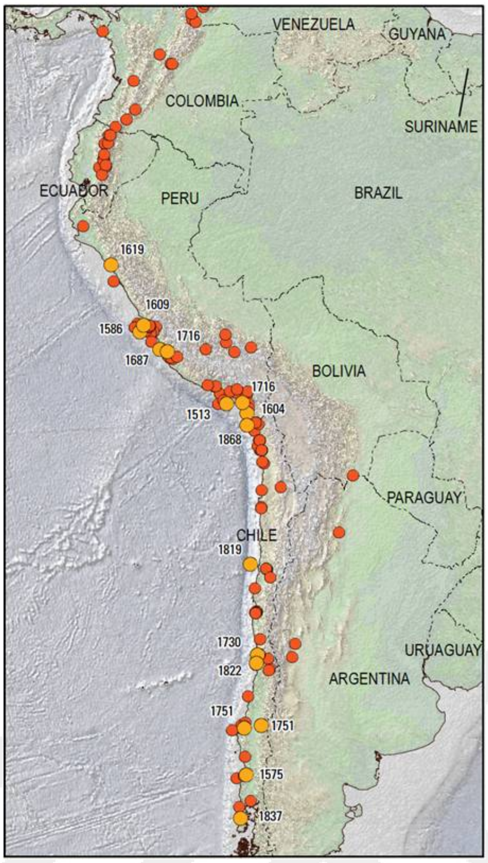

Figure 1.2 : Earthquakes occurred along the Peru-Chile Trench in the pre-intrumental period between 1500-1899 (taken from NOAA National Geophysical Data Center, 2010).

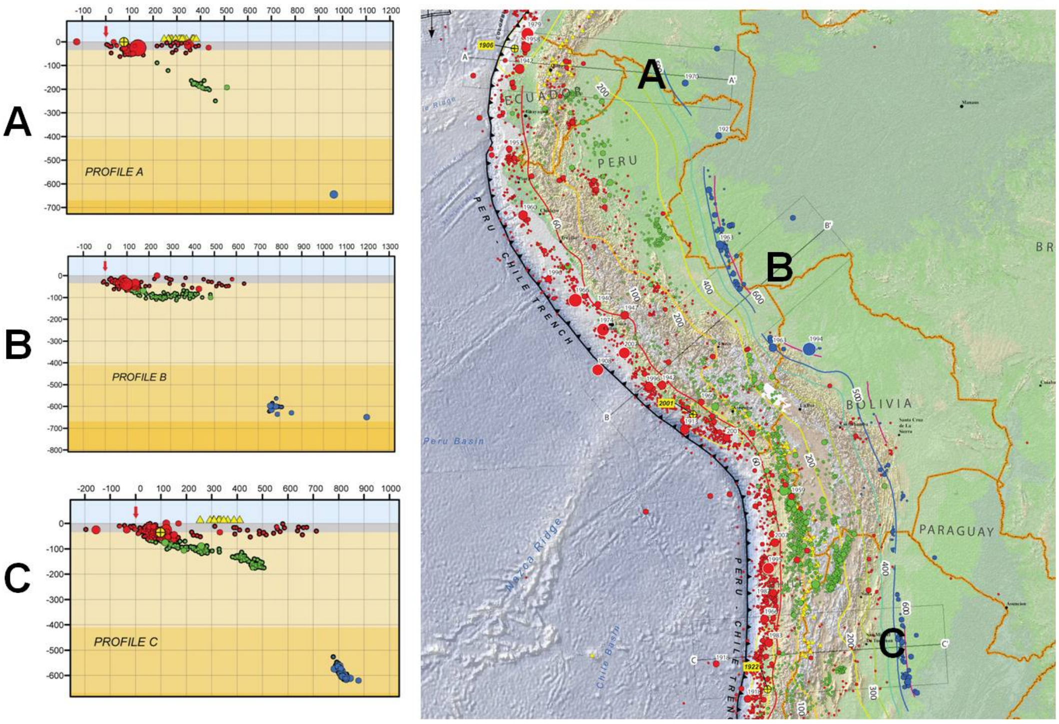

Figure 1.3 : Earthquakes occurred along the Peru-Chile Trench with A, B, C cross-section profiles for focal depths (Hayes and Wald, 2010).

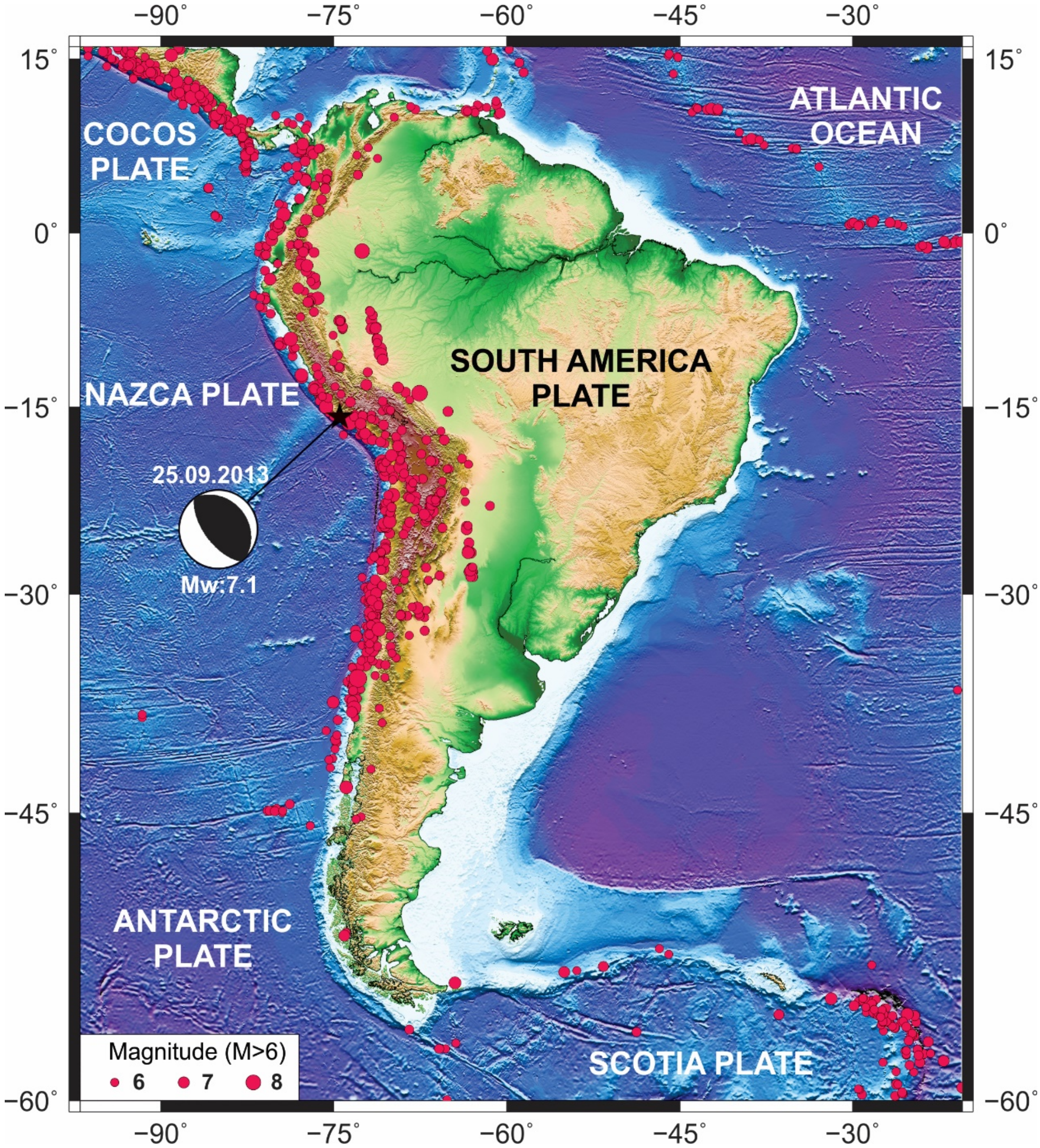

Figure 1.4 : Seismicity map of the South American Plate with the location (black star) and source mechanism solution of the September 25, 2013 Peru earthquake. Epicentres (M >6.0) are taken from USGS NEIC (1973 - 2018) earthquake catalogue. Bathymetry and topography data are also taken from GEBCO-BODC and ETOPO1, respectively.

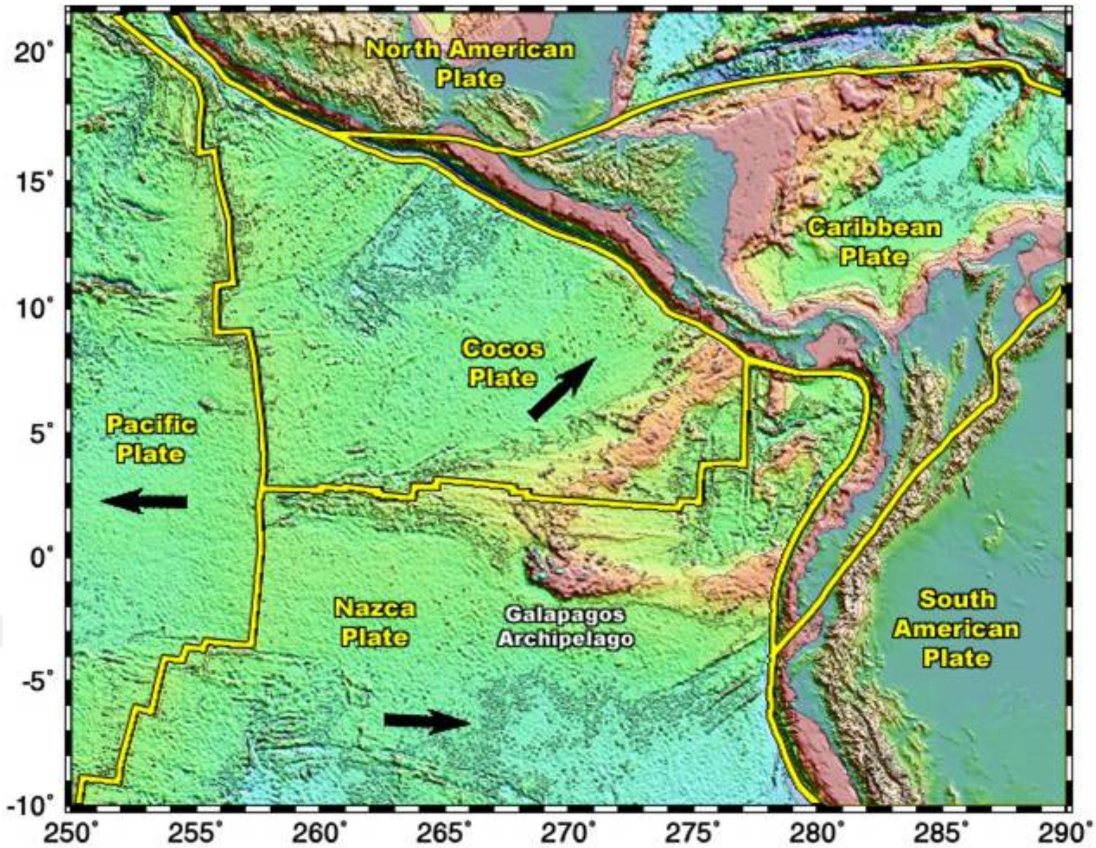

Figure 1.5 : Tectonic settings of the Middle America Trench (taken from the web page of https://pages.uoregon.edu). Bathymetric and topographic data compiled by Smith, W. H. F. and D. T. Sandwell (1997).

In the north, along the Middle America Trench (Figure 1.5), interactions between three tectonic plates control the active tectonic setting of this region: Caribbean plate, Cocos plate and North American plate (Figure 1.5). On 8 September 2017, Chiapas, Mexico earthquake (M_w 8.1) occurred in the center of the Cocos plate subducting beneath the North American plate along Mexico and Central America with a velocity of 6.4 cm/yr (Singh et al., 2000). As a result of this earthquake, minimum 98 people were killed around Oaxaca, and approximately 41,000 buildings were damaged so it is important to study this earthquake throughoutly (Ye et al., 2017). Since 1985 Mexico City and 1932 Jalisco earthquakes which occured at the west of Chiapas (Mendoza, 1993), this earthquake has the largest magnitude that occurred in Mexico. Because of the convergence of Cocos and North America Plates, intense seismic activity observed. The earthquake of 1787 (M_w 8.6), its epicentre being on the south of Mexico (Suarez and Albini, 2009), can be shown as an evidence of the convergence of Cocos and North American plates. There is no previously recorded major ($M_w > 7$) earthquake with thrust fault mechanism on the plate boundary for the last 100 years, so this aseismic zone, where the 2017 Chiapas (Mexico) earthquake occurred, is called Theuantepec Gap (e.g., Kelleher et al., 1973; Kelleher and McCann, 1976; Singh et al., 1981; Nishenko, 1991; Franco et al., 2005; McNally and Minster, 1981). According to Singh et al. (1981), Tehuantepec gap is an aseismic zone or it has a very large earthquake recurrence period. In Tehuantepec Ridge, age of the crust in the northwest is 10-25 Myrs younger than to the southeast (Couch and Woodcock, 1981; Pardo and Suárez, 1995). Subduction interface between the Cocos and Central America Plates converts from shallow dipping slab at Mexico to steeply dipping slab at Central America (Ponce et al., 1992). Rather than being an interplate event with thrust faulting, source mechanism solution of the 2017 Mexico earthquake (M_w 8.2) indicate normal faulting mechanism which specifies an intraplate event (Ye et al., 2017).

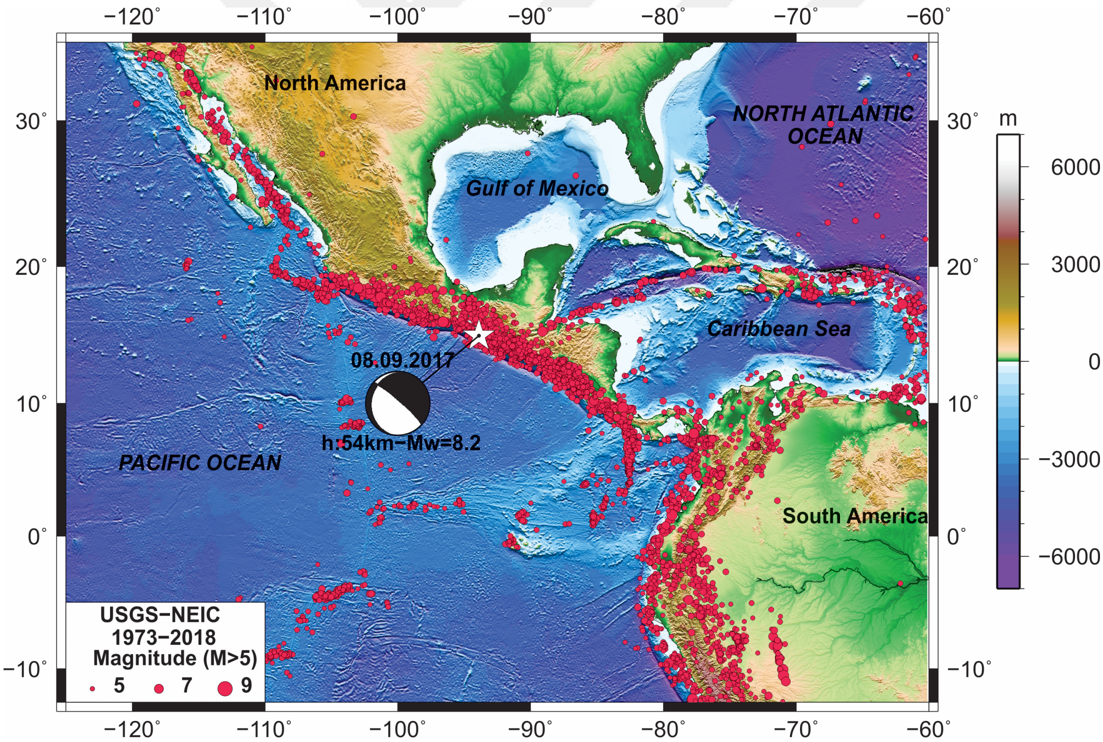

Figure 1.6 : Seismicity map of intersection between the Cocos, North America and Caribbean plates. Epicentres are taken from USGS NEIC (1973 - 2018) earthquake catalogue. Bathymetry and topography data are taken from GEBCO-BODC and ETOPO1, respectively. The location (white star) and source mechanism solution of the September 08, 2017 Mexico earthquake are also given.

Table 1.1 : Large earthquakes (M>8) occurred since 1900 along the South Amercian Arc (taken from USGS-NEIC earthquake catalogue). M_{ww}: Moment w-phase M_{wc}: Centroid moment tensor Moment magnitude.

Date	Time	Latitude (°N)	Longitude (°E)	Depth (km)	M	Type	Location
16.09.2015	22:54:32	-315.729	-71.744	22.44	8.3	M_{ww}	Chile
01.04.2014	23:46:47	-196.097	-70.691	25	8.2	M_{ww}	Chile
27.02.2010	06:34:11	-36.122	-72.898	22.9	8.8	M_{ww}	Chile
15.08.2007	23:40:57	-13.386	-76.603	39	8.0	M_{wc}	Peru
23.06.2001	20:33:14	-16.265	-73.641	33	8.4	M_{ww}	Peru
30.07.1995	05:11:23	-23.340	-70.294	45.6	8.0	M_w	Chile
09.06.1994	00:33:16	-13.841	-67.553	631.3	8.2	M_w	Bolivia
03.03.1985	22:47:07	-33.135	-71.871	33	8.0	M_w	Chile
31.07.1970	17:08:05	-1.597	-72.532	644.8	8.0	M_w	Colombia
17.10.1966	21:42:00	-10.665	-78.228	40	8.1	M_w	Peru
22.05.1960	19:11:20	-38.143	-73.407	25	9.5	M_w	Chile
21.05.1960	10:02:57	-37.824	-73.353	25	8.1	M_w	Chile
09.12.1950	21:38:51	-23.977	-67.912	113.9	8.2	M_w	Chile
06.04.1943	16:07:17	-31.432	-71.475	35	8.1	M_w	Chile
24.08.1942	22:50:32	-14.819	-74.708	30	8.1	M_w	Peru
24.05.1940	16:33:59	-11.094	-77.487	45	8.2	M_w	Peru
11.11.1922	04:32:51	-28.293	-69.852	70	8.5	M_w	Chile
17.08.1906	00:40:04	-32.400	-71.400	35	8.2	M_w	Chile
31.01.1906	15:36:10	0.955	-79.369	20	8.8	M_w	Ecuador

1.3 Literature Review

Seismological studies provide detailed earthquake characteristics and source rupture models by evaluating elastic waves that moves through the Earth. In general, teleseismic, regional and local earthquake data can be used to determine source mechanism parameters using moment tensor inversion methods. For instance, McCaffrey et al. (1991) developed a code called SYN4 that uses teleseismic body waveforms in order to calculate double-couple solutions of eathquake sources. Nabelek (1984) added the feature which provides moment tensor solutions and called it as MT5. Taymaz et al. (1991a, 1991b) studied the motion of Anatolian plate relative to Eurasia and the extension regime in and around the Aegean Sea. They aimed to have better estimation of focal parameters by using the inversion algorithm of MT5 which are based on the determination of theoretical seismograms for P- and SH- waveforms from a given Earth model of the point source defined in terms of earthquake source parameters. They compared the shapes and amplitudes of waveforms, recorded in teleseismic distances, with synthetic waveforms (see also Nabelek, 1984; Taymaz et al., 1990, 1991, 2007, 2008; McCaffrey et al., 1991; Zwick et al., 1994; Yolsal et al., 2007; Yolsal-Çevikbilen and Taymaz, 2012; Fielding et al., 2013; Yolsal-Çevikbilen et al., 2014; Saltogianni et al., 2015). They concluded that focal mechanism solutions of earthquakes occurred in the western part of the Aegean region show dominantly normal faulting mechanisms with WNW striking and slip vectors directed NNW to NNE. Besides, Yagi et al. (2012b) developed a hybrid back-projection method which uses BB P- waveforms that integrates pP and sP phases with reflected phases from discontinuities at the source and uses it to estimate finit-fault slip distribution model of the ruptured area. By using earthquake source mechanism parameters earthquake-induced tsunamis can be numerically simulated, and this is a common practice among Tsunami Hazard Mitigation studies. After constraining the fault model, the vertical dislocation of the ocean bottom can be calculated, and it is used for modelling the initial tsunami wave. For example, Yolsal-Çevikbilen et al. (2018) inverted teleseismic long-period (LP) P- and SH- waveforms to determine source mechanism solutions and finite-fault slip distribution models of the October 28, 2012 Haida Gwaii (M_w 7.7) and the September 16, 2015 Chile (M_w 8.3) earthquakes, and then they numerically simulated tsunami wave propagation related to those earthquakes. There are several tsunami simulation codes (i.e., COMCOT, SWAN, NAMI-DANCE TUNAMI-N2) which are commonly used in literature (see Yolsal-Çevikbilen et al., 2018; Sözdinler et al., 2015; Calisto et al., 2017; Oishi et al., 2015). Cornell Multi-grid Coupled Tsunami modelling package (COMCOT), developed by Liu et al. (1998) used in this MSc. thesis, it is one of the codes that can be used to determine wave heights and arrival times of tsunami waves.

Until now, active tectonics of the Middle America Trench and Peru-Chile subduction zone is extensively studied by many researchers. For example, Lim et al. (2018) defined subduction features of the Nazca Plate by relocating intraslab earthquakes in southern Peru and then they analyzed the relation with the seismicity of the region. They also provided P- wave and S- wave velocity models for the subducting Nazca plate. From the results of relocated seismicity, they inferred smooth bending in the transition between shallow flat dipping (30^o) interface to the northwest and a 30^o dipping interface to the southeast along the ~400 km transition zone. Furthermore, they detected high S- wave velocities and low Vp/Vs above flat slab, showing that it has cold and dry environment. Besides, Ruiz et al. (2018) re-analyzed historical earthquake archives of Chilean region to understand the general characteristics of earthquakes and seismic gaps along the subduction zone. Also they emphasized the importance of the better assessment of the historical earthquake locations in order to study tsunami effects. They concluded that there is a substantial difference between earthquakes that rupture along the entire plate from surface to the bottom and more frequent M_w ~8 events that break lower part of the fault plane. The megathrust earthquakes with magnitudes of at least 8.4 occurred in this region usually produce destructive tsunamis. They occur two times for every 100 years along the Peru-Chile trench (Ruiz et al., 2018). Condori et al. (2017) also investigated the crustal thickness and Vp/Vs ratio beneath northern Peru using receiver function method with teleseismic broad band seismic stations. They identified the P -to -S conversion and their reflected phases using H-k stacking technique. Their results showed that the Moho depth changes drastically starting west towards east, showing shallower depths of approximately 25 km near the coast, and maximum depth of 55-60 km beneath Andean Cordillera. In the Amazonian Basin further east this extends to 35-40 km. Finally, they found bulk crustal Vp/Vs ratio values for Eastern and Western Cordilleras and positive relationship between crustal thickness, Vp/Vs ratio, the Bouguer anomaly, and topography for different parts of Peru.

Up to now, the September 08, 2017 Chiapas (Mexico) earthquake (M_w 8.2) and related tsunami has also been studied by many researchers (e.g., Adriano et al., 2017; Jimenez et al., 2018; Okuwaki and Yagi, 2017; Gusman et al., 2017; Ramirez-Herrera et al, 2017; Ye et al., 2017; Heidarzadeh et al., 2018; Spagnotto et al., 2018; Chacón-Barrantes, 2018). Jimenez et al. (2018) investigated source characteristics of

2017 Chiapas-Mexico earthquake using teleseismic body waveforms and the numerical scheme of Kikuchi and Kanamori (1991), and they obtained a slip distribution model of the fault plane. Their results indicated a normal faulting mechanism within the Cocos plate, with a high dip angle for a depth of 59 km. They used 51 seismic stations for teleseismic point-source modeling. For the finite-fault slip inversion they used 75 seismic stations at teleseismic distances. They found that the rupture extends to northwest with a maximum slip value of 14.5 m. Okuwaki and Yagi (2017) also constructed a source model for 2017 Chiapas (Mexico) earthquake by using 28 teleseismic P- waveforms and suggested that this earthquake occured on a steep normal fault with major slip occuring on the shallow depth of 28 km. Their results showed that the primary cause of this earthquake is the downdip extensional stresses. According to their study, the rupture speed abruptly decelerated at the northwestern end of the fault plane where it crosses the Tehuantepec Fracture Zone. From this information it can be inferred that this fracture zone denied further rupture propagation. The study of Adriano et al. (2017) conducted tsunami simulation using homogenous fault model for understanding the tsunami characteristics near the rupture zone. After that they estimated a finite-fault slip distribution model by inversion of tsunami waveforms. Also, Gusman et al. (2017) analyzed tsunami waveforms recorded at tide gauge stations for estimating the optimum sea surface displacement. Ramirez-Herrera et al. (2017) found a finite-fault source model based on W-phase moment tensor inversion by Servicio Sismologico Nacional (SSN). After that they used analytical solutions of Okada (1985) for estimating seafloor deformation. They also reported runup distribution along the 41 km Chiapas coast and other coastal villages by doing a survey investigation. Ye et al. (2017) also inverted W-phase data for finding point-source model of the 2017 Chiapas earthquake for finding faulting geometry, depth and seismic moment. Then, they used P- wave first arrival times on regional seismograms to relocate the hypocenter. By using the relocated hypocenters, they conducted teleseismic short-period P-waveform back-projection method for the west of North America. Heidarzadeh et al. (2018) applied teleseismic body-wave inversions using rupture velocities between 1.5 and 4.0 km/s for 2017 Chiapas earthquake and then they conducted tsunami simulations. Spagnotto et al. (2018) analyzed static Coulomb criterion, stress change and gravity structure of the offshore forearc zone and its relation with the rupture structure. The study of Chacon-Barrantes (2018) analyzed the 2017 Chiapas tsunami using only the Quepos tide gauge. They simulated tsunami real-time data for only this station using the code of Community Model Interface for Tsunami (ComMIT). They also conducted a post-tsunami simulation to compare the consistency of synthetic data with the real-time observations at Quepos tide gauge station.

2. DATA AND METHODS

2.1 Teleseismic P- and SH- Waveform Modeling

By inverting teleseismic waveforms with inversion methods, kinematic and dynamic features of an earthquake can be determined. These methods are based on the fact that a seismogram can be generated by the interaction of linear filters representing the various properties of the source and the medium that seismic waves propagate through (source mechanism parameters, rupture time and rupture velocity, seismic wave velocity and density etc.). Modeling of the earthquake source and slip distribution on the fault plane play important roles in understanding of the occurrence mechanisms of earthquakes, revealing the rupture geometry, spatio-temporal behavior of the rupture and stress distributions in the region. By analyzing earthquake data, active tectonic structures of a region can be examined in detail, and earthquake risk analysis can be done. Generally, waveform modeling techniques assume that earthquake source acts as a point-source. With this, distribution of forces acting at the hypocenter are given as single-force, equal and opposite double-couple, double-couple rotating around z-axis (Type-I), double-couple rotating reverse around z-axis (Type-II). However, it is more convenient to use the force pairs called Type-I and Type-II for the purpose of describing an earthquake source because they can identify the shear motion that occurs during the faulting process (Kasahara, 1981; Stein and Wysession, 2003).

In seismology, data sets with different frequency ranges are used. For example, reflection seismology deals with high frequencies, however, for studies about crustal deformation, low frequencies are taken account (Figure 2.1). The comparison of P-wave first motion polarities is a much weak method for determination of earthquake source mechanism parameters (i.e., strike, dip and rake angles of nodal planes, focal depth, seismic moment) and their uncertainty rates, compared to the methods using different seismic wave phases and their respective amplitudes.

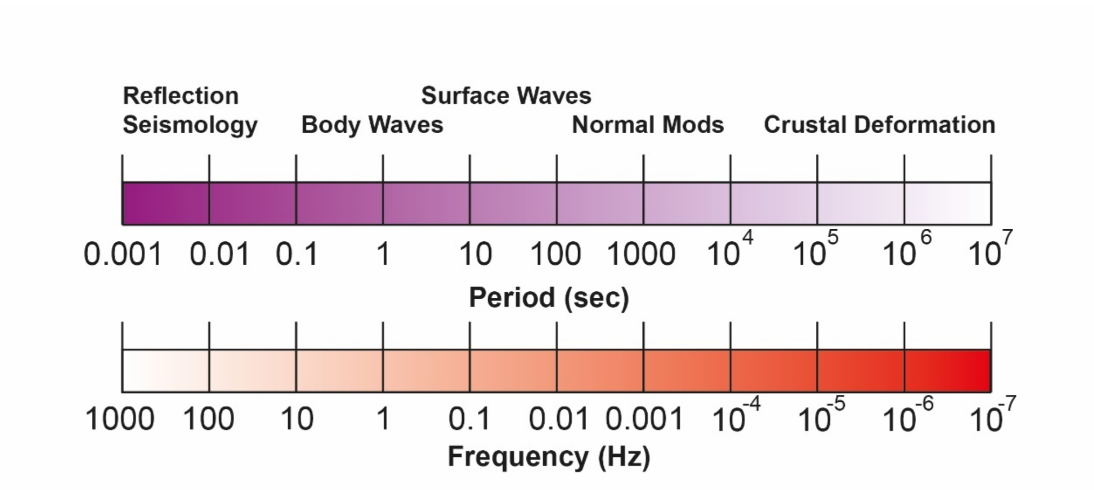

Figure 2.1 : Frequency ranges used in seismological studies (taken from Stein and Wysession, 2003).

By analyzing earthquake data recorded at seismic stations distributed all over the world using various inversion techniques, kinematic and dynamic source parameters of an earthquake can be easily determined. In inversion process, body waves recorded at teleseismic stations (30° ≤ Δ ≤ 90°), which rather suitable for studying earthquake source characteristics, are commonly used (Nabelek, 1984; Taymaz, 1990; Taymaz et al., 1990, 1991; Tan, 2004; Yolsal, 2008). At first step, synthetic waveforms are calculated, and then they are compared with the observed ones in terms of wave shapes and amplitudes.

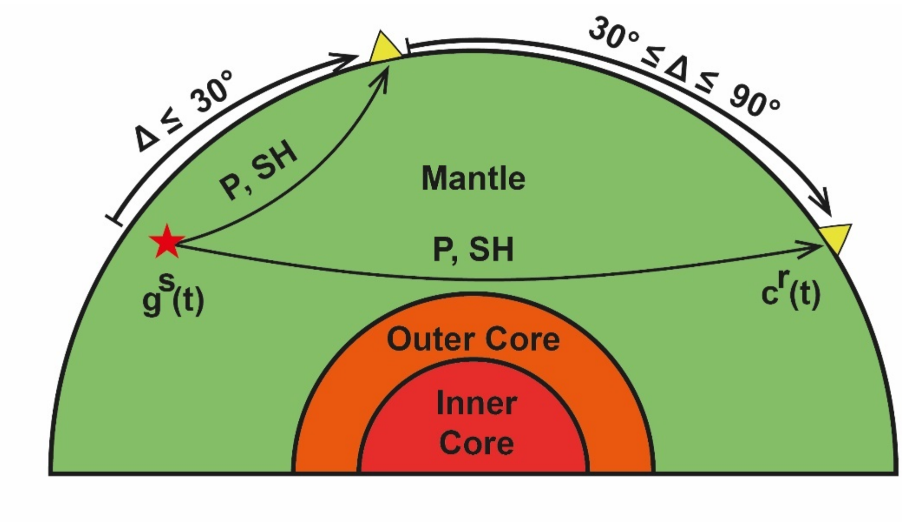

Figure 2.2 : Schematic representation of the source model used for calculating the Green's Function of teleseismic body waves. Δ: epicentral distance, g^s (t): the crustal effect at the source area, c^r (t): the crustal effect under the seismic station (taken from Nàbelek, 1984; Taymaz, 1990; Yolsal, 2008).

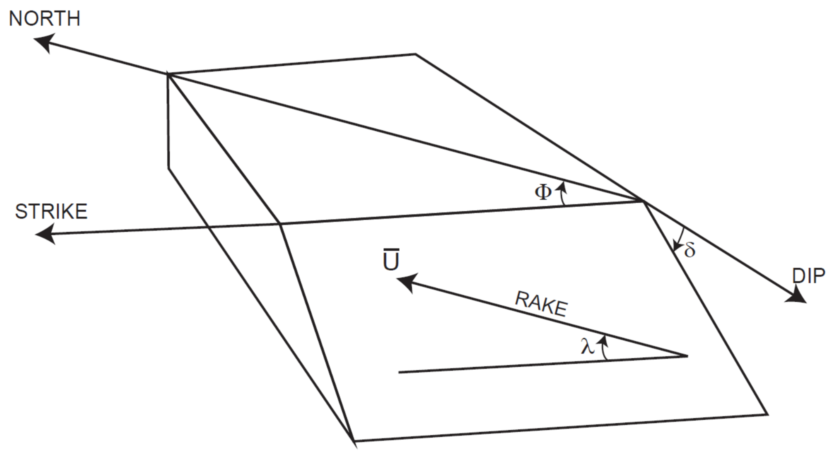

Figure 2.3 : Fault mechanism parameters describing the faulting geometry at source. Strike (φ), dip (δ) and rake (λ) angles are described on a schematic fault plane. U denotes the displacement vector (Aki and Richardson, 1980).

The strike (φ) angle is the angle measured clockwise from the north and varies between $0 \leq \varphi \leq 2\pi$. The dip (δ) is the angle between the fault plane and the horizontal plane, between $0 \leq \delta \leq \pi/2$. The rake (λ) angle is defined as the angle between the strike and the slip motion on the fault plane. It changes between $-\pi \leq \lambda \leq \pi$ and is used to describe the fault type depending on the value. For example, if $\lambda = 0$, the fault is defined as left-lateral strike-slip, if $\lambda = \pi$ than it is defined as right-lateral strike-slip fault (Figure 2.3; Aki and Richards, 1980).

The most important and complex function calculated in waveform modeling methods is the Green’s Function, which is also called the impulse response function. Since it expresses various wave propagation effects such as reflection phases, mode transformations, geometric spreading, non-elastic attenuation, scatterings and refractions, it is expressed intricately. Diversity of tensile forces that causes earthquakes creates variance in the rupture mechanism at the earthquake source, geometry of the fault plane and the slip over it. Relative travel times for different phases are related to the depth of hypocenter of the earthquake and the distance between the source and the station. The distance between the source and the station is controlled by the ray parameter or the take-off angle (Lay and Wallace, 1995). The source-time function obtained by plotting the normalized moment value with respect to time can be simple or complicated relative to the homogeneity of the source area. Source-time function which presents the rupture behavior in time can be identified as a series of isosceles triangle functions (Taymaz, 1990).

In teleseismic waveform modeling method, double-couple approach which consists of two forces opposite to each other with a little distance between them is used, and it is assumed that the medium is point-source, linear, homogeneous, elastic and isotropic. Some undesirable effects such as noisy data, weakness of the modeling method etc., may cause some dissimilarity of the source from the double-couple approach. In this case, the seismic moment tensor approach, which is another representation of the seismic source, can be used to overcome these problems and to calculate the non-double-couple components. The non-double-couple components are resulted from several factors such as volcanic earthquakes, effects from geothermal sources, deep focused events, ruptures in non-horizontal sources (Dziewonski and Woodhouse, 1983), and the presence of shallow structures and anisotropy near the source (Kawasaki, 1982; Trèhu and Solomon, 1983) (Sipkin, 1986; Jost and Herrmann, 1989; Julian et al., 1998; Stein and Wysession, 2003). These components, which are generally found in almost all earthquakes, can only be accurately detected when high-resolution data is used. The seismic moment tensor approach consists of 9 moment tensor components shown as two double-couple forces at a distance of d from each other, and the resulting net force is always 0 (Figure 2.4; Aki and Richards, 1980).

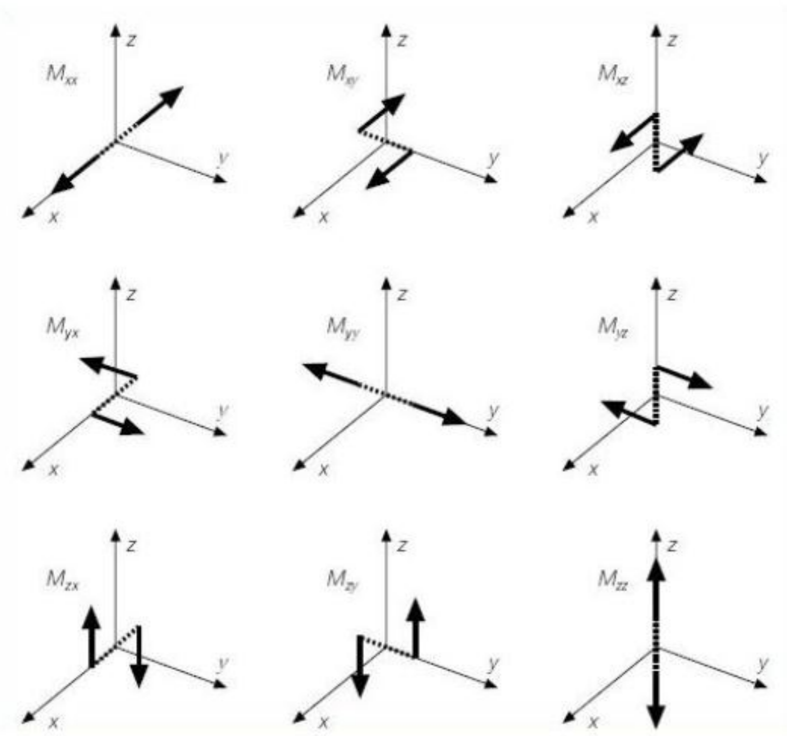

Figure 2.4 : Components of moment tensor matrix consisting of 9 different force couples (Aki and Richards, 1980; Stein and Wysession, 2003).

Moment tensor components can be calculated by using source mechanism parameters as given below (Aki and Richards, 1980).

$$M_{xx} = -M_0(\mathrm{Sin}\delta\mathrm{Cos}\lambda\mathrm{Sin}2\phi + \mathrm{Sin}2\delta\mathrm{Sin}\lambda\mathrm{Sin}^2\phi) \quad (2.1)$$

$$M_{yy} = M_0(\mathrm{Sin}\delta\mathrm{Cos}\lambda\mathrm{Sin}2\phi - \mathrm{Sin}2\delta\mathrm{Sin}\lambda\mathrm{Cos}^2\phi) \quad (2.2)$$

$$M_{zz} = M_0(\mathrm{Sin}2\delta\mathrm{Sin}\lambda) \quad (2.3)$$

$$M_{xy} = M_0(\mathrm{Sin}\delta\mathrm{Cos}\lambda\mathrm{Cos}2\phi + 0.5\ \mathrm{Sin}2\delta\mathrm{Sin}\lambda\mathrm{Sin}2\phi) \quad (2.4)$$

$$M_{xz} = -M_0(\mathrm{Cos}\delta\mathrm{Cos}\lambda\mathrm{Cos}\phi + \mathrm{Cos}2\delta\mathrm{Sin}\lambda\mathrm{Sin}\phi) \quad (2.5)$$

$$M_{yz} = -M_0(\mathrm{Cos}\delta\mathrm{Cos}\lambda\mathrm{Sin}\phi - \mathrm{Cos}2\delta\mathrm{Sin}\lambda\mathrm{Cos}\phi) \quad (2.6)$$

In this thesis, P- and SH- waveforms recorded at teleseismic (far field) stations have been processed through various stages, and they are prepared to be modeled in order to determine source mechanism parameters of earthquakes occurred along the major subduction zones. The MT5 algorithm developed by Zwick et al. (1994) is used in order to find source mechanism parameters. It is adapted from SYN4 (McCaffrey et al., 1991) by adding double-couple and the moment tensor solutions of the earthquake based on the inversion of teleseismic waveforms, which is the next version of SYN 3 adapted from Nàbelek (1984) by McCaffrey and Abers (1988). Three component LP (long period) and BB (broadband) earthquake data are downloaded from IRIS-Wilber 3 web page (*https://ds.iris.edu/wilber3/find_event*) for a time interval in a SEED file format *(The Standard for the Exchange of Earthquake Data)*. SAC (*Seismic Analysis Code*, Tapley and Tull, 1992, Goldstein et al., 1999) is used for analysis of earthquake data. The waveforms and instrument responses are extracted by using *rdseed (read seed)* command. All of the data processing steps conducted for preparing earthquake data to be used in MT5 algorithm are summarized in Figure 2.5.

In inversions, it is assumed that the source is double-couple and point source. The P- and SH- waveforms and the reflected pP, pS and sS reflection phases from that comes from the surface are analyzed. Wave amplitudes are adjusted relative to geometric scattering and non-elastic attenuation factors. For attenuation, the t*, called the Futterman's Q operator, was taken as 1 s and 4 s for P- and SH- waves, respectively and assumed as constant for teleseismic distances (Futterman, 1962). The weighting of the teleseismic stations used in the inversion was done by taking into account the average relative amplitudes of the waves, their wave type and their distribution over the focal sphere. Since displacement records are usually used in waveform modeling studies, the current velocity records have been converted into displacement records. For this purpose, the response function of each velocity record is removed from the records by deconvolution and then re-convolved with another instrument response function representing the displacement record. In this study, the long-period WWSSN instrument response (oscillations 15 sec and maximum amplification T=14.4 sec 0.07 Hz) with appropriate bandwidth was used for converting the velocity records to displacement record (see McCaffrey and Nàbelek, 1987; Plesinger et al., 1996; Tan, 2004; Yolsal, 2008). In order to calculate theoretical travel times of P- and SH- waves, Preliminary Reference Earth Model (PREM) was used (Dziewonski and Anderson, 1981).

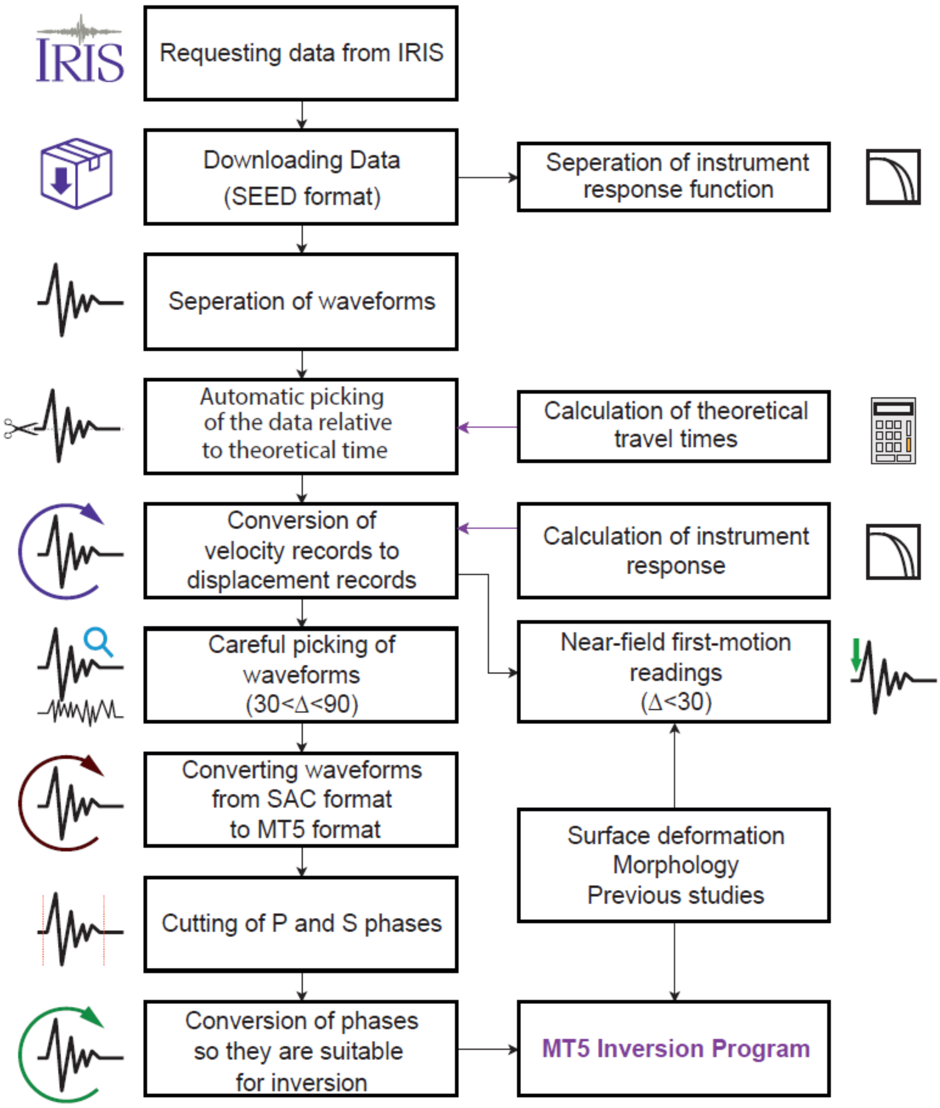

Figure 2.5 : Data processing steps conducted for teleseismic waveform inversion (re-drawn from Tan, 2004; Yolsal, 2008).

The other details of this method can be found in Taymaz (1990), Taymaz et al. (1990, 1991), Tan (2004), Yolsal-Çevikbilen and Taymaz (2012), Fielding et al. (2013), Saltogianni et al. (2015, 2017) and Yolsal-Çevikbilen et al. (2014).

2.2 Hybrid Back-Projection Slip Distribution Inversion

Using waveform modeling and inversion techniques, rupture propagation/ slip distribution on the fault plane, multiple rupture events and asperity and barrier formation can be examined (Figure 2.6). For modeling of slip distribution and rupture processes on a fault plane within the scope of this thesis, the hybrid back-projection inversion algorithm developed by Yagi and Kikuchi (2000) and Yagi et al. (2012b) was used. Earthquake data are downloaded from IRIS-Wilber 3. Hybrid back-projection method, used for determining finite-fault slip model of an earthquake, is a method that estimates seismic energy release in space and time This method uses P-waves to combine Pp, sP phases with reflected phases from discontinuities near the source. Since P-wave trains originated from shallow events combine pP and sP phases, it is problematic to receive high-resolution back-projection results without dealing with this interference, notably when analyzing low-frequency data. Supposing that the cross-correlation of an observed waveform (Equation 2.7) should be large at every observation station, thus allowing us to detect in principle the locations and timing of sub-events (Yagi et al., 2012a).

The cross-correlation function is calculated for each station *j*;

$$w_j(x,t) = \frac{\int_0^T u_j(\tau+t)\cdot g_j(x,\tau)dt}{U_j\sqrt{\int_0^T g_j^2(x,\tau)dt}} \tag{2.7}$$

with

$$U_j = \max_{0<\alpha<T}\sqrt{\int_0^T u_j^2(\tau+\alpha)d\tau} \tag{2.8}$$

where x is location, t is time of the sub-event, u is observed waveform at the station and g corresponds to theoretical Green's function. T is duration of two waveforms. Next *N*-th root of *w* for each station is applied all stations for obtaining beam trace s(x,t) (Rost and Thomas, 2002).

$$s(x,t) = \sum_{j=1}^{j} A_j \left| w_j(x,t) \right|^{1/N} \frac{w_j(x,t)}{|w_j(x,t)|} \qquad (2.9)$$

$$S(x,t)s = |s(x,t)|^{N} \frac{s(x,t)}{|s(x,t)|} \qquad (2.10)$$

Positive values of *S(x,t)* means that positive slip-rate at location *x* and time *t*, negative values are not taken in to account.

As a result of modeling of the waveforms with the inversion, the dimensions of the fault area (length, width), seismic moment drop, maximum and average displacements, stress drop and rupture time are obtained.

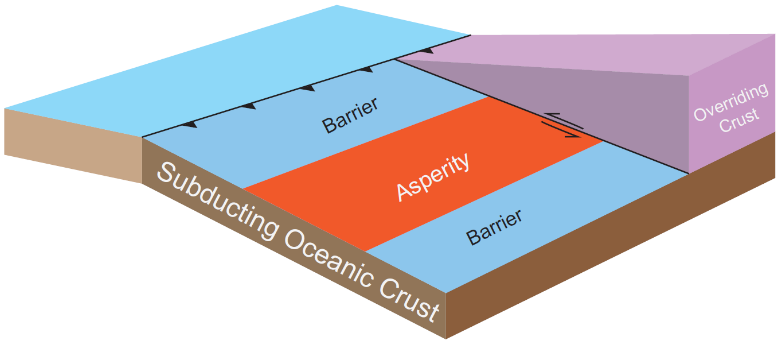

Figure 2.6 : A schematic illustration for the locations of asperity and barriers on a subduction zone.

In order to determine the spatio-temporal distribution of slip made by rupture process, the fault plane is divided by the number of M × N patches with, xx length and yy width (Figure 2.7). Number and size of sub-faults are estimated primarily by the size of the earthquake and Wells and Coppersmith (1994) empirical relation. General information about slip distribution on a fault plane should be acquired by initially dividing fault plane into several sub-faults which is enough to represent the faulting area. Afterwards, more detailed information can be obtained about the area by reducing the faulting area (increasing the resolution) of the slip (Figure 2.7; Yagi et al., 2012a,b).

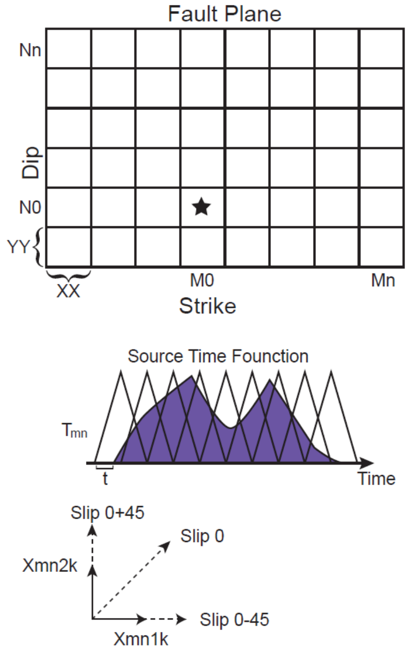

Figure 2.7 : A schematic diagram showing source location. Fault plane is divided into multiple smaller slip patches. Moment function is calculated for mn number of fault planes. T_{mn} is determined from maximum rupture velocity and describes the initiation time of source-time function for each smaller fault plane (Yagi and Kikuchi, 2000; Yagi et al., 2003; Tan, 2004; Tan and Taymaz, 2006).

Source mechanism parameters estimated by teleseismic P- and SH- body waveform modeling are used as input parameters for hybrid back-projection slip algorithm. The rake angle can be selected as fixed or free during inversion. In this study, the size of the sub-faults in the modeling is generally chosen to be between 16 and 25 km². During the selection of sub-fault size, earthquake magnitude, frequency contents of the records used and the rupture time are taken into consideration. For each grid, the source-time function, which consists of L number of triangle function series with t rise time, is calculated and the slip vector is divided into two components perpendicular to each other (see Figure 2.7; Yagi and Kikuchi, 2000).

For earthquakes, it is seen that homogeneous fault models with a uniform slip and constant rupture rate on the fault plane are not realistic. For example, events such as rupture stopping at a point along the fault plane, changing the direction of propagation, jumping and bending etc., are indicative of the absence of homogeneous ambient conditions. Asperity and barrier concepts were introduced in order to explain these movements (Lay and Wallace, 1995). Asperities are regions where high amount of slip and stress-drop (and the strain) are observed on the fault plane, which causes the spread of the high-frequency seismic energy and the stress-drop. These regions can be determined in detail by analyzing near-field strong-motion data. Another heterogeneity indicator that can be observed on the fault plane is the so-called barrier, which is a high-strength zone that makes difficult for the propagation of the rupture. Rupture stops when it reaches to the barrier, it continues behind it if it is durable enough not to break. Thus, an unruptured zone is left on the fault plane after the earthquake. In general, it can be said that asperities are associated with foreshocks and barriers with aftershocks. Furthermore, a durable barrier that stops rupture may then act as asperity for a future earthquake (Lay and Wallace, 1995).

In inversion process, teleseismic (far field) BB P- waveforms with high signal to noise ratios and good azimuthal distributions on focal spheres are used. Waveforms were converted to displacement records before the inversions. Earthquake source mechanism parameters obtained by P- and SH- waveform modeling and a velocity-depth model has been used to calculate the Green's Functions for all stations and synthetic waveforms. As a velocity-depth model, Preliminary Reference Earth Model (PREM) was used in slip inversion (Dziewonski and Anderson, 1981).

2.3 Numerical Tsunami Simulations

2.3.1 Generation, propagation and modeling of tsunami waves

Tsunamis are produced mainly due to the severe and sudden submarine uplift or subsidence in the oceans and coastal areas. They are large wave series with long wavelength and period. For occurrence of tsunami waves, a large body of water must be instantly displaced. When there is a vertical movement, the amount of water gains a potential energy. In order to gain equilibrium state, this potential energy converts into kinetic energy, and then tsunami waves begin to propagate in horizontal direction. Earthquake-induced tsunamis occur when there is a vertical dislocation in the ocean bottom. Therefore, earthquakes with lateral slip usually do not induce tsunamis. In this context, the possibility of tsunami formation is low in regions where strike-slip faults are observed.

Modeling of earthquake-induced tsunamis gives valuable information about tsunami hazard mitigation and plays an important role for checking whether the modelled earthquake source is consistent with real-time tsunami records or not. Numerical modeling provides us arrival times and wave amplitudes of tsunamis, run-up values and inundation areas. The simulation results also provide detailed information about vulnerable coastlines, inunduation maps for flooding and preparing scenarios for possible tsunamigenic earthquakes.

The velocity of tsunami waves are related to the water depth they are going through, and depending on the bathymetry waves can refract, reflect and diffract (Murata et al. 2010). They have long wave length so these waves cannot be felt in open ocean. Because of the complexity of the ocean bottom increases with shoaling it is important to have high resolution bathymetry in order to have good results for tsunami simulations. When they reach the coastlines, their wave length becomes shorter and their amplitudes become larger due to the shallowness of water as tsunami propagates onto a continental shelf. Depending on the wave height, wave energy also increases, so that the waves with high energy reaching the shore become destructive waves and leads to damage in that area. These waves travel in wave trains containing several large waves. Most destructive earthquake-induced tsunamis occur because of shallow focused large earthquakes ($M > 7.0$) with vertical slip. These earthquakes usually occur along the subduction zones where intense seismic activity and deformation observed. Tsunamis can also be induced due to volcanic sources or sudden movement of a large body (landslides) in ocean (Tinti et al., 1999).

In order to calculate initial tsunami wave related to an earthquake, it is necessary to generate a source model indicating how the seafloor displaced. After the estimation of earthquake fault mechanism, the elastic dislocation theory developed by Okada (1985), with either single (uniform) or multiple (non-uniform) fault segments, is adopted to evaluate the seafloor deformation caused by an earthquake. When it is presumed that the slip is uniform, the amount of the seafloor displacement is calculated as the slip and rake is same at the whole fault plane. Fault length and width, depth of the epicentre, epicentre coordinates, strike, dip, and rake of the fault plane are used as input for uniform tsunami simulations. For non-uniform slip model, unlike uniform model, fault is divided into number of sub-faults each having different rake and slip values. After calculating seafloor deformation, initial tsunami wave is modeled by assuming the uplift of the ocean-bottom is same with the initial wave height. Since tsunami waves have long wave length, they feel the ocean bottom while they propagate, so they have a strong relation with bathymetry. Hence, it is only possible to determine parameters such as the maximum wave heights on the coasts and run-up, using high resolution bathymetry data (Geist, 2000).

In this thesis, Cornell Multi-grid Coupled Tsunami Model (COMCOT) is used, for conducting numerical tsunami simulations (Liu et al., 1998; Wang, 2009). The methodology includes modeling of the initial wave height, simulation of tsunami wave propagation and calculation of the maximum wave heights at several coastal areas. Tsunami wave propagation and the major effects of tsunami waves on nearby coastal plains are simulated by calculating the vertical dislocation on the seabed based on the obtained earthquake source parameters and non-uniform slip models from teleseismic waveform inversions. Then, tsunami simulation results have been compared with the available real-time tide gauge records located on near-field coastal plains and DART buoy records.

Tide gagues also known as mareographs are devices that measures and records sea level change at coastal areas with respect to a reference heigth for a period thus showing the sea level change over time. Modern tide gauges transmit the data to a satelite so the data is avaiable worldwide. The measurement can be used to calculate mean sea level. DART buoys, unlike tide gauges are positioned at the open-ocean. A buoy at the surface connected to a pressure recorder (barometer) located at the bottom of the ocean. At the open-ocean, since the complexity of the bathymetry is lesser than coastal areas lineer terms have more effect on the simulated tsunami waveforms, hence they are easier to fit with DART buoy records. Some waveform fits at tide gauges may be poor since high quality bathymetry (resolution of 100 m or less) is needed in order to reflect the complexity of the shallow areas (Rabinovich, 2009).

When a tsunami occurs in the open ocean, they cover a wide range of area. Because of this it is important for tsunami simulation codes to efficiently solve tsunami evolution for different depths and underwater structures. Considering this, in COMCOT, a dynamically coupled to multiple levels two-way nested grid system with different computational resolution is integrated (Wang, 2009).

2.3.2 Governing equations

The difference between tsunami wavelength and depth is high, so effects of dispersion doesnt have a considerable impact on results. Numerical tsunami simulations using shallow water equations are adequate in simulating tsunamis that propagate throughout ocean since the ratio between wavelength and depth is too high. In COMCOT, the conservative form of shallow water equations is implemented to simulate the propagation and runup processes of tsunami. In the conservative form, the governing equations are formulated in terms of free surface fluctuation and volume fluxes .

Linear shallow water equations are usually applied to describe the tsunami evolutions in open ocean, which in Spherical Coordinates have the form of,

$$\frac{\partial \eta}{\partial t} + \frac{1}{R\cos\varphi}\left\{\frac{\partial P}{\partial \psi} + \frac{\partial}{\partial \varphi}(cos\varphi)\right\} = -\frac{\partial h}{\partial t} \qquad (2.11)$$

$$\frac{\partial P}{\partial t} + \frac{gh}{R\cos\varphi}\frac{\partial \eta}{\partial \psi} - fQ = 0 \qquad (2.12)$$

$$\frac{\partial Q}{\partial t} + \frac{gh}{R\cos\varphi}\frac{\partial \eta}{\partial \varphi} + fP = 0 \qquad (2.13)$$

where η stands for the water surface fluctuation; (P, Q) indicate the volume flux components in x (East) and y (North) directions, respectively; (φ,ψ) represent the latitude and longitude of the Earth; R shows the Earth radius; g is the gravitational acceleration and h indicates water depth. $-\partial h/\partial t$, reflecting the effect of bathymetry variation, can be used to simulate tsunami waves generated by transient seafloor motions such as slow rupture processes or submarine landslides. f represents the Coriolis force coefficient due to the rotation of the Earth and

$$f = \Omega \sin\varphi \qquad (2.14)$$

where Ω represents the rotation rate of the Earth (Wang, 2009).

In COMCOT, non-linear shallow water equations are employed in Spherical Coordinates as,

$$\frac{\partial \eta}{\partial t} + \frac{1}{R\cos\varphi}\left\{\frac{\partial P}{\partial \psi} + \frac{\partial}{\partial \varphi}(cos\varphi)\right\} = -\frac{\partial h}{\partial t} \qquad (2.15)$$

$$\frac{\partial P}{\partial t} + \frac{1}{R\,cos\,\varphi}\frac{\partial}{\partial \psi}\left\{\frac{P^2}{H}\right\} + \frac{1}{R}\frac{\partial}{\partial \varphi}\left\{\frac{PQ}{H}\right\} + \frac{gH}{Rcos\varphi}\frac{\partial \eta}{\partial \psi} - fQ + F_x = 0 \qquad (2.16)$$

$$\frac{\partial Q}{\partial t} + \frac{1}{R\,cos\,\varphi}\frac{\partial}{\partial \psi}\left\{\frac{PQ}{H}\right\} + \frac{1}{R}\frac{\partial}{\partial \varphi}\left\{\frac{Q^2}{H}\right\} + \frac{gH}{R}\frac{\partial \eta}{\partial \varphi} + fP + F_y = 0 \qquad (2.17)$$

H: water depth and H = η + h; Fx and Fy is the the bottom friction in x and y directions, respectively. These two terms are calculated using Manning's Formula,

$$F_x = \frac{gn^2}{H^{\frac{7}{3}}} P(P^2 + Q^2)^{1/2} \tag{2.18}$$

$$F_y = \frac{gn^2}{H^{\frac{7}{3}}} Q(P^2 + Q^2)^{1/2} \tag{2.19}$$

where n is the Manning's roughness coefficient, which may vary in space too (Wang, 2009).

2.3.3 Numerical method

COMCOT algorithm uses an explicit staggered leap-frog finite difference scheme to solve shallow water equations in spherical coordinates (Cho, 1995). P and Q, are evaluated at the centers of the cells at boundaries (Figure 2.8).

In spherical coordinates, via Taylor expansion at the cell center ($i\Delta x$, $j\Delta y$) where η is evaluated and at time level $n\Delta t$ when P and Q are evaluated, the explicit leap-frog finite difference scheme for linear shallow water equations, with truncation errors neglected, is expressed as,

$$\frac{\eta_{i,j}^{n+1/2} - \eta_{i,j}^{n-\frac{1}{2}}}{\Delta t} + \left\{\frac{1}{R\cos\varphi}\right\}_{i,j} \frac{P_{i+1/2,j}^{n} + P_{i-1/2,j}^{n}}{\Delta\psi} + \left\{\frac{1}{R\cos\varphi}\right\}_{i,j} \tag{2.20}$$

$$\frac{\left(\cos\varphi_{i,j+1/2}\right) Q_{i,j+1/2}^{n} - \left(\cos\varphi_{i,j-1/2}\right) Q_{i,j-1/2}^{n}}{\Delta\varphi} = -\frac{h_{i,j}^{n+1/2} - h_{i,j}^{n-1/2}}{\Delta t}$$

$$\frac{P_{i+1/2,j}^{n+1} - P_{i+1/2,j}^{n}}{\Delta t} + \left\{\frac{gh}{R\cos\varphi}\right\}_{i+1/2,j} \frac{\eta_{i,j}^{n+1/2} - \eta_{i,j}^{n-1/2}}{\Delta\psi} - fQ_{i+1/2,j}^{n} = 0 \tag{2.21}$$

$$\frac{Q_{i,j+1/2}^{n+1} - Q_{i,j+1/2}^{n}}{\Delta t} + \left\{\frac{gh}{R}\right\}_{i,j+1/2} \frac{\eta_{i,j+1}^{n+1/2} - \eta_{i,j}^{n-1/2}}{\Delta\varphi} + fQ_{i,j+1/2}^{n} = 0 \tag{2.22}$$

which is often used for large-scale transoceanic tsunami simulations. The numerical scheme has a truncation error in the order of O (4x2, 4y2, 4t2).

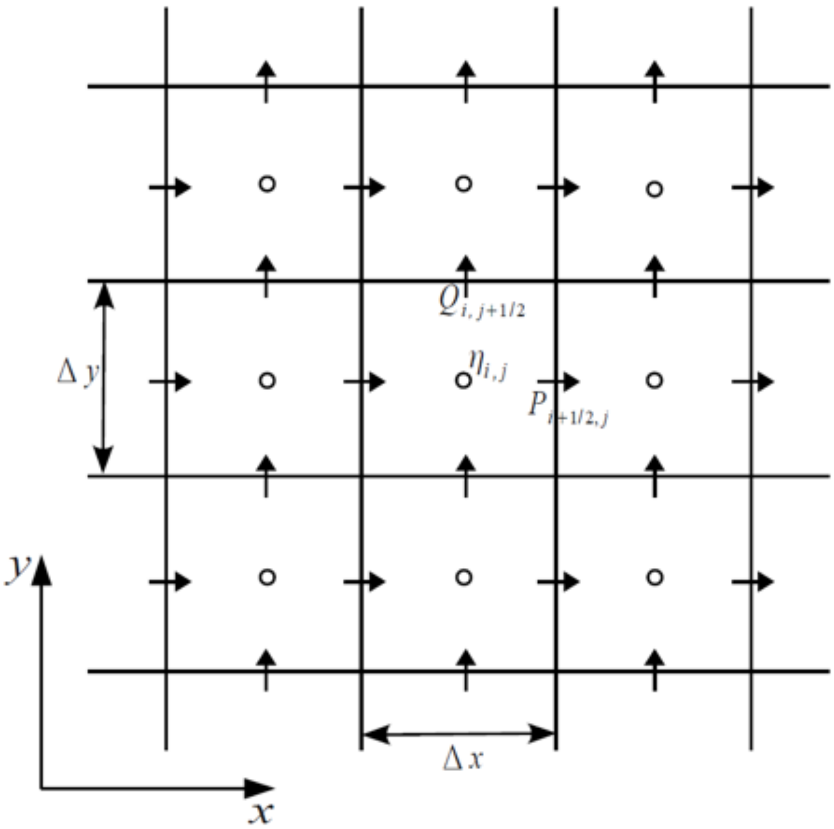

Figure 2.8 : Illustration of the grid system in which the free surface displacement is calculated using leap-frog scheme (Wang, 2009)

The Manning's formula is used to model bottom frictions. The bottom frictional terms are discretized as,

$$F_x = v_x\left(P^{n+1}_{i+1/2,j} - P^{n}_{i+1/2,j}\right) \tag{2.23}$$

$$F_y = v_y\left(Q^{n+1}_{i,j+1/2} - Q^{n}_{i,j+1/2}\right) \tag{2.24}$$

where vx and vy are given by

$$v_x = \frac{1}{2}\frac{gn^2}{\left(H^n_{i+1/2,j}\right)^{7/3}}\left[\left(P^n_{i+1/2,j}\right)^2 + \left(Q^n_{i+1/2,j}\right)^2\right]^{1/2} \tag{2.25}$$

$$v_y = \frac{1}{2}\frac{gn^2}{\left(H^n_{i,j+1/2}\right)^{7/3}}\left[\left(P^n_{i,j+1/2}\right)^2 + \left(Q^n_{i,j+1/2}\right)^2\right]^{1/2} \tag{2.26}$$

for the Manning's formula.

2.4 A Test Run for Tsunami Simulation with COMCOT Code

Initially, to confirm the validity of the COMCOT code, a test run has been conducted to compare the simulation results with a previous study. For this purpose, the September, 16 2015 Illapel (Chile) tsunami has been chosen and synthetic tsunami waves are calculated, and they are matched with the results of Yolsal-Çevikbilen et al. (2018). According to Yolsal-Çevikbilen et al. (2018), the 2015 Illapel (Chile) earthquake is occured as a result of the subduction process between Nazca and South American plates. They obtained source mechanism parameters and the slip distribution model of this earthquake using long-period and broad-band teleseismic P-waveforms. Low dipping nodal plane with strike = 350°, dip = 25°, rake = 74° have been selected as the fault plane since tectonic settings of the subduction zone in the area is more compatible with an east dipping fault. The fault plane is divided into 40 x 12 sub-faults with dimensions of 10 x 10 km^2 with the epicentre being at 26 km of depth.. Source-time function is divided into 39 elements with a rise time of 2.5 s. Faulting area is determined to be 350 x 100 km with maximum slip of 6.50 m at the NW of the fault plane (see Yolsal-Çevikbilen et al., 2018 for details).

Nested grid configuration of COMCOT is used when defining computational layers of the study area. Two nested layers with computational resolution of 2 arc-min between latitudes of -45.0° to -4.0° and longitudes of -111.5° to -69.0°, and inside 0.5 arc-min between latitudes of -35.0° to 28.0° and longitudes of -77.0° to -69.0° (Figure 2.11 and Figure 2.12). The bathymetry data used here is taken from GEBCO-30 (General Bathymetric Chart of the Oceans) ocean bathymetry data with 30 arc-seconds. For comparing real-time tsunami data with synthetic data obtained from tsunami simulation based on non-uniform finite fault slip distribution model of Yolsal-Çevikbilen et al. (2018), two DART and three tide gauges have been chosen (Table 2.1; Figure 2.13). After using this slip distribution model as an input, vertical dislocation of the ocean bottom is calculated using Okada (1985). Initial wave with a maximum value of 2.26m and with a minimum value of -1.552m is determined (Figure 2.14).

```
#=================================================:================
# Job Description: One-line brief description may be added here
 Total Simulated Duration (Wall clock, seconds) :  14400.000
 Time Interval for Snapshot Output    (seconds) :   120.0
 Zmax & Gauge Output  (0-ZMax Z;1-Gauge;2-Both) :      2
 Start Type (0-Cold start; 1-Hot start)         :      0
 Resuming Time for Hot Start          (Seconds) :  3600.00
 Minimum WaterDepth offshore           (meters) :    00.00
 Initial Cond. (0:FLT,1:File,2:WM,3:LS,4:FLT+LS):      0
 Boundary Cond.(0-Open;1-Absorb;2-Wall;3-FACTS) :      0
 Specify Filename of z Input (for BC=3, FACTS)  :23926h.asc
 Specify Filename of u Input (for BC=3, FACTS)  :23926u.asc
 Specify Filename of v Input (for BC=3, FACTS)  :23926v.asc
#
#=================================================:================
```

Figure 2.9 : Section of input file for COMCOT (comcot.ctl) which you define simulation parameters (Total simulated duration, time interval for output, output format, Initial conditions, etc.).

```
#=================================================:================
# Parameters for Fault Model (Segment 01)       :Values          |
#=================================================:================
 Number of FLT Planes (use fault_multi.ctl if>1):       999
 Rupture Start Time(,Uplift Duration)  (seconds):       0.0
 Faulting Option (0:Model-C; 1:Data; 9:Model-T) :      0
 Focal Depth                             (meters):   26000.000
 Length of Fault Plane                   (meters):  350000.000
 Width of Fault Plane                    (meters):  100000.000
 Dislocation of Fault Plane              (meters):       3.86
 Strike Angle (theta)                   (degrees):     350.000
 Dip  Angle (delta)                     (degrees):      25.000
 Slip/Rake Angle (lamda)                (degrees):      80.000
 Origin of Numerical Domain: Latitude   (degrees):     -46.0
 Origin of Numerical Domain: Longitude  (degrees):    -112.0
 Epicenter Location: Latitude           (degrees):     -31.5730
 Epicenter Location: Longitude          (degrees):     -71.6740
 File Name of Input Data                         :finite_fault.txt
 Data Format (0-COMCOT;1-MOST;2-XYZ;3-ASC)       :       2
#
#=================================================:================
```

Figure 2.10 : Section of input file for COMCOT (comcot.ctl) which you define fault parameters for the simulated earthquake induced tsunami.

```
#===============================================:================
# Parameters for 1st-level grids -- layer 01    :Values         |
#===============================================:================
 Run This Layer ?       (0:Yes,       1:No     ):       0
 Coordinate System    (0-Spherical, 1-Cartesian) :       0
 Governing Equations (0-linear,    1-nonlinear) :       0
 Grid Size        (dx, sph:minutes, Cart:meters) :       2
 Time Step Size                      (seconds) :       1.0
 Bottom Friction Switch (0-ON;1-OFF;2-ON,Var.n) :       0
 Manning's n (for Fric.Switch=0), {land, water} :       0.025
 Output Option?   (0-Z+Hu+Hv; 1-Z Only; 2-NONE) :       0
 X_start                                        :    -111.5
 X_end                                          :     -69.0
 Y_Start                                        :     -45.0
 Y_end                                          :      -4.0
 File Name of Bathymetry Data                   :  ascigrid.asc
 Format  (0-OLD;1-MOST;2-XYZ BP;3-XYZ BN;4-ASC) :       4
 Grid Identification Number (ID)                :      01
 Grid Level                                     :       1
 Parent Grid Layer's ID Number                  :       0
#
#===============================================:================
#  Parameters for Sub-level grid -- layer 02    :Values         |
#===============================================:================
 Run This Layer ?       (0:Yes,       1:No     ):       0
 Coordinate System    (0:spherical, 1:cartesian) :       0
 Governing Equations (0:linear,    1:nonlinear) :       1
 Bottom Friction Switch (0-ON,1-OFF,2:ON,Var.n) :       0
 Manning's n (for Fric.Switch=0), {land, water} :       0.025
 Output Option? (0-Z+Hu+Hv; 1-Z Only; 2-NONE)   :       0
 GridSize Ratio of Parent Grid to Current Grid  :       4
 X_start                                        :    -77.00
 X_end                                          :    -69.00
 Y_Start                                        :    -35.00
 Y_end                                          :    -28.00
 File Name of Bathymetry Data                   :  ascigrid.asc
 Format (0-OLD;1-MOST;2-XYZ BP;3-XYZ BN;4-ASC)  :       4
 Grid Identification Number (ID)                :      02
 Grid Level                                     :      2
 Parent Grid Layer's ID Number                  :      01
#
#===============================================:================
```

Figure 2.11 : Computational layer parameters for tsunami simulation. Defined bathymetry file with xyz format can be seen with the boundary coordinates.

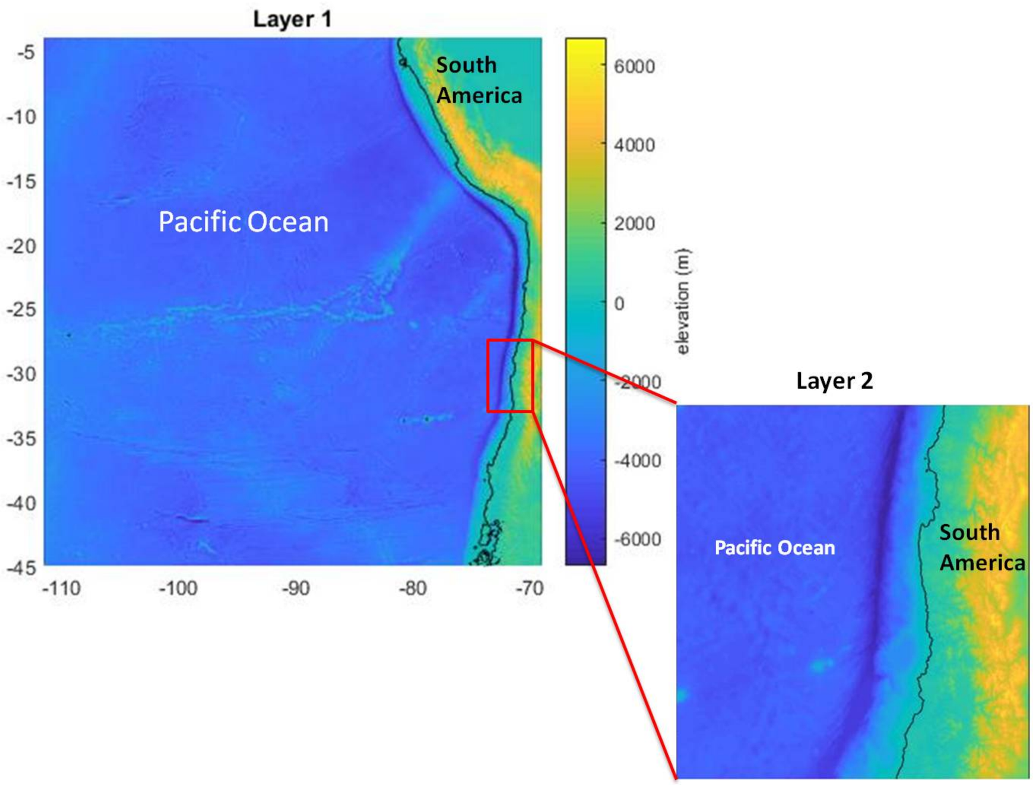

Figure 2.12 : Computational layers used for simulations of the 2015 Illapel tsunami.

Table 2.1 : Location of DART buoys and tide gauges used for comparing real data with calculated data for 2015 Illapel tsunami.

Name	Latitude	Longtitude
DART 32401	20.474	-73.421
DART 32402	26.743	-73.983
Huasco	28.460	-71.223
Juan Fernandez	33.636	-78.830
Talcahuano	36.683	-73.100

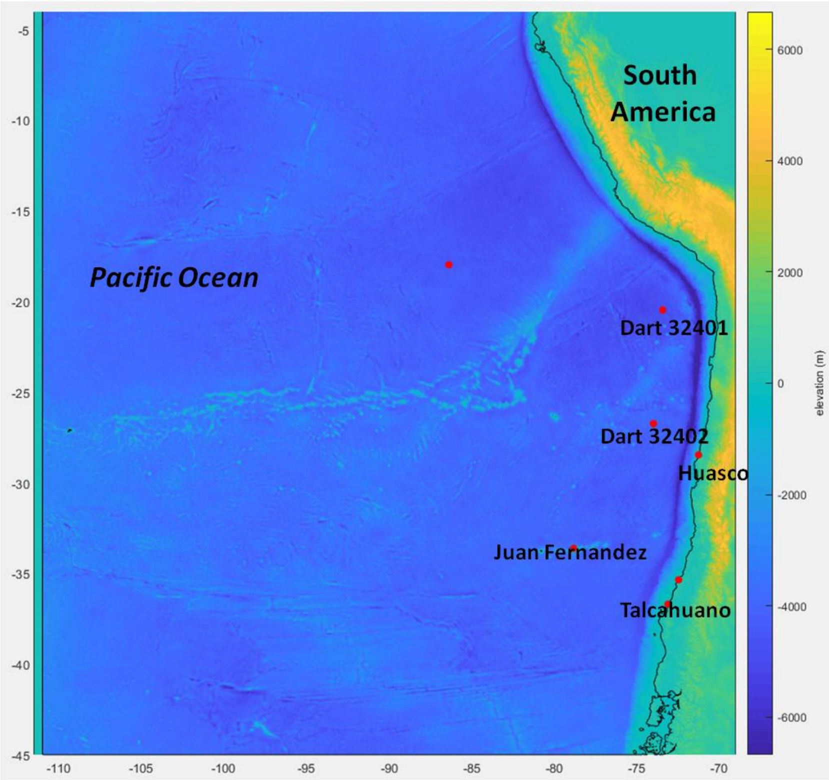

Figure 2.13 : Location of tide gauges and DARTs used in tsunami simulations of 2015 Illapel – Chile earthquake.

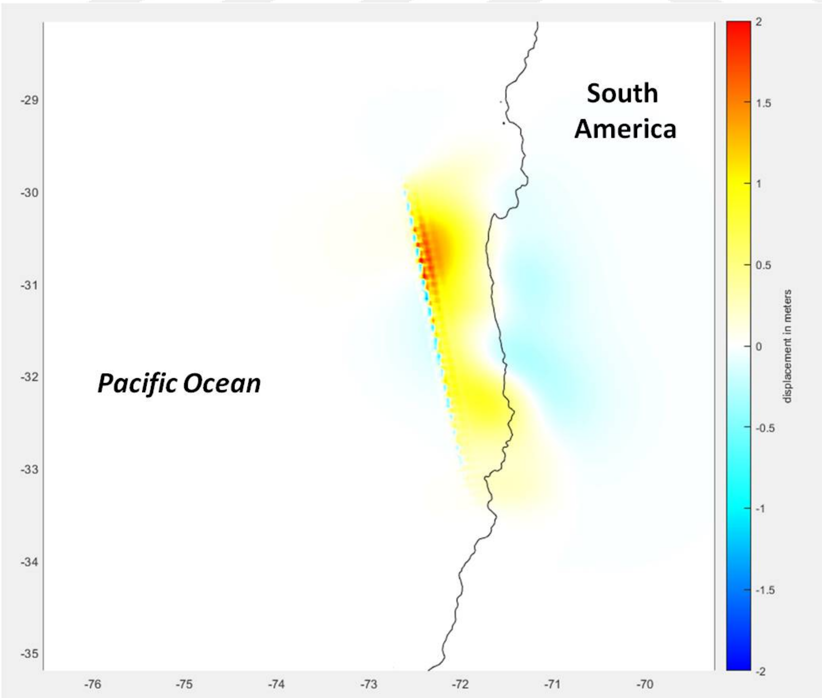

Figure 2.14 : Initial tsunami wave of the 2015 Illapel earthquake. Maximum value of 2.26 m and minimum value of-1.552 m is obtained.

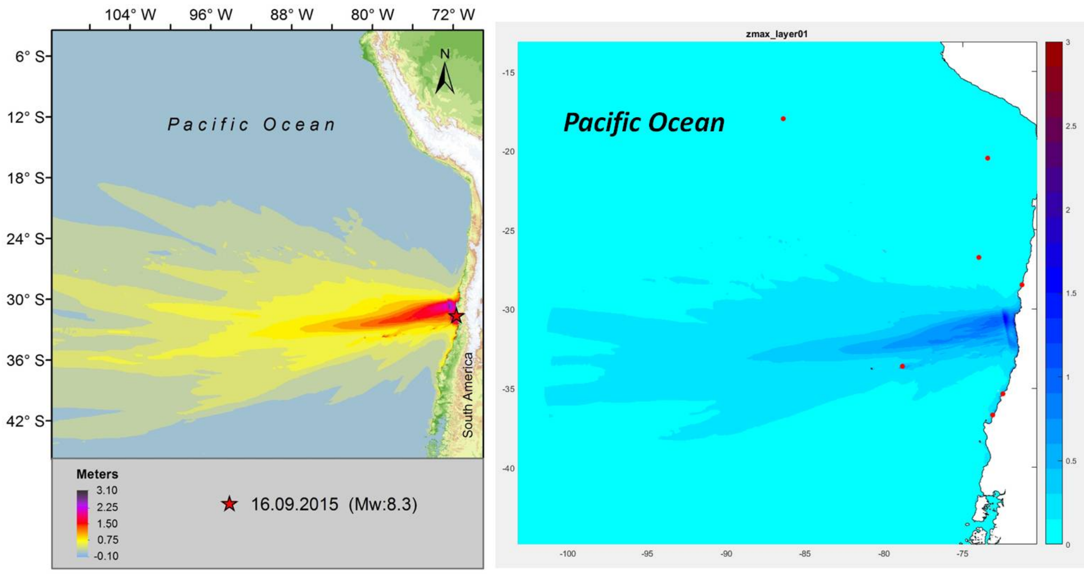

Figure 2.15 : Maximum wave heights obtained from tsunami simulation run for 4 hours (right, layer 1, 2 arc-min computational resolution) in this study. Maximum wave heights reported by Yolsal-Çevikbilen et al. (2018) is given on left for comparison.

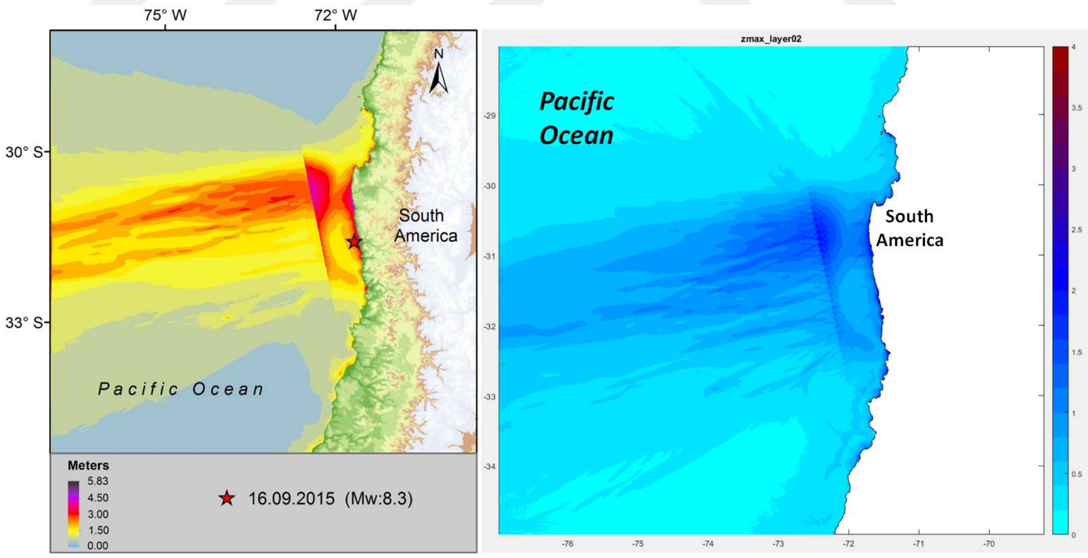

Figure 2.16 : Maximum wave heights obtained from tsunami simulation run for 4 hours (right, layer 2, 0.5 arc-min computational resolution) in this study. Maximum wave heights reported by Yolsal-Çevikbilen et al. (2018) is also given on left for comparison.

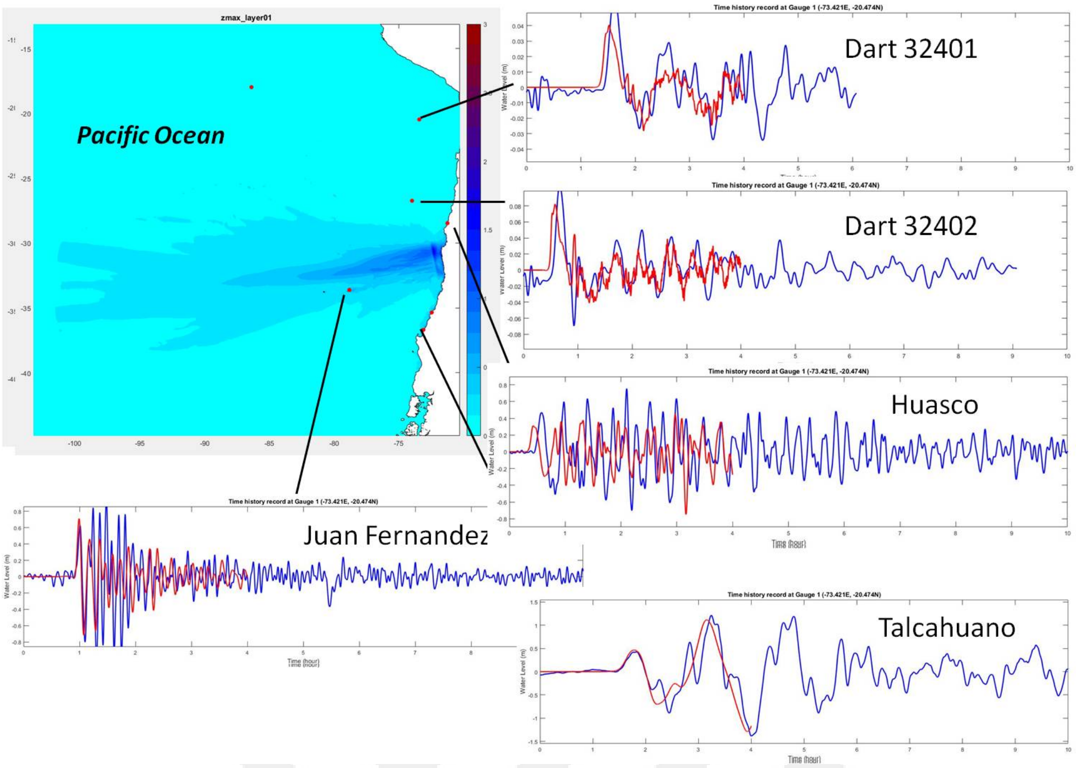

Figure 2.17 : Comparison of observed tsunami data (blue) with the calculated ones (red) by this study.

In Figures 2.15 and 2.16, maximum wave heights for Layers 1 and 2 with 2 arc-min and 0.5 arc-min resolution respectively for the first 4 hours of the tsunami can be seen. Then, the observed and synthetic tsunami waveforms are plotted for DART and tide-gauge stations for comparison in shape and arrival times of waves (Figure 2.17). The simulation results obtained by this study and Yolsal-Çevikbilen et al. (2018) seem to be consistent (Figure 2.18).

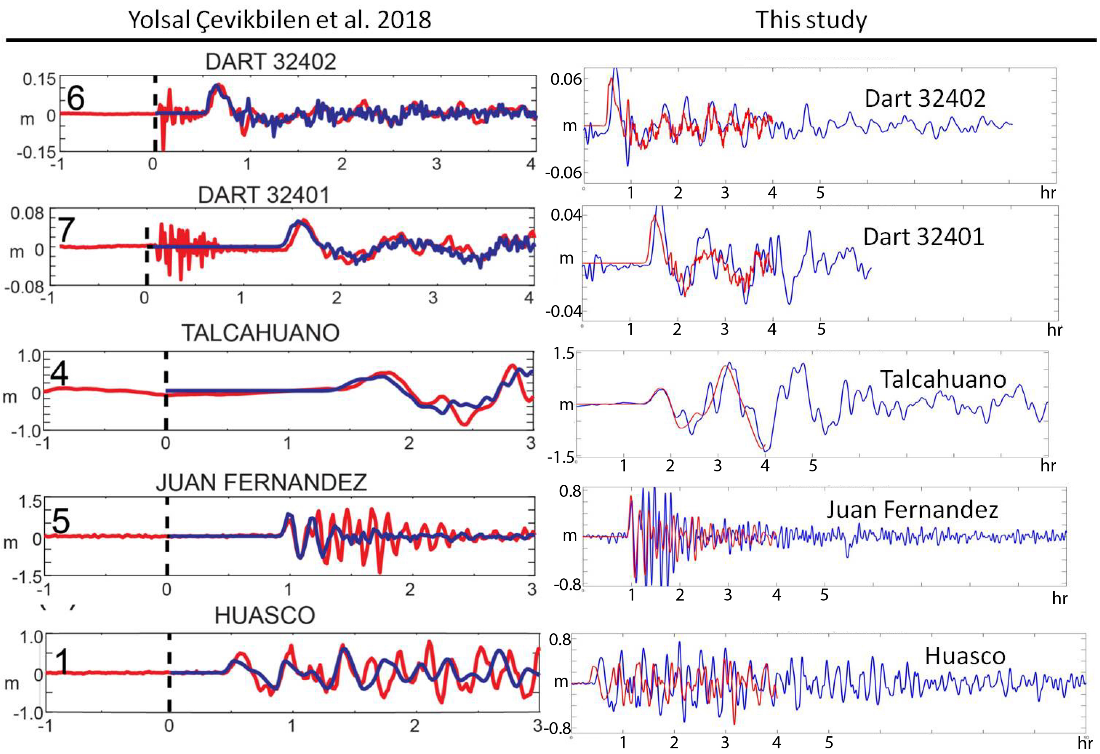

Figure 2.18 : Comparison of simulation results reported by Yolsal-Çevikbilen et al. (2018) and this study.

3. RESULTS

In this part of MSc. thesis, the overall results are summarized. Source models of two destructive earthquakes ($M_w \geq 7.0$) occurred in Peru and Mexico have been analyzed in this study. The detailed point-source parameters and finite-fault slip models are listed in Table 3.1. Then, numerical tsunami simulations which reveal tsunami wave amplitudes and arrival times of first tsunami waves at different coastal plains have also been achieved based on uniform slip models constrained by teleseismic waveform inversions. It is well-known that seismological parameters such as source mechanism parameters and slip distribution models are crucial in tsunami studies since they are used as initial parameters of numerical tsunami simulations (Fan et al., 2017; Heidarzadeh et al., 2018; Yolsal-Çevikbilen et al., 2018).

Tsunami simulations have been run for 4 hours of real-time tsunami wave propagation in open ocean. In order to adequately evaluate the simulation results, comparisons were made between the real-time observed data recorded by DART bouys (NDBC, 2015) and shore-based tide gauges and calculated waveforms in terms of shape and wave amplitudes, and arrival times of first tsunami waves. In general, the limited number of tide-gauges and DART buoys are used in simulations possibly due to the lack of a high resolution bathymetry. By using GEBCO-BODC 30 arc-sec bathymetry data, the COMCOT code assumes most of the other available tide gauge stations inland and it could not calculate synthetic waveforms at those locations. The vertical dislocation of the ocean bottom is computed by using Okada (1985) equations, and then initial tsunami wave is modelled. Furthermore, nested layers named as Layer 1 and Layer 2 with computational resolutions of 2 arc-min and 0.5 arc-min, respectively, are chosen for simulating tsunami wave propagation.

Table 3.1 : Source mechanism parameters of 2013 Acari-Peru (M_w 7.1) and 2017 Chiapas-Mexico (M_w 8.2) earthquakes obtained by this study. Epicenter coordinates and origin times (*) are taken from the USGS-NEIC earthquake catalogue. Earthquake source parameters (**) obtained from point source double-couple inversions are used as input in the finite-fault slip inversions.

	The September 25, 2013 Acari-Peru earthquake		The September 08, 2017 Chiapas-Mexico earthquake	
	Point-Source Double-Couple	Finite-Fault Slip Model	Point-Source Double-Couple	Finite-Fault Slip Model
Latitude (N°)	-15.839*	-15.839*	15.022*	-15.839*
Longitude (W°)	7 .511*	74.511*	93.899*	74.511*
Origin time (h:m:s)	16:42:43*	16:42:43*	04:49:19*	04:49:19*
Focal depth (km)	48	48	54	54
Strike (ϕ, °)	322	322**	311	311**
Dip (δ, °)	27	27**	82	82**
Rake (λ, °)	89	90.4	-105	-85.9
Fault Length(L, km)	---	48	---	120
Fault Width (W, km)	---	32	---	50
Average slip (m) Maximum slip (m)	---	0.67 1.5	---	5.2 22.1
$M_o \times 10^{19}$ (Nm)	4.705	4.712	221	229
M_w	7.1	7.1	8.2	8.2

3.1 25 September 2013 Acari-Peru Earthquake (M_w 7.1)

The September 25, 2013 Acari-Peru earthquake (M_w 7.1) has occurred along the Peru-Chile trench at 16:42:43 UTC (USGS-NEIC) (see Table 3.1; Figure 1.4). In this study, teleseismic 36 long-period (LP) P-waveforms and 5 LP SH-waveforms showing a good azimuthal distribution have been inverted in order to obtain focal mechanism solution of this earthquake. Inversion results indicate a NW-SE trending reverse faulting mechanism (strike/dip/rake angles: 322°/27°/89°) at shallow focal depth of 48 km. Seismic moment of this earthquake is also obtained as 4.705×10^{19} Nm (Table 3.1). Moment magnitude (M_w) is calculated to be 7.1 for this event using the equation of Kanamori and Anderson (1975). Source time function, shown below the P- wave focal sphere (Figure 3.1), exhibits source length about 35 sec.

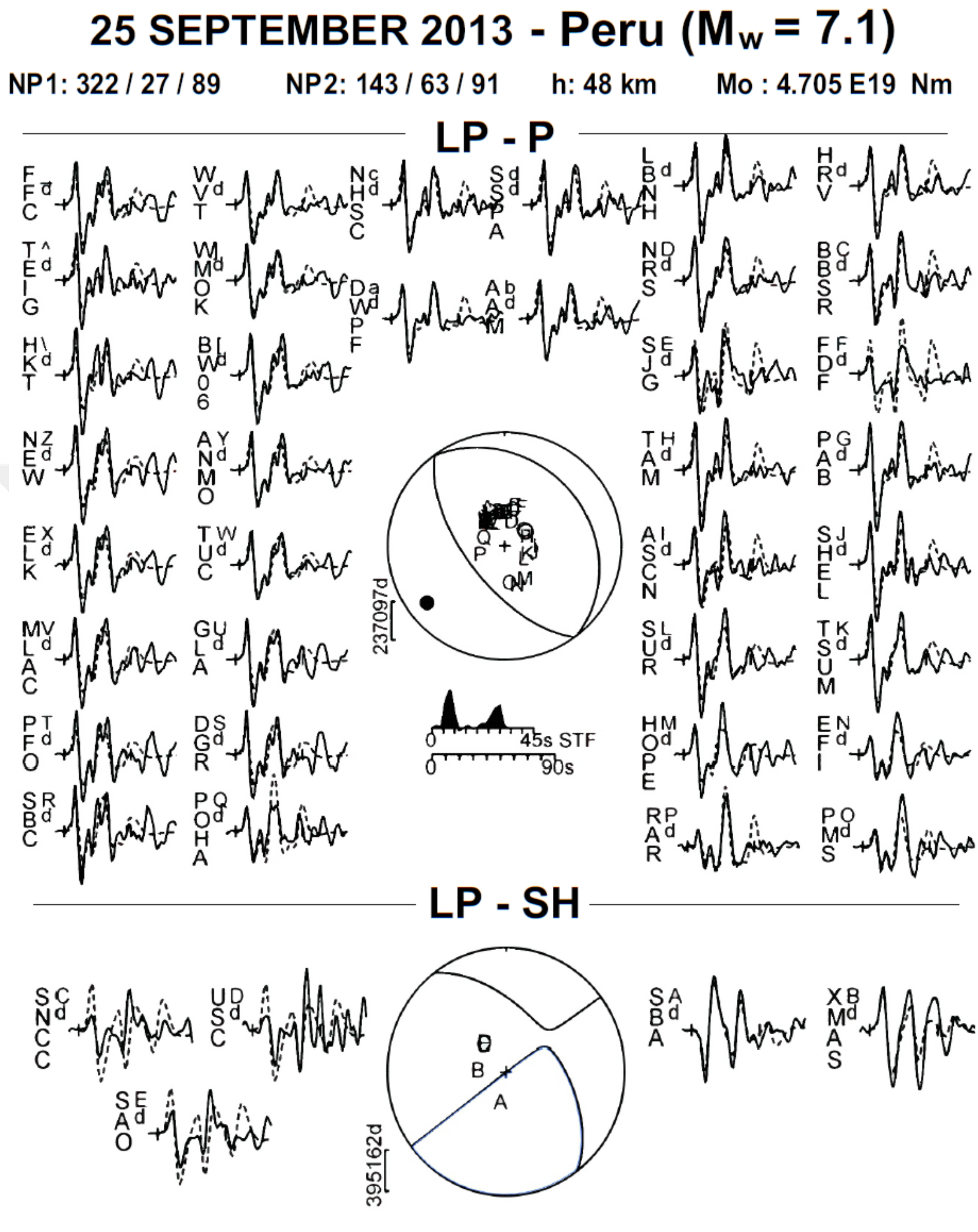

Figure 3.1 : Minimum misfit solution of 2013 Acari (Peru) earthquake obtained by using teleseismic long period 34 P- and 5 SH-waveforms. Strike, dip and rake angles of nodal planes, focal depth and seismic moment of this earthquake is given on header. The source time function (STF) is also given in the middle of figure, and beneath it is shown the time scale used for the waveforms. Focal spheres are shown with P (top) and SH (bottom) nodal planes in lower hemisphere projections. P- and T- axes are marked by solid and open circles, respectively.

The azimuthal distribution of P-wave first motion polarities recorded by seismic teleseismic and near-field stations is also checked. The P-wave first motion polarities are in a good agreement with the focal mechanism solution obtained by waveform inversion. Near-field seismic stations (i.e., PEL, LCO, SMAL, LPAZ etc.) are particularly important for constraining the nodal planes. For example, the downward P- wave first motion polarity at the PEL (Δ=17.58°) seismic station, which is located at the dilatational lobe of the focal sphere, better constrained the nodal plane (see Figure 3.2).

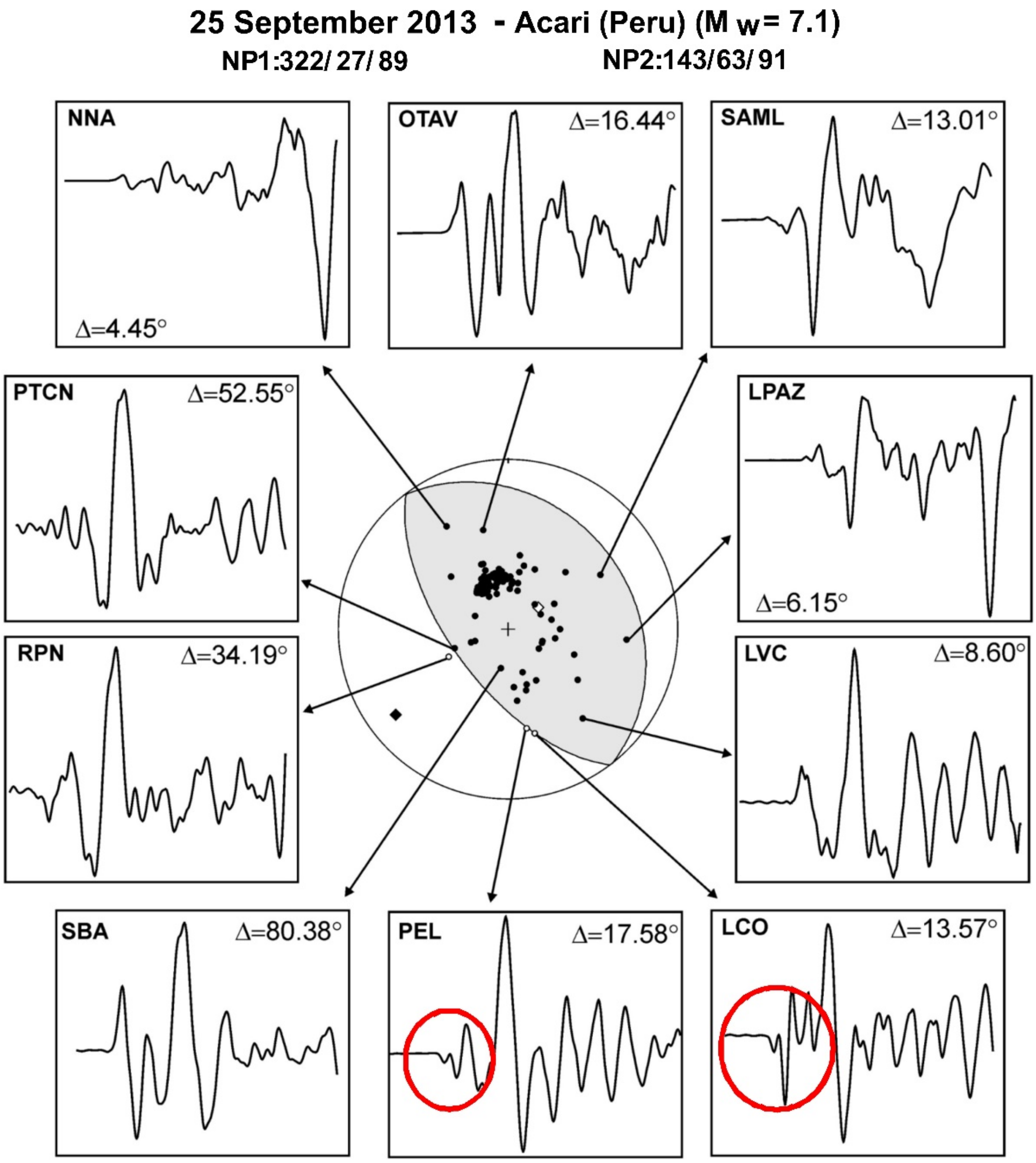

Figure 3.2 : Distributions of P- wave first motion polarities recorded at near-field and teleseismic seismic stations. Up and down polarities are shown with black and open circles, respectively.

In addition, several moment tensor catalogues such as USGS and Harvard-CMT reported a thrust faulting mechanism for this earthquake, and it is seen that source mechnanism parameters are quite similar with the ones obtained by this study (Figure 3.3). When general tectonic settings are considered, the nodal plane with lower dip angle (NP1, δ=27°) is chosen as the fault plane.

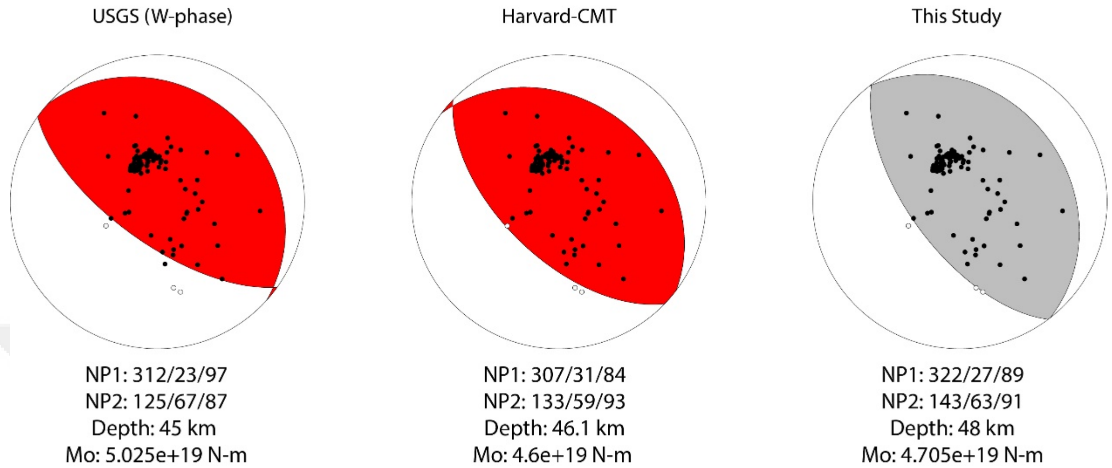

Figure 3.3 : Focal mechanism solutions reported by USGS (left), Harvard-CMT (middle) and this study (right).

For the finite-fault slip distribution modeling, 59 broad-band (BB) P-waveforms are inverted (Figures 3.4 and 3.5). In inversion, the NW-SE trending nodal plane with a dip angle of 27° is selected as the fault plane of this earthquake considering the general tectonic characteristics of the study region. The fault plane is divided into 12 x 8 sub-faults with 4 km x 4 km grid sizes. To set a source time function, 19 overlapping triangle functions each with a rise time (τ) of 2 s are used. For determining the final slip distribution model, 17 various runs have been conducted and the one with best-fitting data and minimum variance value is chosen as the final slip model. It shows a relatively simple slip distribution on the fault plane. Similar to the results of teleseismic P- and SH- waveform inversion, the source duration is found as about 38 sec (see Figure 3.1 and Figure 3.4). There is no finite-fault slip distribution model reported by USGS-NEIC for this earthquake.

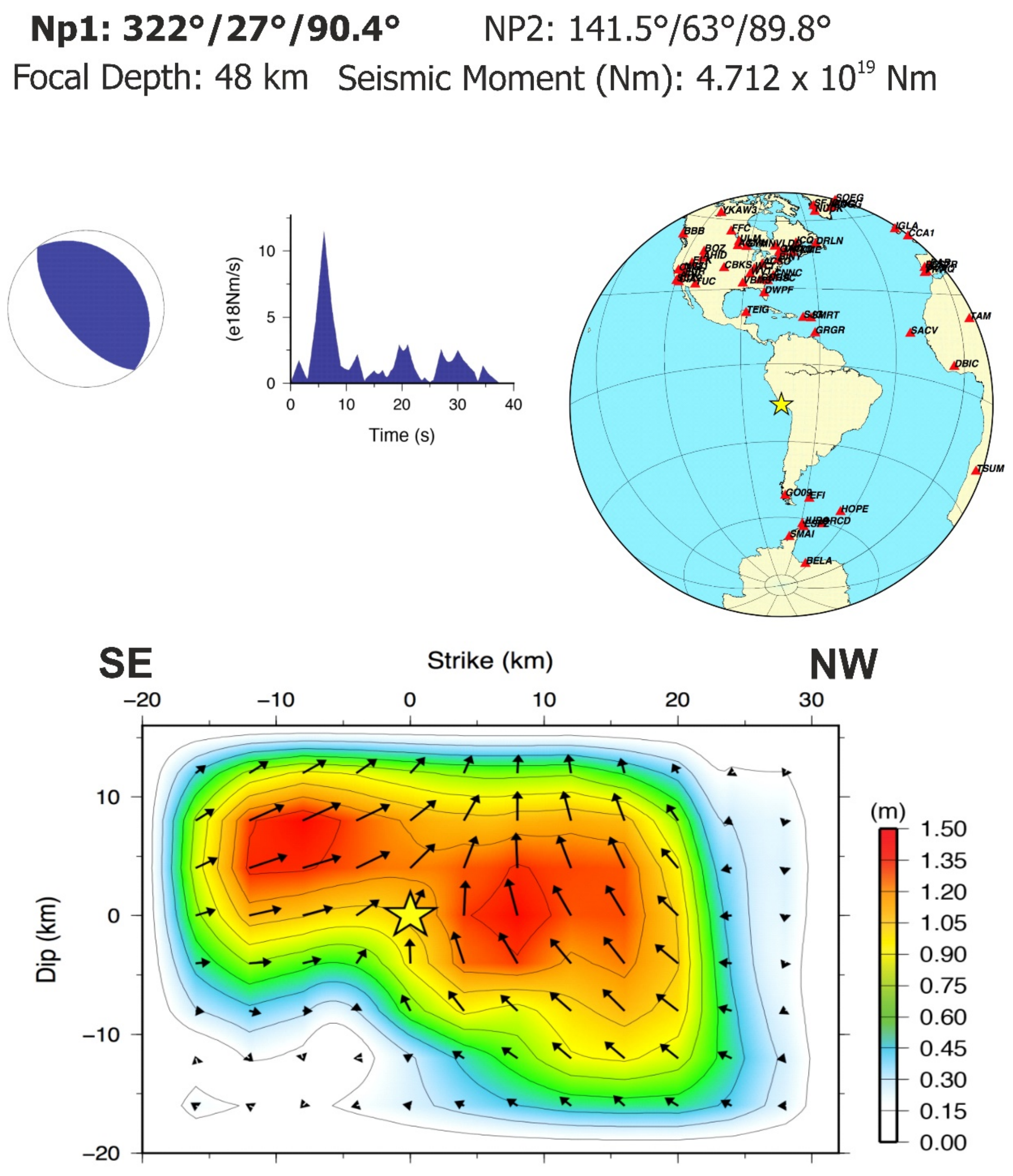

Figure 3.4 : Finite-fault slip distribution model of the September 25, 2013 Peru earthquake determined from hybrid back-projection slip inversion. Focal mechanism, source time function and teleseismic station distribution are also provided.

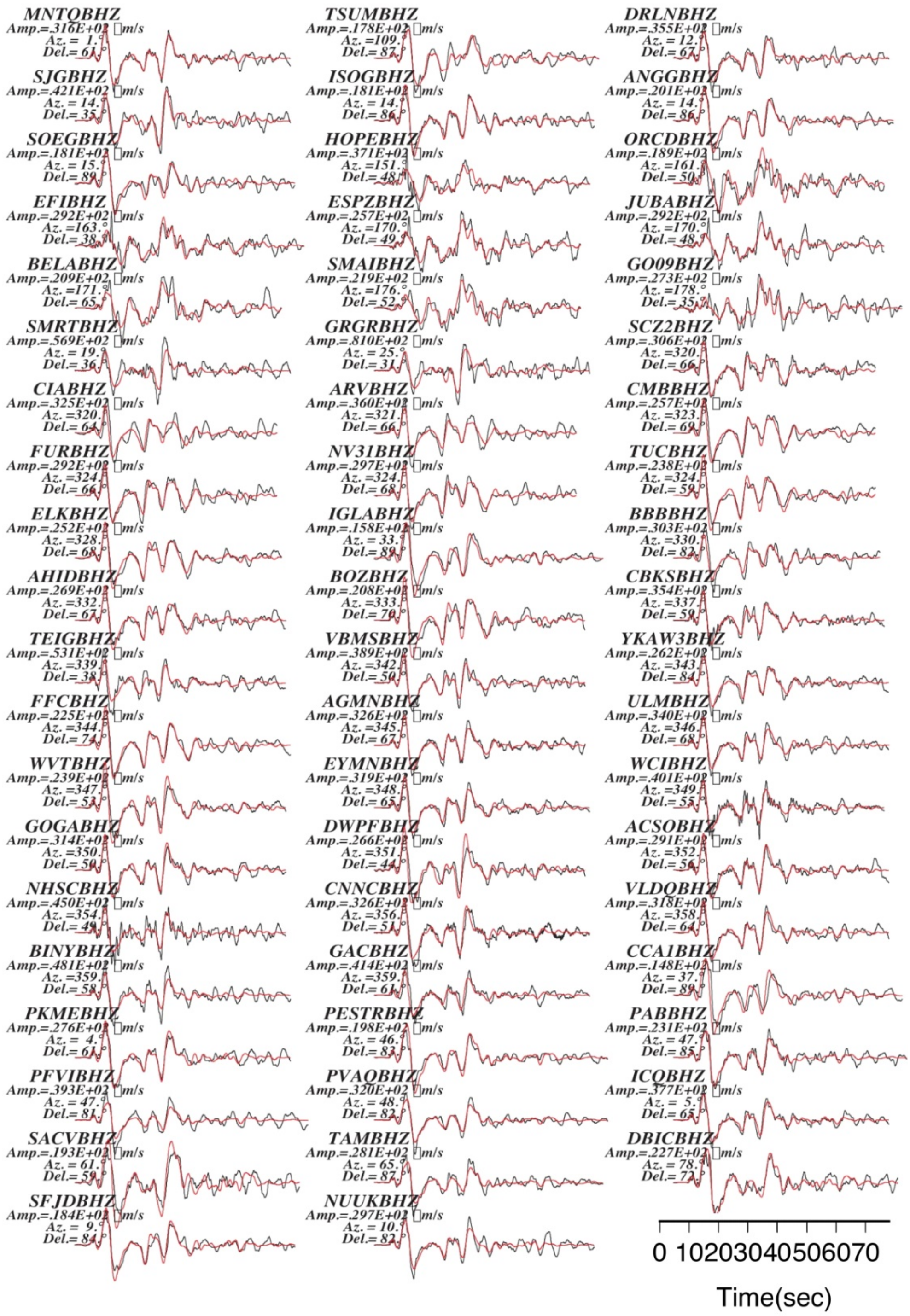

Figure 3.5 : Comparison of teleseismic 59 observed broad-band (BB) P-waveforms (black) and synthetic waveforms (red).

The maximum displacement occurred on the NW and SE side of the fault plane was found to be 1.50 m. Dimensions of the fault plane are found as approximately 40 km for the fault length and 30 km for the fault width (Figure 3.4). These values are consistent with the empirical equations of Wells and Coppersmith (1994). The study of Wells and Coppersmith (1994) analyzed 421 historical earthquakes to find empirical relations between moment magnitude (M_w), subsurface rupture length (SRL), downdip rupture width (RW), rupture area (RA) and maximum and average displacement (MD, MA). According to these equations; the empirical Fault Length = 38.24 km, the Fault Width = 21.78 km, the Fault Area = 833.05 $km^{2,}$ and Maximum Displacement = 1.60 km for this event with the seismic moment of 4.705 x 10^{19} Nm. The stress drop of this earthquake have been calculated as about $\Delta\sigma$ = 20 bars. Kanamori and Anderson (1975) reported that intraplate earthquakes have a large stress drop (~ 100bar), while interplate earthquakes have a smaller stress drop (~ 30bar) values. Hence, this event can be called as interplate earthquake.

Numerical tsunami simulation of 2013 Acari (Peru) earthquake based on uniform slip model is also conducted to calculate synthetic tsunami waveforms. In simulation, source mechanism parameters (strike (φ)=322°, dip (δ)=27°, rake (λ) =89°, and focal depth = 26 km) are used as input parameters. The fault length (L= 48 km) and fault width (W= 32 km) estimated from the finite-fault slip model of this earthquake are another input data for simulations (Figure 3.4). Those input parameters for the COMCOT code is given in Figures 3.7 - 3.8 - 3.9. As a result, it is observed that this event did not create significant tsunami waves (see Figures 3.6 and 3.10) since it has rather small average (D_{av}: 0.95 m) and maximum displacement (D_{max}: 1.50 m) values consistent with the real-time tsunami observations recorded by DART buoys and two tide gauges (Table 3.2). Maximum wave heights calculated for 4 hr simulation time indicate the maximum wave height of 0.20 m (Figure 3.10). It is seen that the amplitudes of calculated tsunami waves are quite low (~20 cm), and hence, by using the low resolution batimetry data in tsunami simulations it is not possible to calculate detailed synthetic tsunami waves. Therefore, the discrepancy between the simulated waves and the real-time data recorded by DART 32401 and tide gauges of Matarina and Taltal is quite high (Figure 3.6).

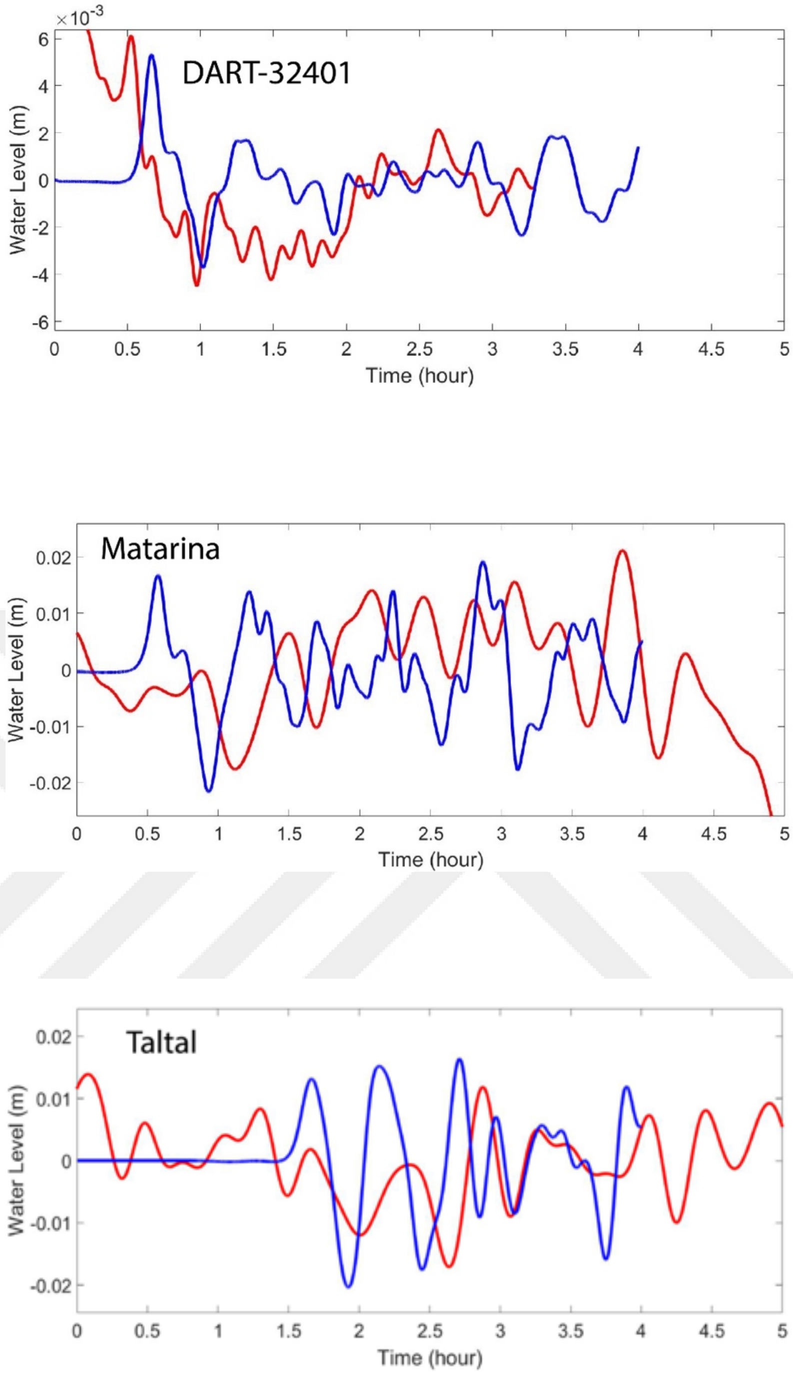

Figure 3.6 : Comparison of the real-time tsunami data (red) recorded by DART buoys and tide gauges with the calculated waveforms (blue).

```
#================================================:================
# General Parameters for Simulation              : Value Field    |
#================================================:================
# Job Description: One-line brief description may be added here
 Total Simulated Duration (Wall clock, seconds) :  14400.000
 Time Interval for Snapshot Output    (seconds) :   120.0
 Zmax & Gauge Output  (0-ZMax Z;1-Gauge;2-Both) :     2
 Start Type (0-Cold start; 1-Hot start)         :     0
 Resuming Time for Hot Start          (Seconds) :  3600.00
 Minimum WaterDepth offshore           (meters) :    00.00
 Initial Cond. (0:FLT,1:File,2:WM,3:LS,4:FLT+LS):     0
 Boundary Cond.(0-Open;1-Absorb;2-Wall;3-FACTS) :     0
 Specify Filename of z Input (for BC=3, FACTS)  :23926h.asc
 Specify Filename of u Input (for BC=3, FACTS)  :23926u.asc
 Specify Filename of v Input (for BC=3, FACTS)  :23926v.asc
#
#================================================:================
```

Figure 3.7 : Section of input file for COMCOT (comcot.ctl) of the 2013 Acari (Peru) earthquake (Total simulated duration, time interval for output, output format, initial conditions, etc.).

```
#================================================:================
# Parameters for Fault Model (Segment 01)        :Values          |
#================================================:================
 Number of FLT Planes (use fault_multi.ctl if>1):       1
 Rupture Start Time(,Uplift Duration)  (seconds):       0.0
 Faulting Option (0:Model-C; 1:Data; 9:Model-T) :       0
 Focal Depth                             (meters):   48000.000
 Length of Fault Plane                   (meters):  48000.000
 Width of Fault Plane                    (meters):  32000.000
 Dislocation of Fault Plane              (meters):       0.95
 Strike Angle (theta)                   (degrees):     322.000
 Dip  Angle (delta)                     (degrees):      27.000
 Slip/Rake Angle (lamda)                (degrees):      89.400
 Origin of Numerical Domain: Latitude   (degrees):     -35.0
 Origin of Numerical Domain: Longitude  (degrees):     -96.0
 Epicenter Location: Latitude           (degrees):     -15.8390
 Epicenter Location: Longitude          (degrees):     -74.5110
 File Name of Input Data                         :finite_fault.txt
 Data Format (0-COMCOT;1-MOST;2-XYZ;3-ASC)      :       2
#
#================================================:================
```

Figure 3.8 : Section of input file for COMCOT (comcot.ctl) of the 2013 Acari (Peru) earthquake including the fault orientation parameters.

```
#=================================================:================
# Parameters for 1st-level grids -- layer 01    :Values          ||
#=================================================:================
 Run This Layer ?       (0:Yes,       1:No      ):       0
 Coordinate System   (0-Spherical, 1-Cartesian) :       0
 Governing Equations (0-linear,    1-nonlinear) :       0
 Grid Size       (dx, sph:minutes, Cart:meters) :       2
 Time Step Size                       (seconds) :       1.0
 Bottom Friction Switch (0-ON;1-OFF;2-ON,Var.n) :       0
 Manning's n (for Fric.Switch=0), {land, water} :       0.025
 Output Option?   (0-Z+Hu+Hv; 1-Z Only; 2-NONE) :       0
 X_start                                        :     -96.0
 X_end                                          :     -69.0
 Y_Start                                        :     -35.0
 Y_end                                          :      -9.0
 File Name of Bathymetry Data                   :  bathymetry.xyz
 Format  (0-OLD;1-MOST;2-XYZ BP;3-XYZ BN;4-ASC) :       3
 Grid Identification Number (ID)                :      01
 Grid Level                                     :       1
 Parent Grid Layer's ID Number                  :       0
#
#=================================================:================
#  Parameters for Sub-level grid -- layer 02    :Values           |
#=================================================:================
 Run This Layer ?       (0:Yes,       1:No      ):       0
 Coordinate System   (0:spherical, 1:cartesian) :       0
 Governing Equations (0:linear,    1:nonlinear) :       1
 Bottom Friction Switch (0-ON,1-OFF,2:ON,Var.n) :       0
 Manning's n (for Fric.Switch=0), {land, water} :       0.025
 Output Option? (0-Z+Hu+Hv; 1-Z Only; 2-NONE)   :       0
 GridSize Ratio of Parent Grid to Current Grid  :       4
 X_start                                        :    -78.00
 X_end                                          :    -70.00
 Y_Start                                        :    -19.00
 Y_end                                          :    -14.00
 File Name of Bathymetry Data                   :  bathymetry.xyz
 Format (0-OLD;1-MOST;2-XYZ BP;3-XYZ BN;4-ASC)  :       3
 Grid Identification Number (ID)                :      02
 Grid Level                                     :      2
 Parent Grid Layer's ID Number                  :      01
#
#=================================================:================
```

Figure 3.9 : Computational layer parameters for tsunami simulation of the 2013 Acari (Peru) earthquake. Defined bathymetry file with xyz format can be seen with the boundary coordinates.

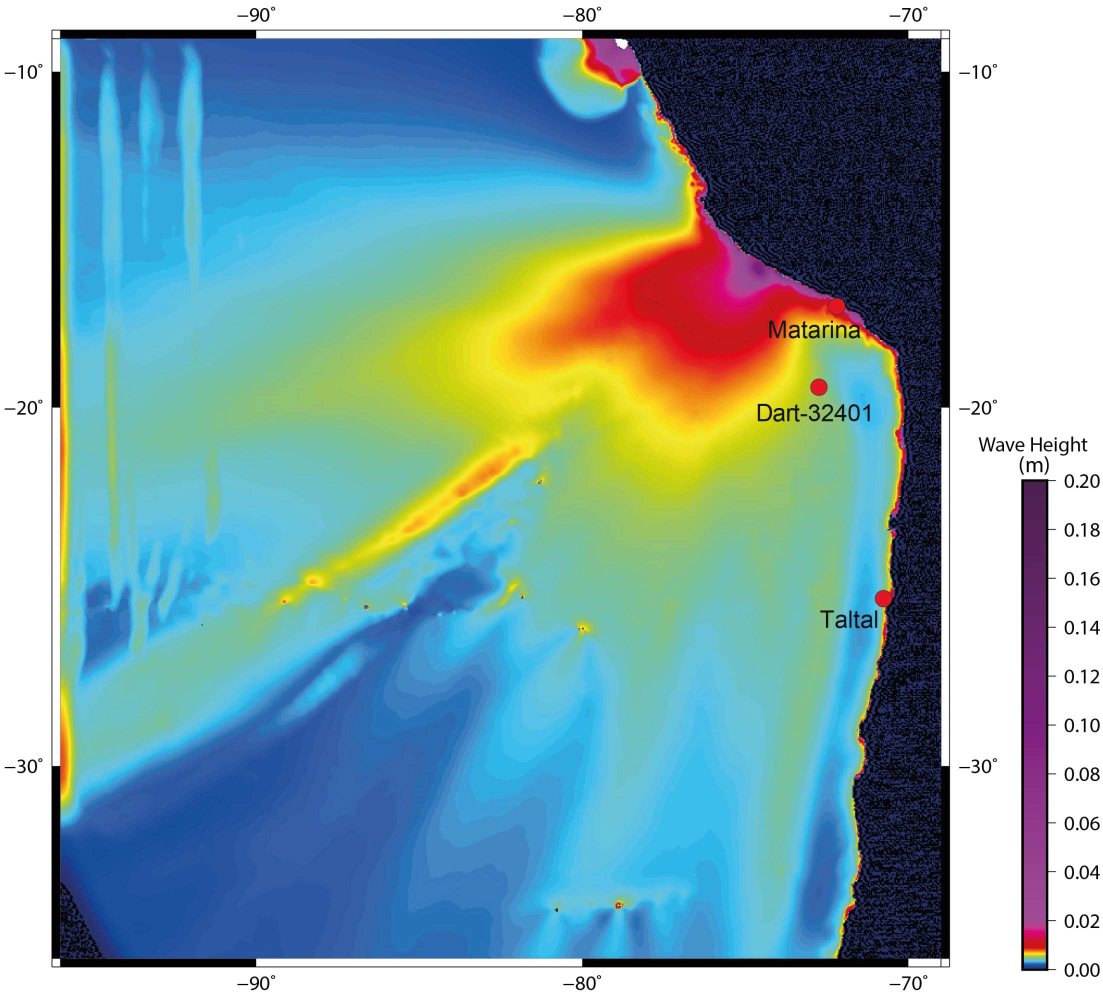

Figure 3.10 : Computed maximum tsunami wave heights for the September 25, 2013 Acari (Peru) earthquake with a computational grid of 2 arcmin. Red dots indicate the locations of the DART bouys and tide gauge station for comparing synthetic waveforms with the real data.

3.2 08 September 2017 Chiapas-Mexico Earthquake (M_w 8.2)

This destructive earthquake occurred on the September 08, 2017 at Chiapas (Mexico) along the Middle America Trench with a moment magnitude (M_w) of 8.2 (Table 3.1; Figure 1.6). Source mechanism parameters of this earthquake have been determined using 25 LP P- and 6 SH- waveforms recorded at teleseismic stations. Inversion result indicates an earthquake with normal faulting mechanism and a small amount of strike-slip component. It is also found that this event occurred in a shallow focal depth of 54 km with a seismic moment (M_o) of 2.21 x 10^{21} Nm. Source time function reveals a relatively simple rupture at focus, and the source duration of about 95 sec (Figure 3.11). P- wave first motion polarities are also consistent with the source mechanism solutions obtained by this study (Figure 3.12).

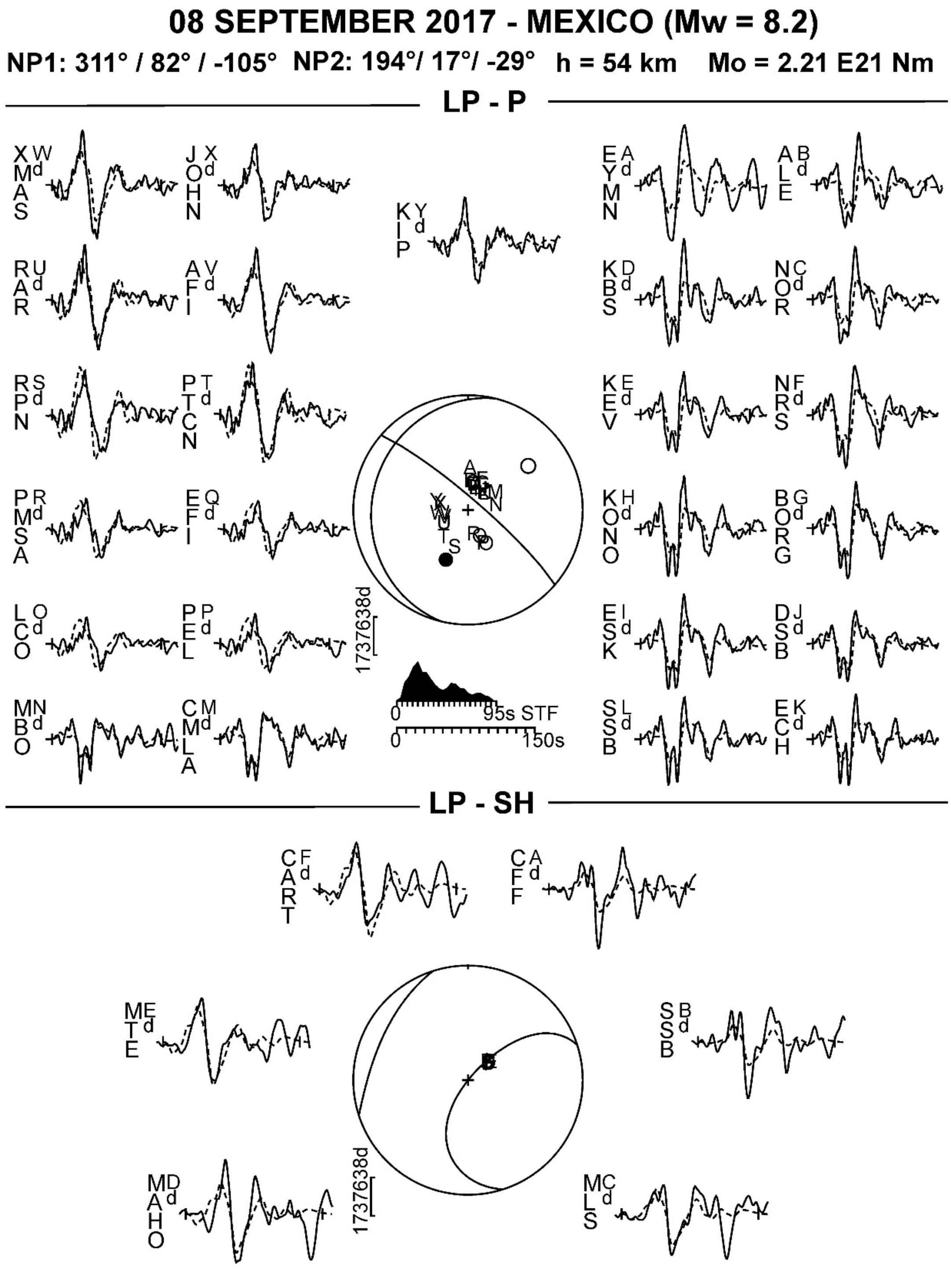

Figure 3.11 : Minimum misfit solution of the September 08, 2017 Chiapas (Mexico) earthquake (M_w 8.2) obtained by using teleseismic long period 25 P- and 6 SH-waveforms. Strike, dip and rake angles of nodal planes, focal depth and seismic moment of this earthquake is given on header. The source time function (STF) is also given in the middle of figure, and beneath it is shown the time scale used for the waveforms. Focal spheres are shown with P (top) and SH (bottom) nodal planes in lower hemisphere projections. P- and T- axes are marked by solid and open circles, respectively.

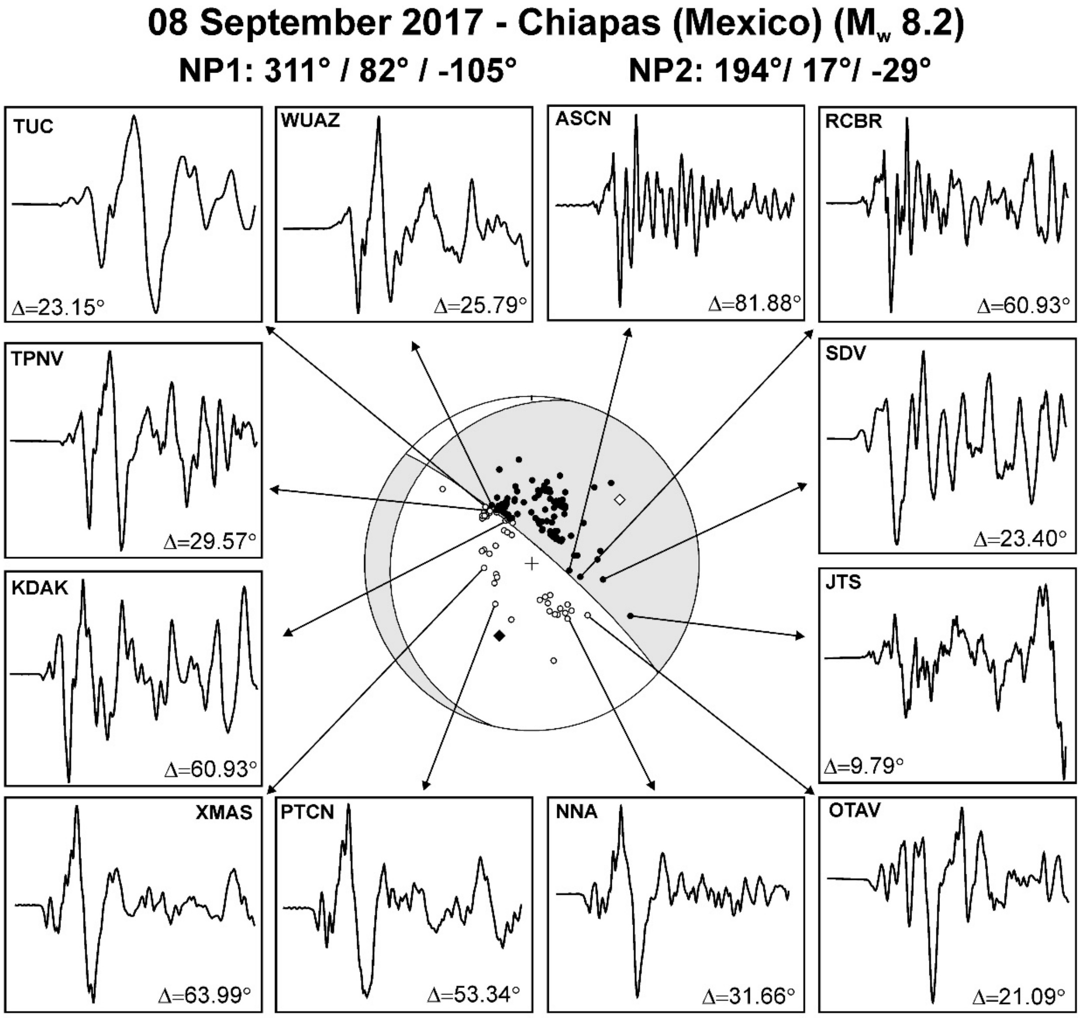

Figure 3.12 : Distributions of P- wave first motion polarities recorded at near-field and teleseismic seismic stations. Up and down polarities are shown with black and open circles, respectively.

Furthermore, there are several source models reported by different seismological studies for this destructive earthquake (i.e., Ramirez-Herrera et al., 2017; Adriano et al., 2017; Ye et al., 2017). From Figure 3.13, it is seen that source mechanism solution of this earthquake, obtained by this thesis, is more consistent with the P-wave first motion polarities than source mechanisms reported by other studies.

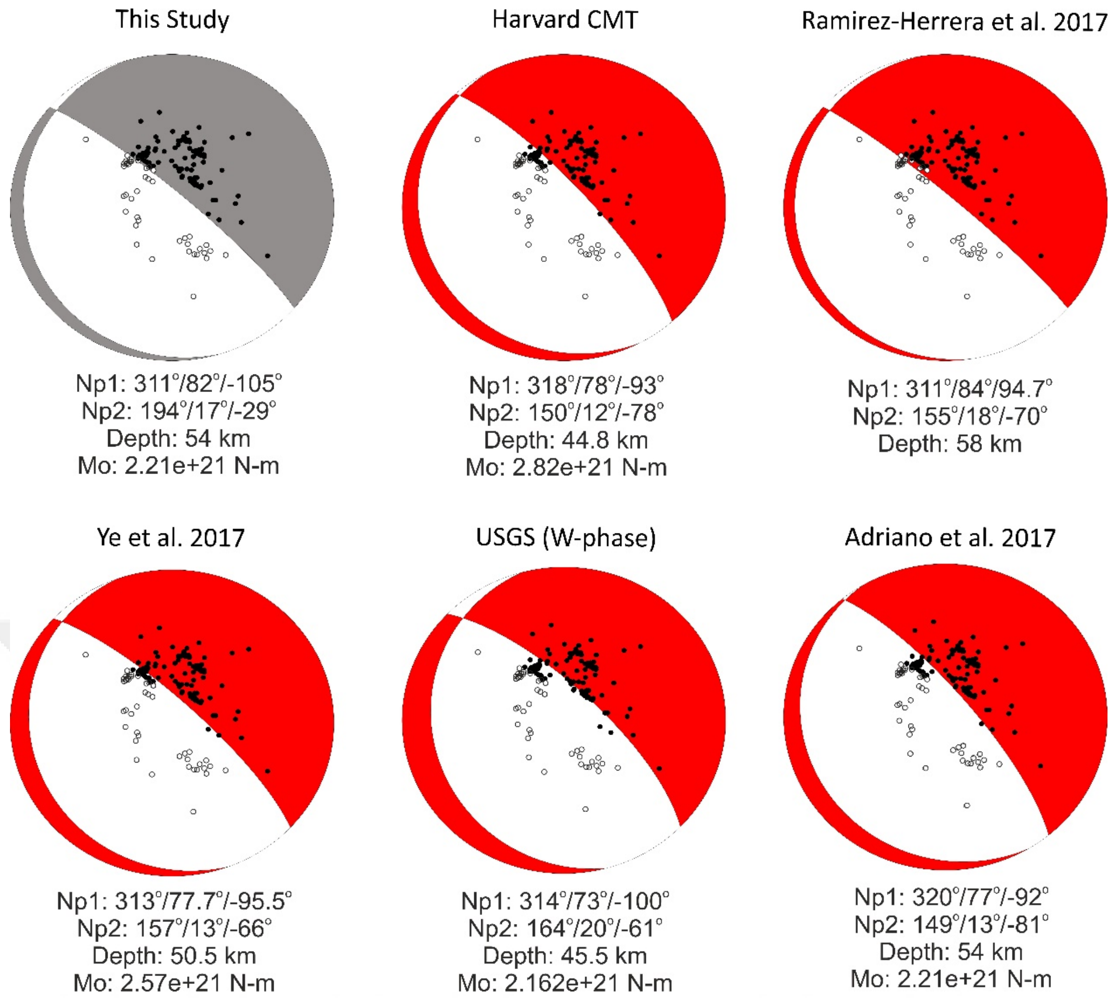

Figure 3.13 : Distributions of P- wave first motion polarities recorded at near-field and teleseismic seismic stations on focal mechanism solutions reported by different institutions (i.e., Harvard-CMT, USGS) and seismological studies (i.e., Adriano et al., 2017; Ye et al., 2017; Ramirez-Herrera et al., 2017).

For the finite-fault slip distribution modeling, 49 broad-band (BB) P-waveforms are inverted (Figures 3.14 and 3.15). In inversion, the NW-SE trending nodal plane with a dip angle of 82° is selected as the fault plane of this earthquake considering the general tectonic characteristics of the study region. The fault plane is divided into 24 x 10 sub-faults with 5 km x 5 km grid sizes. 15 overlapping triangle functions each with a rise time (τ) of 2 s. are used to calculate source time function of the earthquake. For this event, in order to estimate the slip distribution model, 14 various runs have been conducted and the one with best-fitting data and minimum variance value is chosen as the final model. Slip models shows a relatively simple slip distribution on the fault plane. Similar to the results of teleseismic P- and SH-waveform inversion, the source duration is found as about 35 sec (see Figure 3.14).

The maximum displacement occurred at the center of the fault plane away from the hypocenter and it was found to be 22.10 m. Dimensions of the faulting area are estimated to be 120 km for the fault length and 50 km for the fault width. These values are consistent with the empirical equations of Wells and Coppersmith (1994). According to these empirical equations; Fault Length = 123.0269 km, Fault Width = 53.7032 km, Fault Area = 7144.9632 km^{2}, Maximum Displacement = 25.0035 km for this event with the seismic moment of 2.295 x 10^{21} Nm (see Figure 3.14).

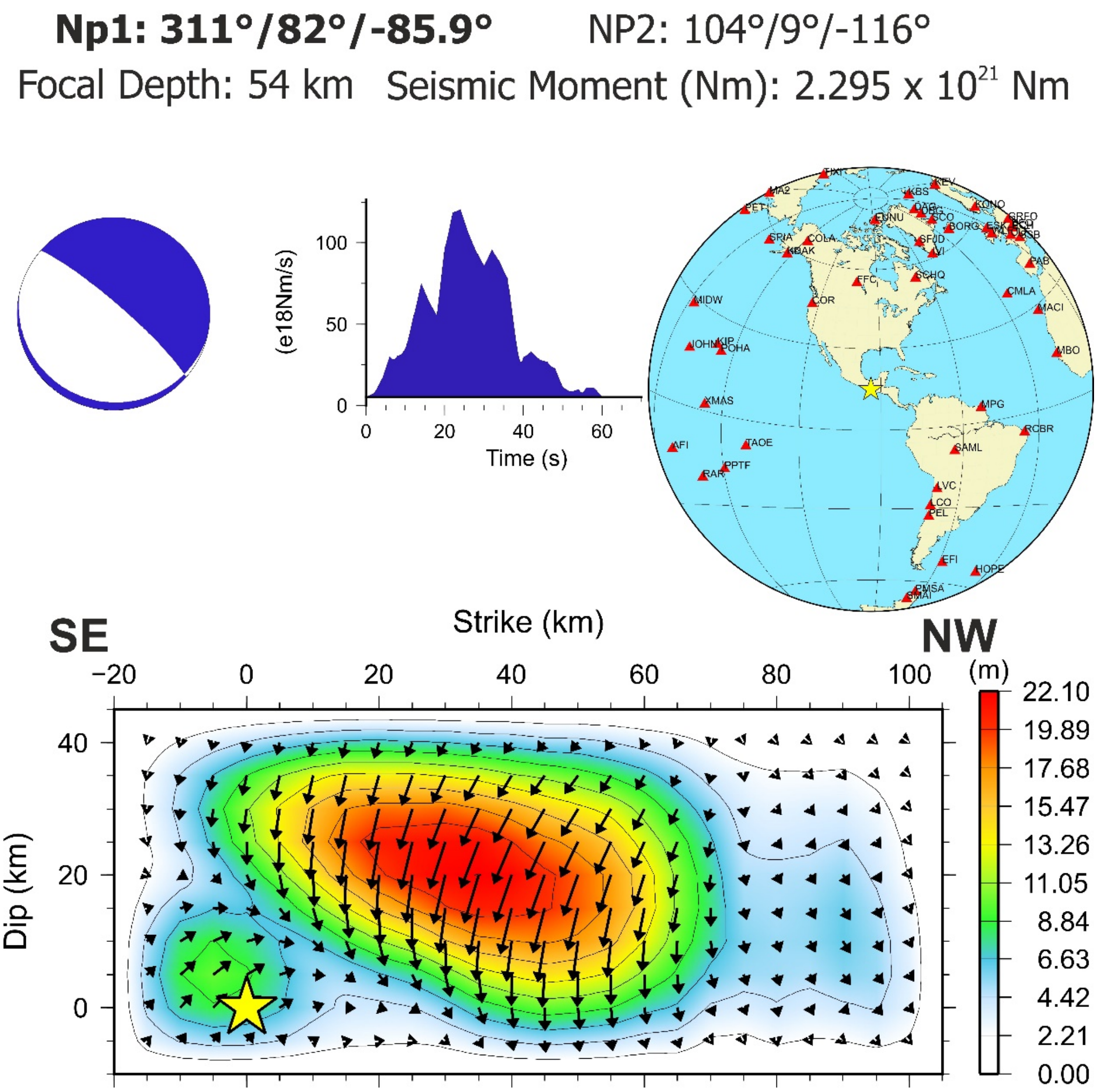

Figure 3.14 : Finite-fault slip distribution model of the September 08, 2017 Chiapas (M_W 8.2; Mexico) earthquake determined by slip inversion. Focal mechanism, source time function and teleseismic station distribution used in inversion are also provided.

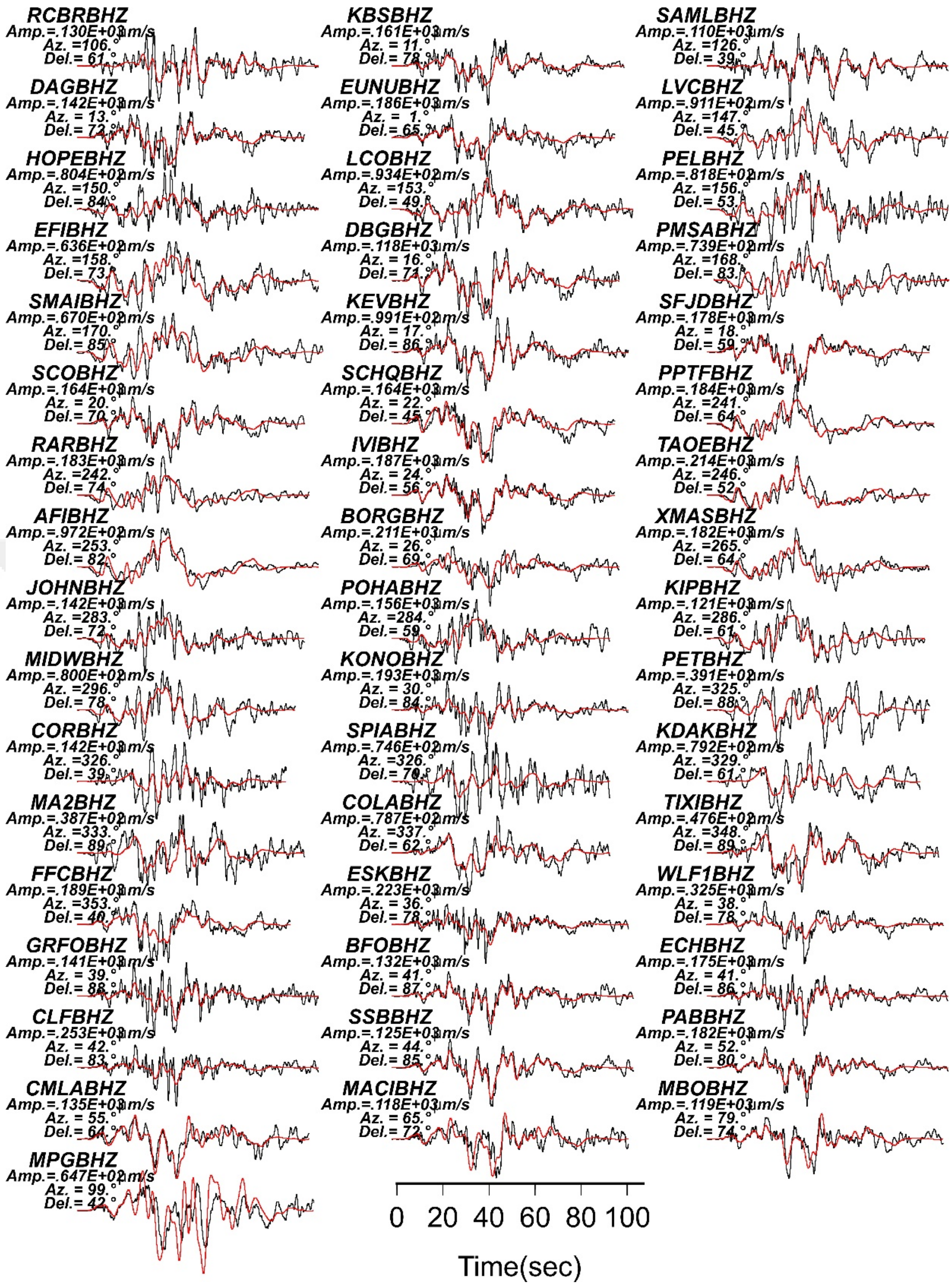

Figure 3.15 : Comparison of teleseismic 49 observed broad-band (BB) P-waveforms (black) and synthetic waveforms (red)

USGS-NEIC also reported a slip distribution model of 2017 Mexico earthquake using a finite-fault inversion algorithm (Ji et al., 2002). They assumed that the nodal plane that has a strike angle = 314° and a dip angle = 81° is the fault plane. The reported slip model indicates that the maximum displacement of 18 meter is at SW of the fault plane, the seismic moment release is 3.6 x 10^{21} dyne.cm, focal depth=47.4

km and the moment magnitude (M_w)=8.3 (Figure 3.16). The faulting area has a length of 120 km and width 70 km. Both slip models reported by USGS and this study indicate quite similar results. The differences betweeen the models can be attributed to selection of different stations with different frequency contents.

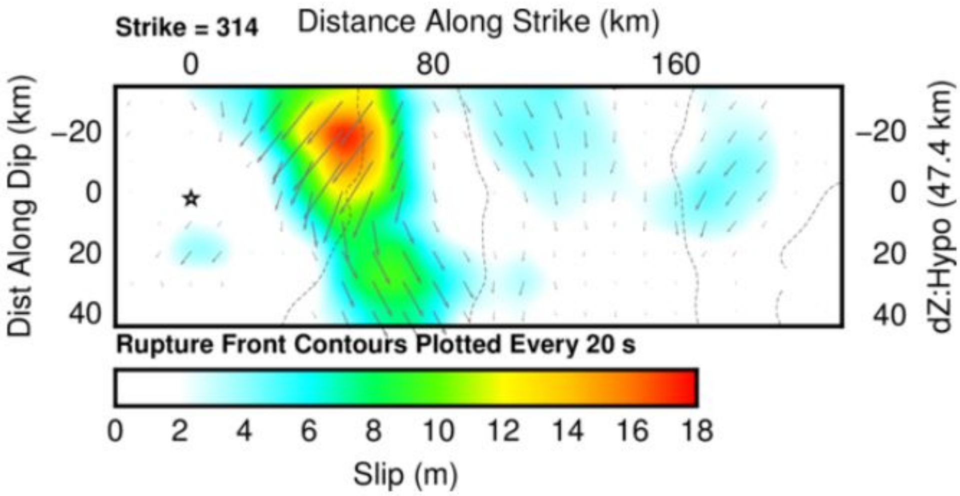

Figure 3.16 : USGS finite-fault slip distribution model(taken from https://earthquake.usgs.gov/earthquakes/eventpage/us2000ahv0/finite-fault)

In this study, numerical simulations of tsunami wave propagations are further performed for the 2017 Chiapas (Mexico) earthquake and associated tsunami based on the uniform slip model estimated from teleseismic body waveform inversions, and the initial tsunami wave is calculated. Tsunami simulation parameters are given in Figures 3.17 – 3.18 - 3.19. Computational layers used for simulations are shown in Figure 3.20. The through of the initial wave is found as 0.791 m, and the crest is calculated as -1.172 m (Figure 3.21). As input parameters, the length and the width of the fault plane (L=125 km × W=55 km) and the faulting geometry (strike φ=311°, dip δ=82°, rake angles λ=255°) determined from P-SH wave inversions are used. By using the relation of Aki and Richards (1980) for seismic moment ($M_o = \mu\, A\, D_{av}$), the average slip is calculated (D_{av}=5.2 m) and it is used as another input parameter for tsunami simulation. The rigidity value (μ) is taken as 7 x 10^{11} dyn/cm^2 as suggested by Adriano et al. (2017) for this region. In general, this value is taken around 3-4 x 10^{11} dyn/cm^2, but for this region the calculated tsunami waves have significantly high amplitudes using the average slip values calculated with the rigidity values of 3-4 x 10^{11} dyn/cm^2, and they do not coincide with the real tsunami data. It is observed that tsunami simulation results are in agreement with the records of DART buoys and tide gauges (Figures 3.22 and 3.23).

```
#=================================================:================
# General Parameters for Simulation               : Value Field    |
#=================================================:================
# Job Description: One-line brief description may be added here
 Total Simulated Duration (Wall clock, seconds) :  14400.000
 Time Interval for Snapshot Output    (seconds) :   120.0
 Zmax & Gauge Output  (0-ZMax Z;1-Gauge;2-Both) :     2
 Start Type (0-Cold start; 1-Hot start)         :     0
 Resuming Time for Hot Start          (Seconds) :  3600.00
 Minimum WaterDepth offshore           (meters) :    00.00         |
 Initial Cond. (0:FLT,1:File,2:WM,3:LS,4:FLT+LS):     0
 Boundary Cond.(0-Open;1-Absorb;2-Wall;3-FACTS) :     0
 Specify Filename of z Input (for BC=3, FACTS)  :23926h.asc
 Specify Filename of u Input (for BC=3, FACTS)  :23926u.asc
 Specify Filename of v Input (for BC=3, FACTS)  :23926v.asc
#
#=================================================:================
```

Figure 3.17 : Section of input file for COMCOT (comcot.ctl) for the 2017 Chiapas (Mexico) earthquake (Total simulated duration, time interval for output, output format, Initial conditions, etc.).

```
#=================================================:================
# Parameters for Fault Model (Segment 01)         :Values          |
#=================================================:================
 Number of FLT Planes (use fault_multi.ctl if>1):       1
 Rupture Start Time(,Uplift Duration)  (seconds):       0.0
 Faulting Option (0:Model-C; 1:Data; 9:Model-T) :       0
 Focal Depth                            (meters):   54000.000
 Length of Fault Plane                  (meters):  125000.000
 Width of Fault Plane                   (meters):   55000.000
 Dislocation of Fault Plane             (meters):       5.2
 Strike Angle (theta)                  (degrees):     311.000
 Dip  Angle (delta)                    (degrees):      82.000
 Slip/Rake Angle (lamda)               (degrees):     255.400
 Origin of Numerical Domain: Latitude  (degrees):      -8.0
 Origin of Numerical Domain: Longitude (degrees):    -106.0
 Epicenter Location: Latitude          (degrees):      15.022
 Epicenter Location: Longitude         (degrees):     -93.899
 File Name of Input Data                        :finite_fault.txt
 Data Format (0-COMCOT;1-MOST;2-XYZ;3-ASC)      :       2
#
#=================================================:================
```

Figure 3.18 : Section of input file for COMCOT (comcot.ctl) for the 2017 Chiapas (Mexico) earthquake including fault orientation parameters.

```
#===============================================:================
# Parameters for 1st-level grids -- layer 01    :Values         |
#===============================================:================
 Run This Layer ?       (0:Yes,       1:No     ):       0
 Coordinate System    (0-Spherical, 1-Cartesian) :      0
 Governing Equations (0-linear,    1-nonlinear) :       0
 Grid Size       (dx, sph:minutes, Cart:meters) :       2
 Time Step Size                      (seconds) :        1.0
 Bottom Friction Switch (0-ON;1-OFF;2-ON,Var.n) :       0
 Manning's n (for Fric.Switch=0), {land, water} :       0.025
 Output Option?   (0-Z+Hu+Hv; 1-Z Only; 2-NONE) :      0
 X_start                                        :    -106.0
 X_end                                          :     -85.0
 Y_Start                                        :      -8.0
 Y_end                                          :      17.0
 File Name of Bathymetry Data                   :  bathymetry.xyz
 Format  (0-OLD;1-MOST;2-XYZ BP;3-XYZ BN;4-ASC) :       3
 Grid Identification Number (ID)                :      01
 Grid Level                                     :       1
 Parent Grid Layer's ID Number                  :       0
#
#===============================================:================
#  Parameters for Sub-level grid -- layer 02    :Values         |
#===============================================:================
 Run This Layer ?       (0:Yes,       1:No     ):       0
 Coordinate System    (0:spherical, 1:cartesian) :      0
 Governing Equations (0:linear,    1:nonlinear) :       1
 Bottom Friction Switch (0-ON,1-OFF,2:ON,Var.n) :       0
 Manning's n (for Fric.Switch=0), {land, water} :       0.025
 Output Option? (0-Z+Hu+Hv; 1-Z Only; 2-NONE)   :       0
 GridSize Ratio of Parent Grid to Current Grid  :       4
 X_start                                        :    -97.00
 X_end                                          :    -92.00
 Y_Start                                        :     14.00
 Y_end                                          :     16.50
 File Name of Bathymetry Data                   :  bathymetry.xyz
 Format (0-OLD;1-MOST;2-XYZ BP;3-XYZ BN;4-ASC)  :       3
 Grid Identification Number (ID)                :      02
 Grid Level                                     :      2
 Parent Grid Layer's ID Number                  :      01
#
#===============================================:================
```

Figure 3.19 : Computational layer parameters for tsunami simulation of 2017 Chiapas (Mexico) earthquake. Defined bathymetry file with xyz format can be seen with the boundary coordinates.

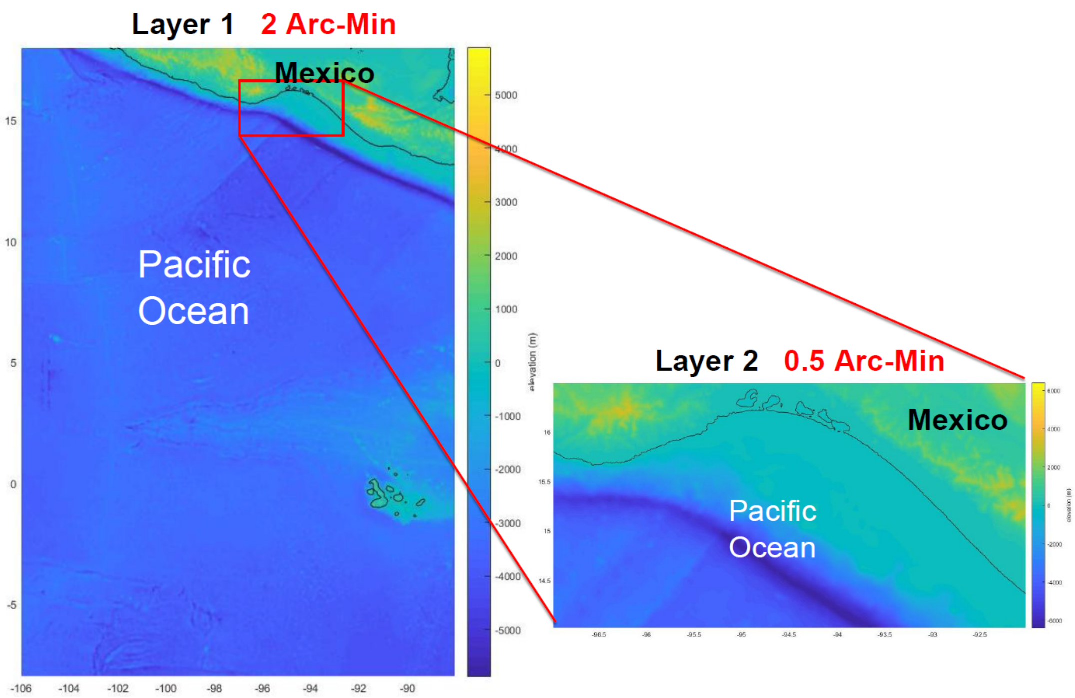

Figure 3.20 : Computational layers used for simulations of the 2017 Chiapas (Mexico) tsunami.

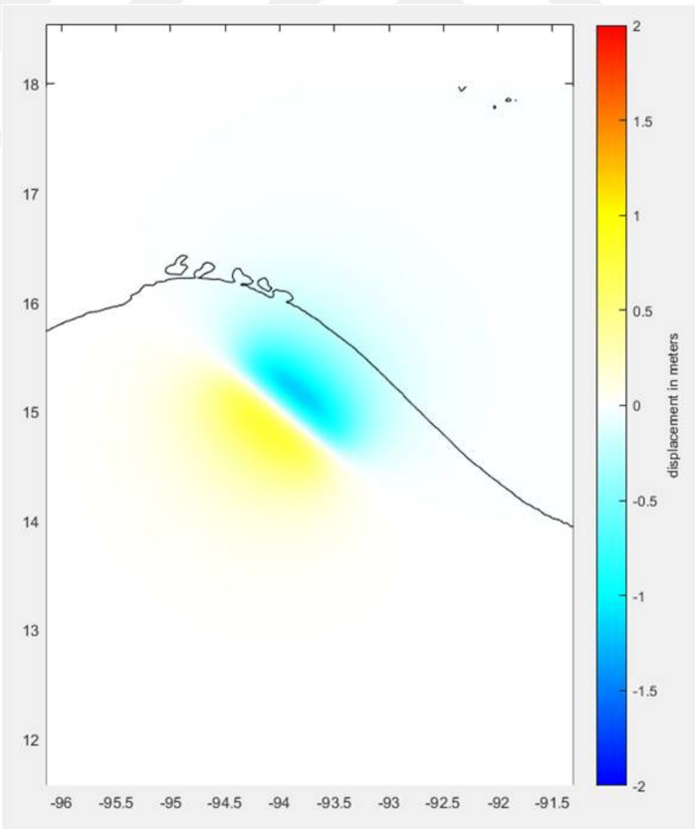

Figure 3.21 : Initial tsunami wave calculated using the uniform slip model in tsunami simulation of the 2017 Chiapas (Mexico) earthquake. The through and crest of the initial wave is found as 0.791 m, and -1.172m, respectively.

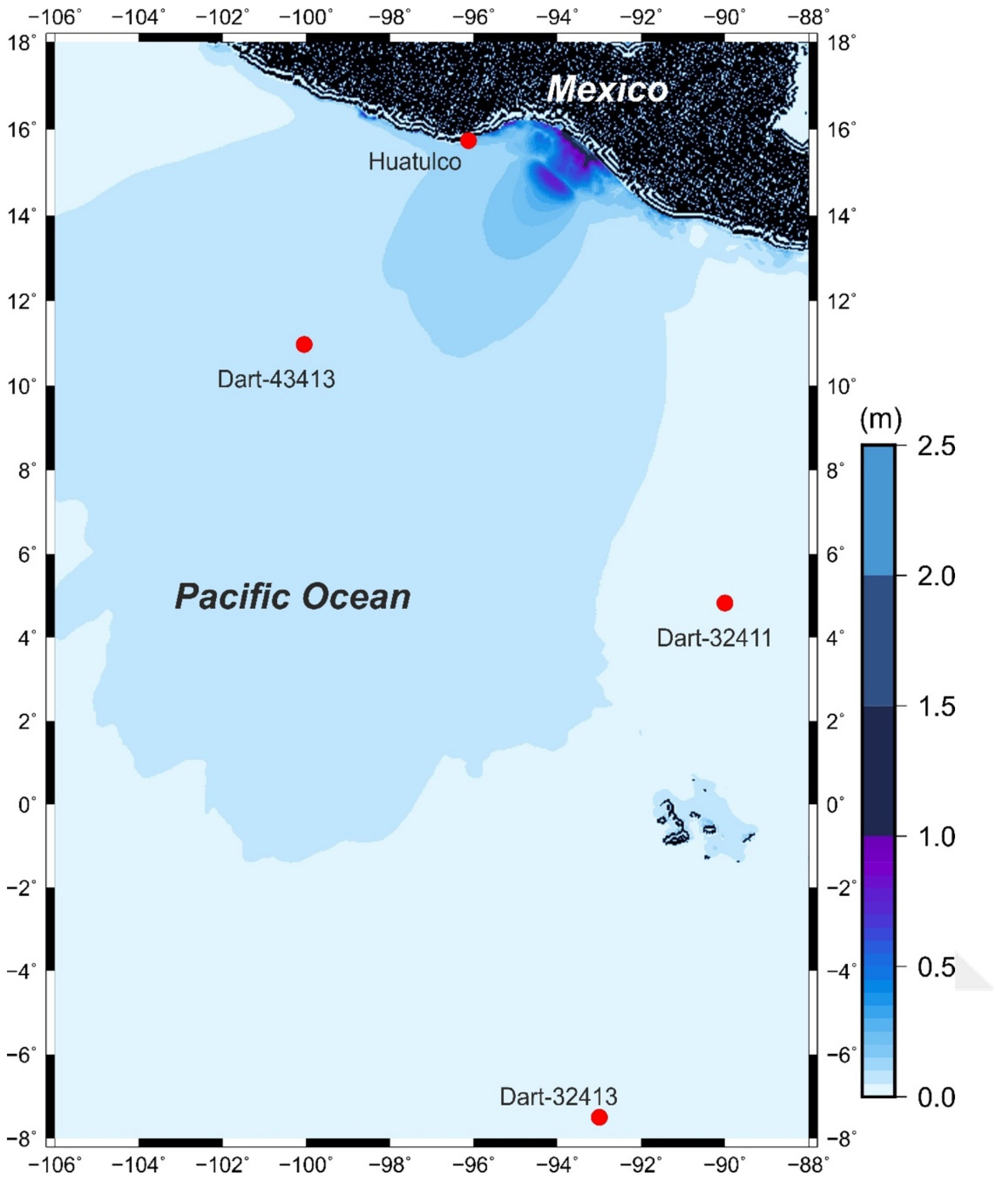

Figure 3.22 : Computed maximum tsunami wave heights for the September 08, 2017 Chiapas (Mexico) earthquake with a computational grid of 2 arcmin. Red dotes indicate the locations of the DART bouys and tide gauge station for comparing synthetic waveforms with the real data.

The real-time records of three DART buoys and one tide gauge stations are used in simulations (Table 3.2). In general, shape and amplitudes of the calculated waveforms are quite consistent with the observed data. The arrival times of the first tsunami waves are particulary compatible with the observed data recorded by DART buoys (see DART-32411, DART-32413 and DART-43413), however, there is an evident time shift for the record of Huatulco tide gauge station (see Figure 3.23). This inconsistency could be related to the lack of the high resolution bathymetry data used in simulation, since it is quite important especially for the near-field area where tide gauges are located.

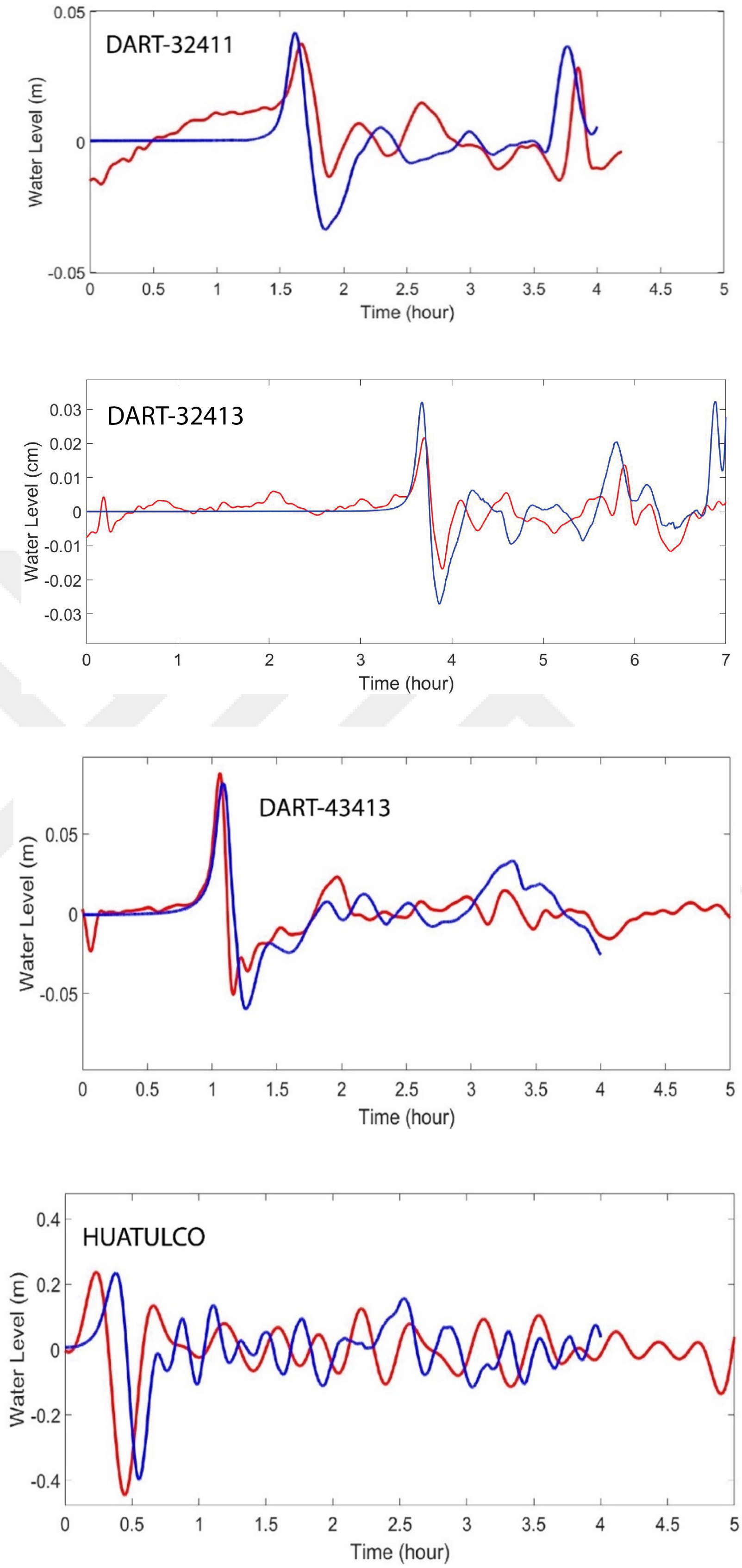

Figure 3.23 : Comparison of the real-time tsunami data (red) recorded by DART buoys and tide gauges with the calculated waveforms (blue).

Table 3.2 : The list of DART buoys and tide-gauges used in simulations of 2017 Mexico tsunami (NOAA-NDBC, IOC).

Station code	**Lat (°N)**	**Lon (°E)**
DART 32411	4.953	90.880
DART 32413	7.409	93.517
DART 43413	11.012	100.083
DART 32401	-20.474	-73.421
Huatulco	15.750	-96.116
Matarina	-17.0009	-72.1088
Taltal	-25.4081	-70.4916

4. DISCUSSION

In the scope of this MSc thesis, source mechanism parameters and finite-fault slip distribution models of the September 25, 2013 Acari - Peru (M_w 7.1) and September 08, 2017 Chiapas - Mexico (M_w 8.1) earthquakes have been obtained by using teleseismic P- and SH- body waveform modelling and hybrid back-projection slip inversions. Inversion of the earthquake data allows us to properly determine rupture geometry, focal depth, seismic moment, and kinematic and dynamic parameters of earthquakes such as faulting area, source duration, stress drop etc.. Furthermore, it is well known that seismological observations are crucial for simulating tsunami wave propagation especially for earthquake-induced tsunamis. In this study, numerical tsunami simulations of the 2013 Peru and 2017 Chiapas (Mexico) earthquakes based on uniform slip distribution models are performed. This type of studies are important for hazard mitigation in order to save human lives and to prevent severe destruction of the populated areas.

The results of this MSc. thesis enhance our understanding of seismicity distribution along the major subduction zones, the details of rupture propagations on fault planes of earthquakes, characteristics of earthquake-induced tsunamis that occur on subduction zones and how these events affect the coastal plains of the regions. They can be used as input for defining the endangered areas by tsunamis and earthquakes that may occur in the future. Preliminary results reported by the major institutes and research centers such as USGS, Harvard-CMT etc. give insight about the events; but they are in general not reliable if it is used in order to investigate the tectonic features, seismic periodicity, fault orientation, and hazard mitigation in details for study regions. Particularly, they provide inadequate results for the focal depth and rupture characteristics. Focal mechanism solutions shown in this thesis are obtained from the inversion of seismic data taken from seismic stations at teleseismic distances with good azimuthal distribution all around the globe. Input data was carefully selected for focal mechanism solutions, finite-fault slip distribution models and tsunami simulations. However, it is seen that one of the most important shortcomings of this study is the low number of SH- waves used in the estimation of focal mechanism solutions of earthquakes.

For the September 25, 2013 Acari-Peru (M_w 7.1) earthquake, teleseismic body waveform inversion results show a NW-SE trending reverse faulting mechanism (strike/dip/rake angles: 322°/27°/89°) at shallow focal depth of 48 km. Considering that this earthquake has been occurred on the Peru-Chile subduction zone we can assume that it occurred on the fault interface. P-wave first motion polarities are checked and they are compatible with the focal mechanism solution obtained by the waveform inversion. Also these results have been compared with the results of Harvard-CMT and USGS. Focal mechanism solution of this study has better fit with the P-wave first motion polarities than the other reported solutions. As a result of finite-fault slip inversion the details of slip distribution on the fault plane is obtained and it reflects similar results with the body waveform inversion. According to the finite-fault slip model, the maximum displacement occurred on the NW and SE side of the epicentre with 1.50 m. Furthermore, by using the results from the focal mechanism solutions as input, numerical tsunami simulation has been conducted. Using uniform fault model initial tsunami wave has been modeled and waveform propagation is calculated throughout the open-ocean. DART buoy named DART-32401 and tide gauges Matarina and Taltal were investigated for comparing the simulated tsunami waves with real-time recorded tsunami wave data. Due to the fact that the absence of high resolution bathymetry data, a large number of tide gauge stations could not be used in simulations. Since the tide gauges are stationed at coasts their locations migth be interpretted as inland. Also it is essential to have high resolution bathymetry in order to simulate ocean water level change at coastal regions since with shoaling, the effects of the complex bathymetry increases and higher bathymetric/computational resolution is needed. The 2013 Acari-Peru (M_w 7.1) earthquake, did not generate significant tsunami waves because it has small average (D_{av}:0.95 m) and maximum displacement (D_{max}: 1.50 m) values. It is shown that the calculated tsunami wave amplitudes are low and with the low bathymetric resolution it is not possible to reach detailed synthetic tsunami waves especially for tide gauge stations.

Furthermore, teleseismic body waveform inversion of the September 08, 2017 Chiapas - Mexico (M_w 8.1) earthquake show a NW – SE trending normal faulting mechanism (strike/dip/rake angles: 311°/82°/-105°) with a small amount of strike-slip component at shallow focal depth of 54 km. This earthquake is occurred near the Tehuantepec seismic gap. It is called a seismic gap because this area has been quite for over a century and no earthquake is occured since 1993 (Singh et al. 1981, 2008). This seismic gap represents high threat to nearby Mexico City and defined as Cocos Plate subducting under North American Plate. Since most of the tsunami generated earthquakes have low dip values (lower than 30°) it is an interesting tsunamigenic earthquake because it occurred on the NE dipping fault plane with the high dip angle and it shows a normal faulting mechanism rather than a regular megathrust earthquakes that occur along the Middle Americas. Also the obtained results are compared with those reported by Harvard-CMT, USGS, Ramirez-Herrera et al. (2017), Ye et al. (2017) and Adriano et al. (2017). It can be seen that the results of this study constrained the dip angle better than the results of the other studies. Given the finite-fault slip model, the maximum displacement occurred on the NE side of the epicentre with 22.10 m. Tsunami simulation based on the uniform slip model that was set by source parameters obtained by this study was also conducted for this earthquake. The obtained results are compatible with the real-time tsunami data. However, tsunami simulations based on non-uniform slip models should be perfomed in future studies to determine more well-matched waveforms with the observed data. Furthermore, this earthquake and associated tsunami have been studied by many researchers (e.g., Okuwaki and Yagi, 2017; Adriano et al., 2017; Gusman et al., 2017; Ramírez-Herrera et al., 2018; Heidarzadeh et al., 2018). Adriano et al. (2017) investigated tsunami wave propagation using a source model focusing on the tsunami signals recorded at nearby tide gauge stations based on aftershock distribution of the earthquake 1 day prior to main event and inversion of tsunami waves. The crest and through of initial tsunami wave calculated as 0.4 m and -0.4 m, respectively. These values are consistent with the findings of this thesis. The comparison of analyzed DART and tide gauge data betweeen this study and Adriano et al. (2017) shows high similarities. Heidarzadeh et al (2018) conducted a finite-fault slip model using teleseismic body-wave inversions, and they investigated the best-fitting rupture velocity (V_r) value for this earthquake. Then they conducted a non-uniform tsunami simulation using the finite-fault slip distribution model. They obtained relatively less amplitude values than the results of this study. This difference can be attributed to the use of different source models used for calculating the ocean bottom deformation. Since non-uniform source models have less slip values on the edges rather than the uniform slip models, they usually give higher amplitude values. Gusman et al. (2017) also reported the maximum sea surface uplift of 0.5 m located very close to trench and extends beyond it. These results agree with the output of the tsunami simulation conducted for this destructive earthquake in this thesis (see Figures 4.1 – 4.4).

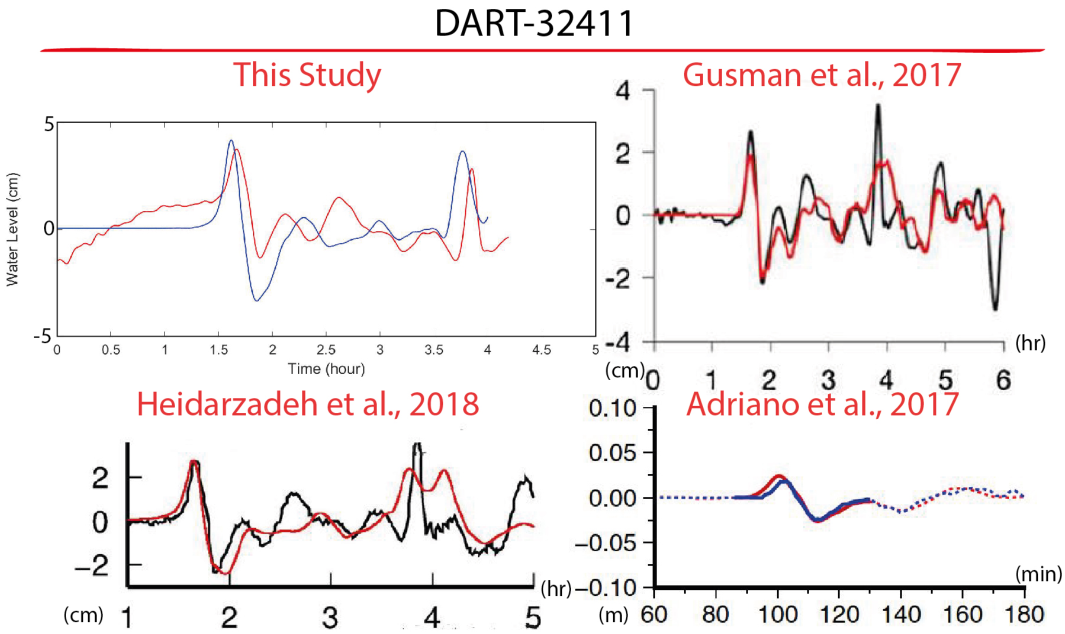

Figure 4.1 : Comparison of real time tsunami waves with synthetic waves recorded at DART-32411 from the studies of Gusman et al., (2017), Heidarzadeh et al., (2018), Adriano et al., (2017) and this study.

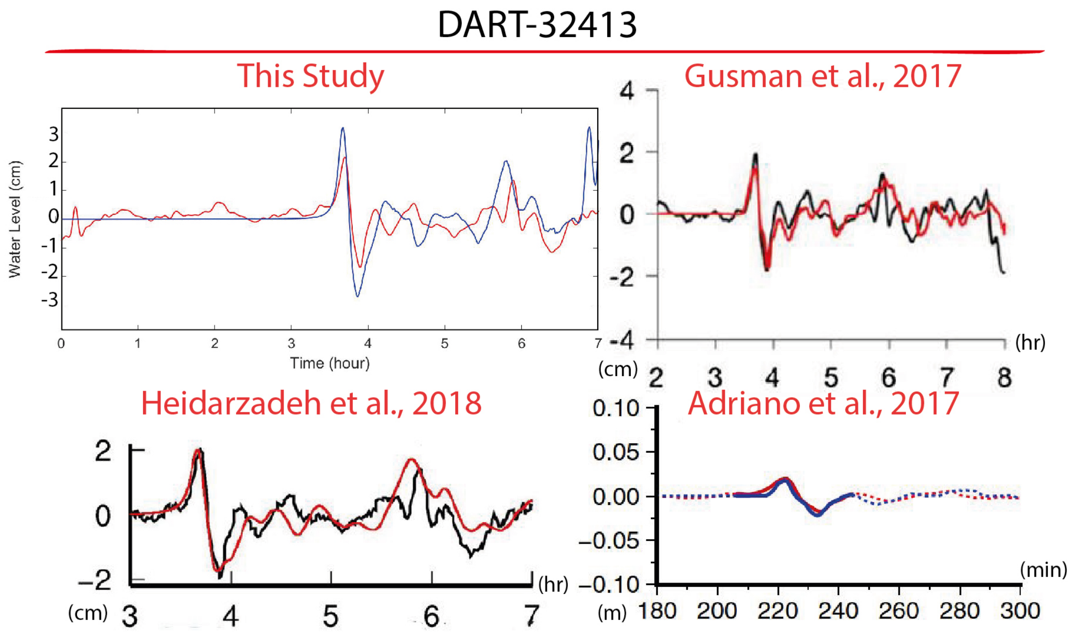

Figure 4.2 : Comparison of real tsunami waves with synthetic waves recorded at DART-32413 from the studies of Gusman et al., (2017), Heidarzadeh et al., (2018), Adriano et al., (2017) and this study.

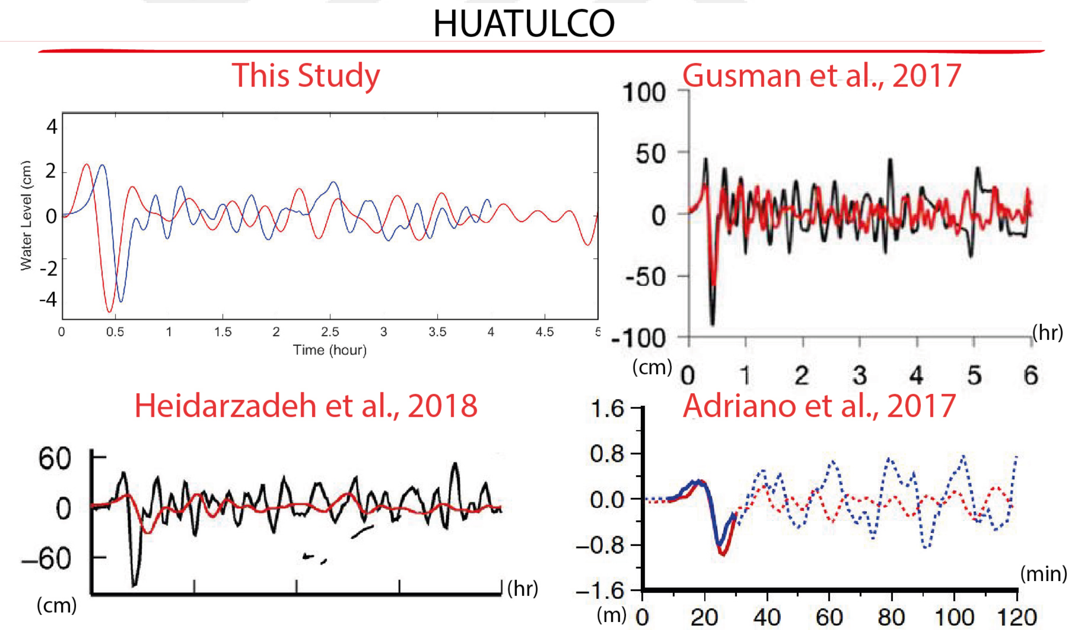

Figure 4.3 : Comparison of real time tsunami waves with synthetic waves recorded at Huatulco from studies of Gusman et al., (2017), Heidarzadeh et al., (2018), Adriano et al., (2017) and this study.

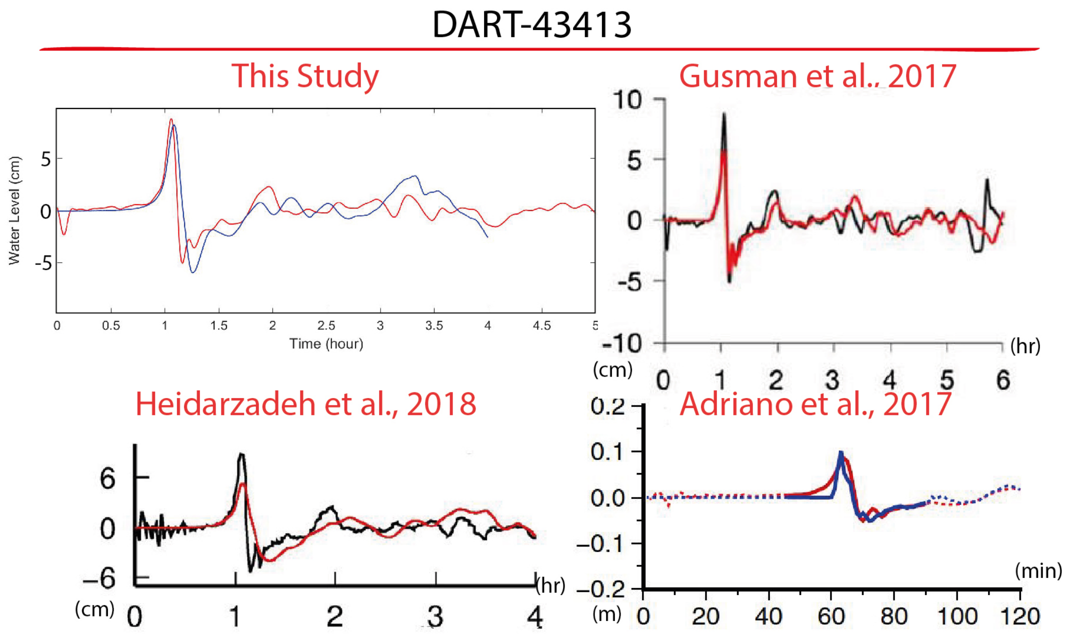

Figure 4.4 : Comparison of real time tsunami waves with synthetic waves recorded at DART-43413 from the studies of Gusman et al., (2017), Heidarzadeh et al., (2018), Adriano et al., (2017) and this study.

REFERENCES

Adriano, B., Fujii, Y., Koshimura and S. et al. (2017). Tsunami Source Inversion Using Tide Gauge and DART Tsunami Waveforms of the 2017 Mw8.2 Mexico Earthquake. *Pure Appl. Geophys.* 175: 35. https://doi.org/10.1007/s00024-017-1760-2

Aki, K. and Richards P. G. (1980). Quantitative Seismology, Theory and Methods. *Geological Magazine*. 118. 208. 10.1017/S0016756800034439.

Bilek, S.L., (2010). Seismicity along the South American subduction zone: Review of large earthquakes, tsunamis, and subduction zone complexity, *Tectonophysics*, Volume 495, Issues 1–2, 2010, Pages 2-14, ISSN 0040-1951, https://doi.org/10.1016/j.tecto.2009.02.037.

Calisto I., Miller M. and Constanzo I. (2017). Comparison Between Tsunami Signals Generated by Different Source Models and the Observed Data of the Illapel 2015 Earthquake. In: Braitenberg C., Rabinovich A. (eds) The Chile-2015 (Illapel) Earthquake and Tsunami. *Pageoph Topical Volumes*. Birkhäuser, Cham

Chacón-Barrantes, S. (2018). The 2017 México Tsunami Record, Numerical Modeling and Threat Assessment in Costa Rica. *Pure Appl. Geophys.* 175: 1939. https://doi.org/10.1007/s00024-018-1852-7

Cho, I., Nakanishi, I., Kazutoshi, I. and Sato, T. (1995). The CMT Solution of the 1994 October 4 Shikotan Island Earthquake (MJMA=8.1) Recorded by Broad-band Strong-motion Seismographs. Zisin, *Journal of the Seismological Society of Japan*. 2nd ser.). 48. 353-364. 10.4294/zisin1948.48.3_353.

Cifuentes, I., (1989). The 1960 Chilean earthquakes. *J. Geophys. Res*. 94, 665–680. http:// dx.doi.org/10.1029/JB094iB01p00665.

Condori, C., França, G.S, Tavera, H.J, Albuquerque, D.F, Bishop, B.T. and Beck, S.L. (2017). Crustal structure of north Peru from analysis of teleseismic receiver functions, *Journal of South American Earth Sciences*, Volume 76, 2017, Pages 11-24, ISSN 0895-9811, https://doi.org/10.1016/j.jsames.2017.02.006.

Couch, R., and Woodcock, S. (1981). Gravity and structure of the continental margins of southwestern Mexico and northwestern Guatemala: *Journal of Geophysical Research*, v. 86, p. 1829–1840.

Dziewonski, A.M. and Anderson, D.L. (1981). Preliminary Reference Earth Model (PREM), *Phys. Earth Planet. Inter*. 25, 297-356.

Geist, E.L. (2000). Papua New Guinea tsunami: Earthquake or landslide: *Seismological Research Letters*, v. 71, no. 3, p. 344-351.

Geist, E. L. (2002). Complex earthquake rupture and local tsunamis, *J. Geophys. Res*., 107(B5), doi: 10.1029/2000JB000139.

Goldstein, P., Dodge, D., Firpo, M. and Minner, L. (2003). SAC2000: signal processing and analysis tools for seismologists and engineers, *Int.Geophys*., 81, 1613–1614.

Gusman, A., Mulia, I. and Satake, K. (2017). Optimum Sea Surface Displacement and Fault Slip Distribution of the 2017 Tehuantepec Earthquake (Mw 8.2) in Mexico Estimated From Tsunami Waveforms. *Geophysical Research Letters*. 10.1002/2017GL076070.

Fielding, E.J., Lundgren, P.R., Taymaz,T., Yolsal-Çevikbilen, S. and Owen, S.E. (2013). Fault-Slip Source Models for the 2011 M7.1 Van Earthquake in Turkey from SAR Interferometry, Pixel Offset Tracking, GPS and Seismic Waveform Analysis, *Seismological Research Letters*, July-August 2013, Vol: 84 (4), pp: 579-593, SRL-D-12-00164, https://doi.org/10.1785/0220120164.

Fan, W., D. Bassett, J. Jiang, P. M. Shearer, and C. Ji. (2017). Rupture evolution of the 2006 Java tsunami earthquake and the possible role of splay faults, *Tectonophysics*, doi: 10.1016/j.tecto.2017.10.003,

Futterman,W. I. (1962). Dispersive body waves, J. Geophys. Res., 67(13), 5279–5291, doi:10.1029/JZ067i013p05279.

Franco, S.I., Kostoglodov, V., Larson, K.M., Manea, V.C., Manea, M., and Santiago, J.A. (2005). Propagation of the 2001 – 2002 silent earthquake and interplate coupling in the Oaxaca subduction zone, *Mexico, Earth Planets Space*, 57, 973 – 985.

Hayes, G.P., Smoczyk, G.M., Benz, H.M., Villaseñor, A., and Furlong, K.P. (2015). Seismicity of the Earth 1900–2013, Seismotectonics of South America (Nazca Plate Region): *U.S. Geological Survey Open-File Report* 2015–1031–E, 1 sheet, scale 1:14,000,000, https://dx.doi.org/10.3133/ofr20151031E.ISSN 2331-1258 (online).

Heidarzadeh, M., Ishibe, T. and Harada, T. (2018). Constraining the Source of the Mw 8.1 Chiapas, Mexico Earthquake of 8 September 2017 Using Teleseismic and Tsunami Observations. *Pure and Applied Geophysics*. 175. 10.1007/s00024-018-1837-6.

Ji, C., Wald, D. J. and Helmberger, D. V. (2002). Source description of the 1999 Hector Mine, California, earthquake, part I: Wavelet domain inversion theory and resolution analysis. *Bulletin of the Seismological Society of America,* 92(4): p. 1192-1207.

Jiménez, C. (2018). Seismic source characteristics of the intraslab 2017 Chiapas-Mexico earthquake (Mw8.2), *Physics of the Earth and Planetary Interiors*, Volume 280, 2018, Pages 69-75, ISSN 0031-9201, doi:https://doi.org/10.1016/j.pepi.2018.04.013.

Jost, M. L. and Herrmann R. B. (1989). A Student's Guide to and Review of Moment Tensors, *Seismological Research Letters*, April-June 1989, v. 60, p. 37-57, doi:10.1785/gssrl.60.2.37

Julian, B.R. and. Gillian R. F. (1998). Non-Double-Couple Earthquake Mechanisms, I. *Theory, Rev. Geophys*., 36, 525-549.

Kanamori, H. and Anderson, D.L. (1975). Theoretical Basis of Some Empirical Relations in Seismology. *Bulletin of the Seismological Society of America*, 65, 1073-1095.

Kanamori, H. and Cipar, J.J. (1974). Focal processes of the Great Chilean earthquake May 22, 1960. *Phys. Earth Planet. Inter*. 9, 128–136.

Kasahara, K. (1981). Earthquake mechanics, *Cambridge University Press*.

Kawasaki, I. (1982). A method for the near-source anisotropy by the pair-event inversion of Rayleigh-wave radiation patterns. *Geophysical Journal of* *the Royal Astronomical Society*, 71: 395-424. doi:10.1111/j.1365-246X.1982.tb05995.x

Kelleher, J., Sykes L., and Oliver J. (1973).Possible criteria for predicting earthquake locations and their application to major plate boundaries of the Pacific and the Caribbean, *J. Geophys. Res.*, 78(14), 2547–2585, doi: 10.1029/JB078i014p02547.

Kelleher, J., and McCann., W. (1976). Buoyant zones, great earthquakes, and unstable boundaries of subduction, *J. Geophys. Res*., 81, 4885-4896.

Kikuchi, M., Kanamori, H., (1991). Inversion of complex body waves—III. *Bulletin of the Seismological Society of America*; 81 (6): 2335–2350.

Komar, P.D. (1998). Beach processes and sedimentation, *Prentice-Hall*, second edition, 544 p.

Lay, T. and Wallace, T.C. (1995). Modern Global Seismology, *Academic Press*, ISBN #0-12-732870-X.

Lim, H., Kim, Y.H., Clayton, R.W. and Thurber, C.H., (2018). Seismicity and structure of Nazca Plate subduction zone in southern Peru, *Earth and Planetary Science Letters*, Volume 498, 2018, Pages 334-347, https://doi.org/10.1016/j.epsl.2018.07.014.

Liu PL. F., Woo, S.B. and Cho, Y.S. (1998). Computer programs for tsunami propagation and inundation. *Cornell University*, Ithaca

McCaffrey, R., and Abers, G. (1988). Active deformation in the New Guinea fold-and-thrust belt: Seismological evidence for strike-slip faulting and basement-involved thrusting. *Journal of Geophysical Research*. 931. 13332-13354. 10.1029/JB093iB11p13332.

McCaffrey, R., and Abers, G. and Zwick, P. (1991). Inversion of teleseismic body waves. *IASPEI Software Library*. 3. 81-166.

McCaffrey, R., and Nabelek, J. (1987). Earthquakes, gravity, and the origin of the Bali Basin: An example of a Nascent Continental Fold-and-Thrust Belt. *Journal of Geophysical Research*. 92. 441-460. 10.1029/JB092iB01p00441.

McNally, K. C., and Minster, J. B. (1981). Nonuniform seismic slip rates along the Middle America Trench, *J. Geophys. Res*., 86(B6), 4949–4959, doi:10.1029/JB086iB06p04949.

Mendoza, C., (1996). Rapid Derivation of Rupture History for Large Earthquakes. *Seismological Research Letters*; 67 (6): 19–26. doi:https://doi.org/10.1785/gssrl.67.6.19

Mendoza, C. (1993). Coseismic slip of two large Mexican earthquakes from teleseismic body waveforms: Implications for asperity interaction in the Mihoacan plate boundary segment. *J Geophys. Res.* 98, 8197-8210

Nabelek, J. N. (1984). Determination of source parameters from inversion of body waves, (Ph. D. Thesis). Massachusetts Institute of Technology, *Dept. of Earth, Atmospheric and Planetary Sciences*. Massachusetts.

Nishenko, S. P. (1991). Circum-Pacific seismic potential – 1989-1999, *Pure Appl. Geophys*., 135, 169-259.

Oishi, Y., Imamura, F. and Sugawara, D. (2015), Near- field tsunami inundation forecast using the parallel TUNAMI- N2 model: Application to the 2011 Tohoku- Oki earthquake combined with source inversions. *Geophys. Res. Lett.*, 42: 1083– 1091. doi: 10.1002/2014GL062577.

Okada, Y. (1985). Surface deformation due to shear and tensile faults in a half-space. *Bulletin of the Seismological Society of America*; 75 (4): 1135–1154.

Okuwaki, R. and Yagi, Y. (2017). Rupture Process during the Mw 8.1 2017 Chiapas Mexico Earthquake: Shallow Intraplate Normal Faulting by Slab Bending. *Geophys. Res. Lett.* 44. https://doi.org/10.1002/2017GL075956

Pardo, M. and Suarez, G. (1995). Shape of the subducted Rivera and Cocos plates in southern Mexico: Seismic and tectonic implications. *J. Geophys. Res*., 100, 12,357- 12,373.

Plesinger, A. and Musil, M. (1996). Discrimination between local microearthquakes and quarry blasts by multi-layer perceptrons and Kohonen maps, *Bullettin of seismological Society of America*., 86, 1077–1090.

Ponce, L., Suarez, G., and Lomas, E. (1992). Geometry and state of stress of the downgoing Cocos plate in the Isthmus of Tehuantepec, Mexico, *Geophys. Res. Lett*., 19, 773-776.

Rabinovich, A. B., Vilibić, I. and Tinti, S. (2009). Meteorological tsunamis: Atmospherically induced destructive ocean waves in the tsunami frequency band, *Physics and Chemistry of the Earth*, Parts A/B/C, Volume 34, Issues 17–18, 2009, Pages 891-893, ISSN 1474-7065, https://doi.org/10.1016/j.pce.2009.10.006.

Ramírez-Herrera, M., Corona, N., Ruiz-Angulo, A., Melgar, D. and Zavala-Hidalgo, J. (2017). The 8 September 2017 Tsunami Triggered by the Mw 8.2 Intraplate Earthquake, Chiapas, Mexico. *Pure and Applied Geophysics*. 175. 10.1007/s00024-017-1765-x.

Rost, S., and Thomas C. (2002). Array seismology: Methods and applications, *Rev. Geophys*., 40 (3), 1008, doi: 10.1029/2000RG0001002002.

Ruiz, S., and Madariaga, R. (2018). Historical and recent large megathrust earthquakes in Chile, *Tectonophysics*, Volume 733, 2018, Pages 37-56, ISSN 0040-1951,https://doi.org/10.1016/j.tecto.2018.01.015.

Saltogianni, V., Gianniou M., Taymaz, T., Yolsal-Çevikbilen, S., Stiros, S. and (2015). Fault slip source models for the 2014 Mw 6.9 Samothraki-Gökçeada earthquake (North Aegean trough) combining geodetic and seismological observations, *Journal of Geophysical Research*: Solid Earth,

Saltogianni, V., Taymaz, T., Yolsal-Çevikbilen, S., Eken, T., Moschas, F. and Stiros, S. (2017). Fault model for the 2015 Leucas (Aegean Arc) earthquake: Analysis based on seismological and geodetic observations, *Bull. Seism. Soc. Am*., 107, 433–444, doi:10.1785/0120160080. v. 120, p. 8610-8622.

Sipkin, S.A. (1986). Estimation of Earthquake Source Parameters by the Inversion of Waveform Data: Global Seismicity 1981-1983, *Bulletin of the Seismological Society of America*. v. 76, p. 1515-1541.

Singh, S. K., Astiz, L., and Havskov, J. (1981). Seismic Gaps and Recurrence Periods of Large Earthquakes Along the Mexican Subduction Zone: A Reexamination, *Bulletin of the Seismological Society of America*, Vol. 71, No. 3, pp. 827-843.

Singh, S. K., Pérez-Campos, X., Iglesias, A. and Pacheco, J. (2008). An exploratory study for rapid estimation of critical source parameters of great subduction-zone earthquakes in Mexico. *Geofísica Internacional*. 47.

Singh, S. K., Shapiro M.N., Iglesias-Mendoza A., Cruz-Atienza V. and Pacheco J. (2000). Popocatepetl, an active volcano, reduce seismic hazard to Mexico City. *Geophys Res Lett* 27:2753–2756

Smith, W. H. F. and Sandwell, D.T. (1997). Global sea floor topography from satellite altimetry and ship depth soundings. *American Association for the Advancement of Science*. Vol. 277, pp. 1956-1952

Sözdinler, C., Yalçıner, A., Zaytsev, A., Suppasri, A. and Imamura, F. (2015). Investigation of Hydrodynamic Parameters and the Effects of Breakwaters During the 2011 Great East Japan Tsunami in Kamaishi Bay. *Pure and Applied Geophysics*. 172. 10.1007/s00024-015-1051-8.

Spagnotto, S., Alvarez, O. and Folguera, A. (2018). Static Stress Increase in the Outer Forearc Produced by M_W 8.2 September 8, 2017 Mexico Earthquake and its Relation to the Gravity Signal *Pure Appl. Geophys.* 175: 2575. https://doi.org/10.1007/s00024-018-1962-2

Stein, S. and Wysession, M. (2003). An Introduction to Seismology, Earthquakes, and Earth Structure

Suárez, G.and Albini, P., (2009). Evidence for great Tsunamigenic Earthquakes (M 8.6) along the Mexican Subduction Zone. BSSA 99 (2A), 892–896.

SLSMF (2015). Sea Level Station Monitoring Facility. Station Lists. http://www.ioc-sealevelmonitoring.org/list.php.

Tan, O., Sato, T., Kasahara, J., Taymaz, T., Ito, M., Kamimura, A. and Hayakawa, T. (2004). A study of microearthquake seismicity and focal mechanisms within the Sea of Marmara (NW Turkey) using ocean bottom seismometers (OBSs). *Tectonophysics*. 391 1-4 p 303-314

Tapley, W.C., Tull, J.E. (1992). SAC —Seismic Analysis Code: Users Manual, Revision 4,. Lawrence Livermore National Laboratory. 388pp

Taymaz, T. (1990). Earthquake source parameters in the eastern Mediterranean region, (Ph. D. Thesis) University of Cambridge, CAMBRIDGE.

Taymaz, Tuncay, Eyidogan, H. and Jackson, J.A. (1991b). Source Parameters of large earthquakes in the East Anatolian Fault Zone (Turkey), *Geophysical Journal* International-Oxford, 106, 537-550.

Taymaz, T., Jackson, J. and McKenzie, D. (1991a). Active tectonics of the north and central Aegean Sea, *Geophysical Journal International-Oxford*. 106, 433-490.

Taymaz, T., Jackson, J. and Westaway, R. (1990). Earthquake mechanisms in the Hellenic Trench near Crete. *Geophysical Journal International-Oxford*, 102: 695-731. doi:10.1111/j.1365-246X.1990.tb04590.x

Taymaz, T., Tan, O. and Yolsal, S. (2005). Sumatra Earthquake (Mw~9.0) of December 26, 2004 Source Rupture Processes and Slip Distribution Modelling Preliminary Rupture Model

Taymaz, T., Tan, O. and Yolsal, S. (2008). Recent Devastating Earthquakes in Turkey and Active Tectonics of the Aegean and Marmara Seas, *In: Proceedings of* the NATO-Science Series: IV. Earth and Environmental Sciences - Vol. 81: Earthquake Monitoring and Seismic Hazard Mitigation in Balkan Countries (ed. Eystein S. Husebye), Borovetz, Bulgaria, September 11-18, 2005, 289 pages, pp.

47-57, doi:10.1007/978-1-4020-6815-7, ISBN:978-1-4020-6813-3, MARCH 2008.

Taymaz, T., Wright, T., Yolsal, S., Tan, O., Fielding, E. and Seyitoğlu, G. (2007). Source Characteristics of June 6, 2000 Orta-Çankırı (Central Turkey) Earthquake: a synthesis of seismological, geological and geodetic (InSAR) observations, and internal deformation of Anatolian plate. *In:* The Geodynamics of the Aegean and Anatolia (eds. Tuncay Taymaz, Yücel Yılmaz & Yıldırım Dilek), pp. 259-290, The Geological Society of London, *Special Publications Book*, Vol: 291, ISBN: 978-1-86239-239-7, DECEMBER 2007.

Tinti, S., Bortolucci, E. and Armigliato, A. (1999). Numerical simulation of the landslide-induced tsunami of 1988 on Vulcano Island, Italy *Bull Volcanol* 61: 121. https://doi.org/10.1007/s004450050267

Tréhu, A. M., and Solomon S. C. (1983). Earthquakes in the Orozco Transform Zone: Seismicity, source mechanisms, and tectonics, *Journal of Geophysics. Res.,* 88(B10), 8203–8225, doi: 10.1029/JB088iB10p08203.

Wang, X. (2009). User Manual for COMCOT version 1.7 (first draft), Cornell University

Wei, S. Helmberger, D., Owen, S., Graves, R. W., Hudnut, K. W. and Fielding, E. J. (2013). Complementary slip distributions of the largest earthquakes in the 2012 Brawley swarm, Imperial Valley, California, *Geophys. Res. Lett.,* 40, 847–852, doi: 10.1002/grl.50259.

Wells D. L. and Coppersmith K. J. (1994). New empirical relationships among magnitude, rupture length, rupture width, rupture area, and surface displacement. *Bull. Seismol. Soc. Am.* 84, 4 (1994), 975–1002.

Wessel, P., and Smith, W. H. F. (1998). New, improved version of generic mapping tools released, Eos Trans. AGU, 79(47), 579579. doi:10.1029/98EO00426.

Woodhouse, J. H. and Dziewonski A. M. (1984). Mapping the upper mantle: Three dimensional modelling of earth structure by inversion of seismic waveforms, *Journal of Geophysics. Res*. 89, 5953-5986.

Yagi, Y. and Kikuchi, M. (2000). Source rupture process of the Kocaeli, Turkey, earthquake of August 17, 1999, obtained by joint inversion of near-field data and teleseismic data, *Geophys. Res. Lett*., 27, 1969–1972,.

Yagi, Y., Mikumo, T. and Pacheo, J. (2004). Source rupture process of the Tecoman, Colima, Mexico earthquake of January 22, 2003, determined by joint inversion of teleseismic body wave and near-field data, *Bull. Seism. Soc. Am*., 94 (5),1795-1807.

Yagi, Y., Nishimura, N. and Kasahara, A. (2012a). Source process of the 12 May 2008 Wenchuan, China, earthquake determined by waveform inversion of teleseismic body waves with a data covariance matrix, *Earth, Planets and Space*, 64, e13-e16.

Yagi, Y., Nakao, A. and Kasahara, A. (2012b). Smooth and rapid slip near the Japan Trench during the 2011 Tohoku-oki earthquake revealed by a hybrid back-projection method, Earth Planet. Sci. Lett., 355, 94-101.

Yagi, Y. and Kikuchi, M. (2003). Partitioning between seismogenic and aseismic slip as highlighted from slow slip events in Hyuga-nada, Japan, *Geophys. Res. Lett*., 30, 1087.

Ye, L., Lay, T., Kanamori, H., Zhan, Z. and Duputel, Z. (2016). Diverse rupture processes in the 2015 Peru deep earthquake doublet, *Science Advances*, Vol. 2, no. 6, doi: 10.1126/sciadv.1600581.

Ye, L., Lay, T., Bai, Y., Cheung, K. F. and Kanamori, H. (2017). The 2017Mw8.2Chiapas, Mexico, earthquake: Energetic slab detachment. *Geophysical Research Letters*,44, 11,824–11,832.

Yolsal, S., (2008). Source mechanism parameters and slip distributions of Crete-Cyprus Arcs, Dead Sea transform fault earthquakes and historical tsunami simulations, (Ph. D. Thesis) Istanbul Technical University, Instutute of Science Engineering and Technology, ISTANBUL.

Yolsal-Çevikbilen, S., Ulutaş, E. and Taymaz, T. (2018). Source Models of the 2012 Haida Gwaii (Canada) and 2015 Illapel (Chile) Earthquakes and Numerical Simulations of Related Tsunamis *Pure Applied Geophysics*, https://doi.org/10.1007/s00024-018-1996-5.

Yolsal-Çevikbilen, S. and Taymaz, T. (2012). Earthquake source parameters along the Hellenic subduction zone and numerical simulations of historical tsunamis in the Eastern Mediterranean. *Tectonophysics*, v. 536, p. 61-100.

Yolsal-Çevikbilen, S., Taymaz, T. and Helvacı, C. (2014). Earthquake mechanisms in the Gulfs of Gökova, Sığacık, Kuşadası, and the Simav Region (western Turkey): Neotectonics, seismotectonics and geodynamic implications, *Tectonophysics*, Vol: 635, pp. 100-124, doi:10.1016/j.tecto.2014.05.001.

Yolsal, S., Taymaz, T. and Yalçıner, A.C. (2007). Understanding Tsunamis, Potential Source Regions and Tsunami Prone Mechanisms in the Eastern Mediterranean, *In:* The Geodynamics of the Aegean and Anatolia (eds. Tuncay Taymaz, Yücel Yılmaz & Yıldırım Dilek), pp. 201-230, *The Geological Society of London*, *Special Publications Book*, Vol: 291, ISBN: 978-1-86239-239-7, DECEMBER 2007.

Zwick, P., McCaffrey, R. and Abers, G. (1994). MT5 Program, IASPEI Software Library.

APPENDICES

APPENDIX A : Table of coordinates of seismic stations used for estimating focal mechanism solutions.

APPENDIX A

Table A.1: Station locations used in inversions revealing source mechanism solutions of the September 25, 2013 Acari (Peru) and September 9, 2017 Chiapas (Mexico) earthquakes (Taken from IRIS-DMC, http://ds.iris.edu/wilber3/find_event).

STATION	LATITUDE	LONGITUDE	STATION	LATITUDE	LONGITUDE
AAM	42.30120	-83.65670	EYMN	47.94620	-91.49500
ACSO	40.23189	-82.98203	FDF	14.73333	-61.15033
AFI	-13.90940	-171.77700	FFC	54.72500	-101.97800
AGMN	48.29775	-95.86189	FUR	48.16550	11.27633
AHID	42.76539	-111.10039	GAC	45.70330	-75.47830
ALE	82.50330	-62.35000	GLA	33.05149	-114.82706
ANGG	65.61600	-37.63700	GO09	-51.27067	-72.33811
ANMO	34.94591	-106.45720	GOGA	33.41120	-83.46660
ARV	43.49767	12.94103	GRFO	49.69090	11.22030
ASCN	-7.93269	-14.36011	GRGR	12.13239	-61.65403
BBB	52.18470	-128.11300	HKT	29.95000	-95.83333
BBSR	32.37119	-64.69619	HOPE	-54.28361	-36.48789
BELA	-77.87500	-34.62690	HRV	42.50640	-71.55830
BFO	48.33010	8.32956	ICQ	49.52170	-67.27190
BINY	42.19930	-75.98610	IGLA	53.41950	-9.37500
BORG	64.74740	-21.32680	ISOG	65.54800	-38.97570
BOZ	45.59700	-111.62970	IVI	61.20581	-48.17119
BW06	42.76669	-109.55825	JOHN	16.73289	-169.52919
CART	37.58681	-1.00119	JUBA	-62.23733	-58.66267
CBKS	38.81400	-99.73740	KBS	78.92561	11.94169
CCA1	50.18660	-5.22770	KDAK	57.78281	-152.58350
CFF	45.76300	3.11119	KEV	69.75530	27.00670
CIA	31.56500	-8.75900	KIP	21.42330	-158.01400
CLF	46.82500	-119.38700	KONO	59.64910	9.59822
CMB	38.03456	-120.38650	LBNH	44.24010	-71.92590
CMLA	37.76369	-25.52431	LCO	-29.01111	-70.70100
CNNC	35.23931	-77.89011	LVC	-22.61000	-68.91000
COLA	64.87381	-147.85111	MA2	59.57530	150.76800
COR	44.58570	-123.30300	MACI	28.25019	-16.50819
DAG	76.77140	-18.65470	MAHO	39.89589	4.26650

STATION	LATITUDE	LONGITUDE	STATION	LATITUDE	LONGITUDE
DBG	74.30710	-20.21930	MBO	14.39080	-16.95470
DBIC	6.67008	-4.85631	MID	59.42780	-146.33900
DGR	33.64997	-117.00947	MLAC	37.63019	-118.83605
DRLN	49.25600	-57.50420	MLS	42.95783	1.09467
DSB	53.24519	-6.37619	MNTQ	45.50030	-73.62280
DWPF	28.11030	-81.43270	MPG	38.16170	13.36000
ECH	48.21583	7.15833	MTE	40.39969	-7.54419
EFI	-51.67531	-58.06369	NEW	48.26419	-117.12269
ELK	40.74480	-115.23900	NHSC	33.10669	-80.17781
ESK	55.31670	-3.20500	NOR	81.60000	-16.68330
ESPZ	-63.39806	-56.99639	NRS	61.15953	-45.41875
EUNU	80.05331	-86.41581	NUUK	64.18000	-51.73000
ORCD	-60.73806	-44.73611	ULM	50.24970	-95.87500
PAB	39.54580	-4.34833	USC	34.01917	-118.28597
PEL	-33.14360	-70.68530	VBMS	32.21850	-90.51767
PESTR	38.86720	-7.59020	VLDQ	48.11239	-77.45361
PET	53.02389	158.65306	WCI	38.22900	-86.29381
PFO	33.61170	-116.45940	WLF1	53.28940	-4.39660
PFVI	37.13281	-8.82681	WMOK	34.73790	-98.78100
PKME	45.26439	-69.29169	WVT	36.12969	-87.83000
PMS	61.24470	-149.56100	XMAS	2.04481	-157.44531
PMSA	-64.77420	-64.04900	SCZ2	33.99540	-119.63510
POHA	19.75750	-155.53250	SFJD	66.99600	-50.62150
PPT	-17.56825	-149.57614	SHEL	-15.95880	-5.74569
PTCN	-25.07136	-130.09533	SJG	18.11167	-66.15000
PVAQ	37.40370	-7.71730	SMAI	-68.13020	-67.10590
RAR	-21.21250	-159.77300	SMRT	18.05050	-63.07460
RCBR	-5.82750	-35.90139	SNCC	33.24787	-119.52437
RPN	-27.12670	-109.33400	SOEG	68.20330	-31.37700
SACV	14.97019	-23.60850	SPIA	57.17660	-170.24770
SAML	-8.94881	-63.18319	SSB	45.27919	4.54167
SAO	36.76403	-121.44722	SSPA	40.63580	-77.88760
SBA	-77.85030	166.75600	SUR	-32.38000	20.81167
SBC	34.44170	-119.71330	TAM	22.79170	5.52333
SCHQ	54.83190	-66.83360	TAOE	-8.85490	-140.14820
SCO	70.48330	-21.95000	TEIG	20.22631	-88.27639
TIXI	71.64900	128.86650			
TSUM	-19.20220	17.58380			
TUC	32.30980	-110.78470			

CURRICULUM VITAE

Name Surname : Hakan Tarık Meriç

Place and Date of Birth :İstanbul - 19.10.1993

E-Mail : htarikmeric@gmail.com

EDUCATION

- **B.Sc.** : 2016, Kocaeli University, Faculty of Engineering, Geophysical Engineering Department
- **M.Sc.** : 2019, Istanbul Technical University, Graduate School of Science, Engineering and Technology , Geophysical Engineering Department

PUBLICATIONS, PRESENTATIONS AND PATENTS ON THE THESIS:

- **Meriç, H. T., Yolsal-Çevikbilen, S., and Taymaz, T**, (2018). Fault Model of 25 September 2013 PERU (MW 7.1) Earthquake and Tsunami Initiation, April 23-27, 2018 Ankara, Turkey. (71st Geological Congress of Turkey, Abstracts Book, Geoscientist of the Future, 337-338).
- **Meriç, H. T., Yolsal-Çevikbilen, S., and Taymaz, T**, (2018). Fault Mechanism and Tsunami Simulation of September 08, 2017 Mexico (Mw 8.2) Earthquake, April 8-13, 2018 Vienna, Austria. (Vol. 20, EGU2018-720-2, 2018 EGU General Assembly 2018).
- **Meriç, H. T., Yolsal-Çevikbilen, S., and Taymaz, T,** (2017). Source Mechanisms and Numerical Tsunami Simulations of September 25, 2013 Peru Earthquake (Mw: 7.1), May 10-12, 2017, İstanbul, Turkey. (90 Yılın Ardından İstanbul Üniversitesi'nde Jeofiziğin Serüveni, 39).